Economic Geology, v. 114, no. 5, pp. 857–896

Mineralization and Alteration of a Modern Seafloor Massive Sulfide Deposit Hosted in Mafic Volcaniclastic Rocks

Melissa O. Anderson,[1,2,†,*] Mark D. Hannington,[1,2] Timothy F. McConachy,[3] John W. Jamieson,[4] Maria Anders,[2] Henning Wienkenjohann,[5] Harald Strauss,[5] Thor Hansteen,[2] and Sven Petersen[2]

[1]*Department of Earth and Environmental Sciences, University of Ottawa, 25 Templeton Street, Ottawa, Ontario K1N 6N5, Canada*

[2]*GEOMAR, Helmholtz Centre for Ocean Research Kiel, Wischhofstrasse 1–3, Kiel 24148, Germany*

[3]*Neptune Minerals, Inc., 3/30 Woolcott Street, Waverton, New South Wales 2060, Australia*

[4]*Department of Earth Sciences, Memorial University of Newfoundland, 40 Arctic Avenue, St. John's, Newfoundland A1B 3X7, Canada*

[5]*Institute für Geologie und Paläontologie, Westfälische Wilhelms-Universität, Corrensstrasse 24, Münster 48149, Germany*

Abstract

Tinakula is the first seafloor massive sulfide deposit described in the Jean Charcot troughs and is the first such deposit described in the Solomon Islands—on land or the seabed. The deposit is hosted by mafic (basaltic-andesitic) volcaniclastic rocks within a series of cinder cones along a single eruptive fissure. Extensive mapping and sampling by remotely operated vehicle, together with shallow drilling, provide insights into deposit geology and especially hydrothermal processes operating in the shallow subsurface. On the seafloor, mostly inactive chimneys and mounds cover an area of ~77,000 m^2 and are partially buried by volcaniclastic sand. Mineralization is characterized by abundant barite- and sulfide-rich chimneys that formed by low-temperature (<250°C) venting over ~5,600 years. Barite-rich samples have high SiO_2, Pb, and Hg contents; the sulfide chimneys are dominated by low-Fe sphalerite and are high in Cd, Ge, Sb, and Ag. Few high-temperature chimneys, including zoned chalcopyrite-sphalerite samples and rare massive chalcopyrite, are rich in As, Mo, In, and Au (up to 9.26 ppm), locally as visible gold. Below the seafloor, the mineralization includes buried intervals of sulfide-rich talus with disseminated sulfides in volcaniclastic rocks consisting mainly of lapillistone with minor tuffaceous beds and autobreccias. The volcaniclastic rocks are intensely altered and variably cemented by anhydrite with crosscutting sulfate (± minor sulfide) veins. Fluid inclusions in anhydrite and sphalerite from the footwall (to 19.3 m below seafloor; m b.s.f.) have trapping temperatures of up to 298°C with salinities close to, but slightly higher than, that of seawater (2.8–4.5 wt % NaCl equiv). These temperatures are 10° to 20°C lower than the minimum temperature of boiling at this depth (1,070–1,204 m below sea level; m b.s.l.), suggesting that the highest-temperature fluids boiled below the seafloor. The alteration is distributed in broadly conformable zones, expressed in order of increasing depth and temperature as (1) montmorillonite/nontronite, (2) nontronite + corrensite, (3) illite/smectite + pyrite, (4) illite/smectite + chamosite, and (5) chamosite + corrensite. Zones of argillic alteration are distinguished from chloritic alteration by large positive mass changes in K_2O (enriched in illite/smectite), MgO (enriched in chamosite and corrensite), and Fe_2O_3 (enriched in pyrite associated with illite/smectite alteration). The $\delta^{18}O$ and δD values of clay minerals confirm increasing temperature with depth, from 124° to 256°C, and interaction with seawater-dominated hydrothermal fluids at high water/rock ratios. Leaching of the volcanic host rocks and thermochemical reduction of seawater sulfate are the primary sources of sulfur, with $\delta^{34}S$ values of sulfides, from –0.8 to 3.4‰, and those of sulfate minerals close to seawater sulfate, from 19.3 to 22.5‰.

The mineralization and alteration at Tinakula are typical of a class of ancient massive sulfide deposits hosted mainly by permeable volcaniclastic rocks with broad, semiconformable alteration zones. Processes by which these deposits form have never been documented in modern seafloor massive sulfide systems, because they mostly develop below the seafloor. Our study shows how hydrothermal fluids can become focused within permeable rocks by progressive, low-temperature fluid circulation, leading to a large area (>150,000 m^2) of alteration with reduced permeability close to the seafloor. In our model, overpressuring and fracturing of the sulfate- and clay-cemented volcaniclastic rocks produced the pathways for higher-temperature fluids to reach the seafloor, present now as sulfate-sulfide veins within the footwall. In the geologic record, the sulfate (anhydrite) is not preserved, leaving a broad zone of intense alteration with disseminated and stringer sulfides typical of this class of deposits.

Introduction

Volcanogenic massive sulfide (VMS) deposits have been classified according to host-rock lithology, bulk composition, and tectonic setting (e.g., Barrie and Hannington, 1999; Franklin et al., 2005). In extensional volcanic arc and back-arc environments, VMS deposits are typically hosted by volcanic successions including both clastic and coherent rock types (cf. Franklin et al., 2005; Hannington et al., 2005; Galley et al., 2007). Volcanic facies play a first-order control on the sizes and shapes of the deposits, the flow of hydrothermal fluids, and the nature of the footwall alteration zones. Coherent lavas that formed by effusive eruptions are relatively impermeable,

†Corresponding author: e-mail, melissao.anderson@utoronto.ca
*Current address: Department of Earth Sciences, University of Toronto, 22 Russell Street, Toronto, Ontario M5S 3B1, Canada.

ISSN 0361-0128; doi:10.5382/econgeo.4666; 40 p.
Digital appendices are available in the online Supplements section.

Submitted: October 25, 2018 / Accepted: May 17, 2019

and hydrothermal fluids tend to be focused along faults with minimal influx of cold seawater and form discordant pipe-like alteration zones (e.g., Ansel and Amulet deposits, Noranda district, Québec: Kerr and Gibson, 1993; Gibson and Galley, 2007). In contrast, volcaniclastic-dominated strata have high permeability and porosity, promoting lateral fluid flow, widespread mixing with seawater, and broadly stratiform alteration zones. There are numerous examples of ancient volcaniclastic-hosted VMS deposits, including the Mattabi deposit in the Sturgeon Lake Caldera Complex, Canada (cf. Franklin et al., 1975; Morton and Franklin, 1987; Holk et al., 2008), the Horne and Bouchard-Hebert deposits in the Noranda mining district, Canada (cf. Gibson et al., 1993; Galley et al., 1995), the Boundary deposit in the Newfoundland Appalachians, Canada (cf. Piercey et al., 2014), and the Rosebery deposit in the Mount Read Volcanics belt of western Tasmania (cf. Large et al., 2001). In these deposits, the massive sulfide orebodies occur as stratiform lenses that are interpreted to form in whole or in part below the seafloor. Underlying the massive sulfide lenses, stringer mineralization is vertically restricted, occurring as semiconformable zones of disseminated sulfide mineralization. In the immediate footwall of the VMS deposits, zones of diffuse pipe-like alteration occur along synvolcanic faults, consisting of extreme leaching, silica mobility, and Fe metasomatism (e.g., Morton and Franklin, 1987). Typical alteration assemblages are sericite and chlorite, occurring as matrix cement and pervasive replacement of glass-rich clasts (e.g., Gifkins and Allen, 2001). These diffuse pipe-like zones merge outward into more widespread semiconformable alteration zones (e.g., Franklin et al., 1975). The geometry of these zones can be distinguished using oxygen isotope mapping, where increasing $\delta^{18}O$ values of altered rocks are associated with decreasing temperatures of hydrothermal activity (e.g., King et al., 2000; Holk et al., 2008). Importantly, silicified horizons tend to form near the seafloor, acting as impermeable caps that isolate high-temperature circulation from shallow, low-temperature hydrothermal regimes (e.g., Franklin et al., 1981; Galley, 1993). This highlights the importance of early hydrothermal processes, such as silicification, in controlling the pathways of subsequent fluid flow (cf. Gibson et al., 1983; Skirrow and Franklin, 1994). While hydrothermal fluid flow regimes and associated alteration processes are well studied in the ancient rock record, these processes are largely unknown in modern settings due a lack of seafloor drilling to investigate the third dimension of these systems.

The Tinakula seafloor massive sulfide (SMS) deposit is the first identified modern analog of a mafic volcaniclastic-dominated deposit of the type described by Morton and Franklin (1987). It is located in the Jean Charcot troughs in the northern New Hebrides back arc, centered at 167°36'50"E/12°12'10"S (Fig. 1). This part of the Jean Charcot troughs is characterized by enhanced magmatism where regional structures, including the EW-trending Tikopia fracture zone, extend into the back arc (Fig. 1A). The transition from the arc to the back arc is marked by an abrupt change from tectonic extension associated with normal faulting to magmatic-tectonic extension where dike-fed lavas have erupted along linear fissures (Fig. 1B). Unlike hydrothermal systems in many deep back-arc basins, which are localized along mid-ocean ridge-type spreading centers (e.g., Hannington et al., 2005), hydrothermal activity at Tinakula is focused along a row of young mafic cinder cones on the flank of the Starfish stratovolcano (Figs. 1B, 2). Cinder cones are common volcanic landforms but have not been widely described on the modern seafloor. These features form from the buildup of volcanic tephra associated with Strombolian-style eruptions (i.e., fire-fountaining; cf. Cashman, 2004). Submarine pyroclastic deposits associated with fire-fountaining eruptions have been described in the ancient rock record (e.g., Mueller and White, 1992). This style of eruption may be more common in arc-proximal settings where mafic magmas have higher water contents compared to those in other tectonic settings (e.g., Gill et al., 1990).

In this paper, we present a comprehensive three-dimensional study of an actively forming massive sulfide deposit, with seafloor and subseafloor components, in a nascent back-arc setting dominated by bimodal mafic volcaniclastic rocks. We investigate how features of the volcaniclastic substrate have influenced the mineralization and alteration at Tinakula, including the possible roles of boiling, fluid mixing, duration of hydrothermal activity, host-rock compositions, and magmatic contributions to the hydrothermal system.

Regional Geology and Exploration History

The Jean Charcot troughs in the northern New Hebrides (Vanuatu-Solomon Islands) constitute one of the youngest back arcs in the world, forming only ~4 m.y. ago in response to eastward subduction and rollback of the Indo-Australian plate beneath the Pacific plate (Fig. 1; Monjaret et al., 1991; Pelletier et al., 1998). Unlike the simple graben morphologies of other young back-arc rifts, such as the Coriolis troughs to the south (cf. Anderson et al., 2016), back-arc extension in the Jean Charcot troughs is characterized by a complex series of horst-and-graben structures that are widely spaced up to ~120 km from the arc front and have variable orientations (Fig. 1A; Pelletier et al., 1993; Maillet et al., 1995). Seafloor depths range from ~800 to 3,600 m below sea level (m b.s.l.), and individual grabens range from 20 to 65 km long and 5 to 15 km wide. The Jean Charcot troughs are bound to the south by the Hazel Holme fracture zone, a seismically active ridge that is considered to be an extensional zone related to opening of the North Fiji basin (Maillet et al., 1995). A second EW-trending extensional zone (Tikopia fracture zone; Fig. 1A) occurs north of the Hazel Holme fracture zone. Like the Hazel Holme fracture zone, the Tikopia fracture zone displays a slow-spreading trough morphology to depths of ~4,200 m b.s.l. east of Tikopia Island. To the west of this island, the presence of volcanic ridges and aligned seamounts suggests that the basement structure that controls the location of volcanic activity extends at least as far as the volcanic arc. Where the Tikopia fracture zone crosses the back-arc region, there is a notable bathymetric high, interpreted to be recent volcanic complexes that obscure the horst-and-graben morphology of the back arc (Fig. 1A; Récy et al., 1986). The Jean Charcot troughs are separated from the North Fiji basin by the West Tikopia Ridge and the Duff Ridge, which are interpreted to be part of the prerift fossil volcanic arc (Auzende et al., 1995). There is no consensus on the northern extent of the Jean Charcot troughs, although here we consider these to include the NW-SE–trending trough between the Duff Ridge and the Reef Islands. The current rate of extension of the

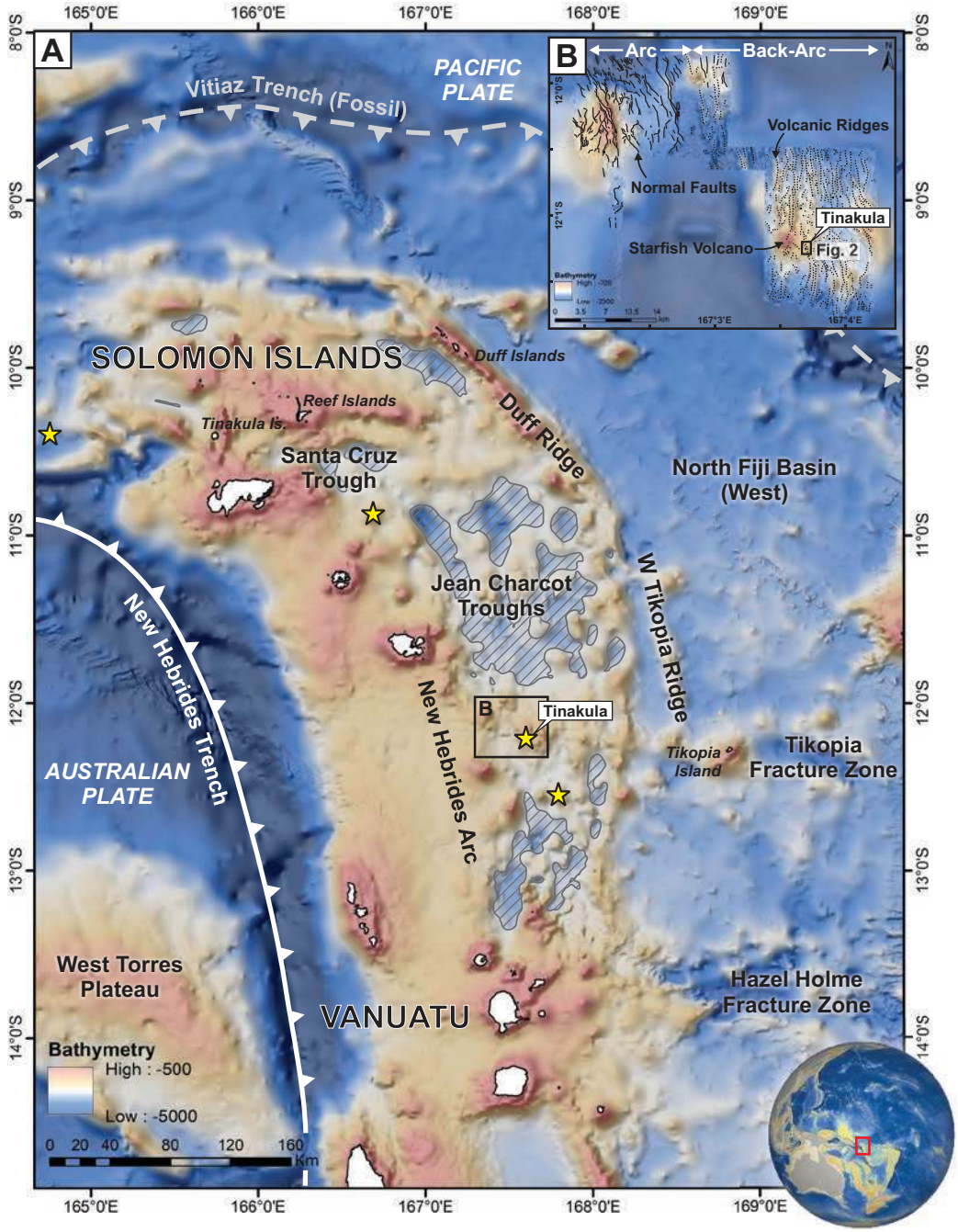

Fig. 1. Seafloor morphology of the Jean Charcot troughs. (A) Global marine altimetry from Sandwell et al. (2014), with back-arc troughs deeper than 2,800 m b.s.l. indicated by gray hatched pattern. (B) RESON SeaBat 8160 50-kHz multibeam bathymetry of the Starfish area (50 m resolution) collected by Neptune Minerals, Inc., showing transition from tectonic extension in the arc (forming NNW-trending normal faults, black lines) to tectonic-magmatic extension in the back arc (forming N-trending volcanic ridges, dotted black lines). Location of Tinakula deposit (Fig. 2) is shown, along with other sites of hydrothermal venting indicated by yellow stars (after Beaulieu and Szafranski, 2018). Globe inset in lower right corner shows location of research area in the South Pacific Ocean.

troughs increases northward from 36 to 55 mm yr^{-1} to 70 to 81 mm yr^{-1} (Bergeot et al., 2009); however, this extension may be distributed over the entire width of the back arc, in which case individual troughs could be opening much more slowly.

Research cruises in the late 1980s to early 1990s provided most of the geochemical data that we now have for the Jean Charcot troughs (summarized by Maillet et al., 1995), but high-resolution (50 m or better) regional bathymetric data are lacking, and most of the region is unexplored, particularly in the north. The first indication of hydrothermal venting in the Jean Charcot troughs was a methane anomaly detected in the water column near the Starfish seamount during the KAIYO 89 cruise (Urabe et al., 1990). This anomaly was investigated on the SOLAVENTS cruise, which recovered fresh and

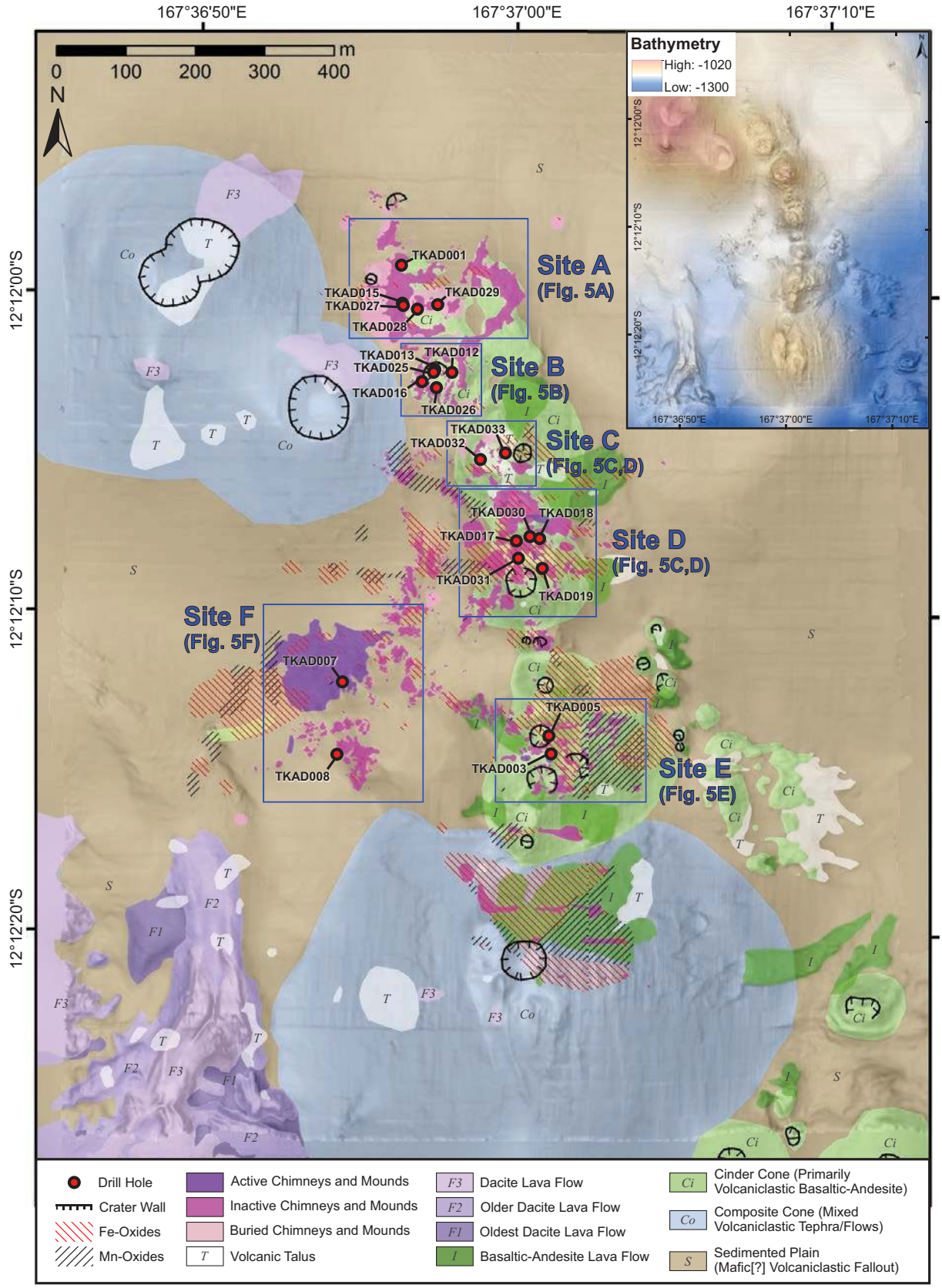

Fig. 2. Geology of the Tinakula deposit area interpreted from ROV dive videos and sampling overlain on hill- and slope-shaded RESON SeaBat 7125-ROV2 400-kHz multibeam bathymetry (inset), with locations of study sites and drill holes indicated.

altered rhyodacite samples by dredging and recorded a number of temperature anomalies in the water column near the seafloor (McConachy et al., 2002). Additional cruises in the area included the SEAPSO Leg 2 cruise (Récy et al., 1986), a GLORIA side-scan sonar survey (Johnson et al., 1992), and the SOPACMAPS cruise (Kroenke, 1995). More recent work has been aimed at exploration for SMS deposits. The Tinakula deposit was discovered by Neptune Minerals, Inc., in September 2011 during the ASHR Leg 2 cruise aboard the MV Dorado Discovery. It is located in the Temotu Province within the exclusive economic zone of the Solomon Islands, approximately 890 km east-southeast of Guadalcanal. The discovery was initially made by locating the source of a seafloor-hugging hydrothermal plume, followed by dives with a remotely operated vehicle (ROV), which located sulfide chimneys. Additional mapping, ROV grab sampling, and shallow drilling occurred during four subsequent (2011–2012) cruises.

Host Rocks, Volcanology, and Structure

The Tinakula SMS deposit is located at depths of 1,070 to 1,204 m b.s.l. on the flank of the Starfish stratovolcano (Fig. 1B). The geology of the Tinakula area has been interpreted from seafloor observations and sampling during ROV dives, drill core logging, and analysis of newly acquired high-resolution (20 cm) bathymetry. The bathymetry details reveal a strong structural control on volcanic and hydrothermal features (Fig. 2).

Volcanoes in the Tinakula area are composed of basaltic andesite (53.4–57.3 wt % SiO_2) and dacite (63.0–67.9 wt % SiO_2) (Anderson, 2018) and include composite cones, cinder cones, and the submarine equivalent of maars (craters without cones) (see App. Fig. A1). The morphologies of these edifices are broadly similar to those of subaerial volcanoes, but the edifices are consistently smaller than their subaerial equivalents. In the central part of the map area, the volcanic cones are aligned along a large (~1.6 km long) NS-trending fissure (Fig. 2, inset). The southern part of the fissure is dominated by a large composite cone with bimodal lava flows and blocky volcanic talus. This is followed northward by a 900-m-long row of cinder cones, on which the deposit is centered, and two small maar-like craters at the northern end of the fissure. The volcanic material making up the cinder cones consists of variably altered basaltic andesite with vertical and lateral facies variations over several meters, including changes in clast size, shape, composition, and degree of sorting (Figs. 3, 4; App. Figs. A2-A18). The breccia facies include the following: (1)

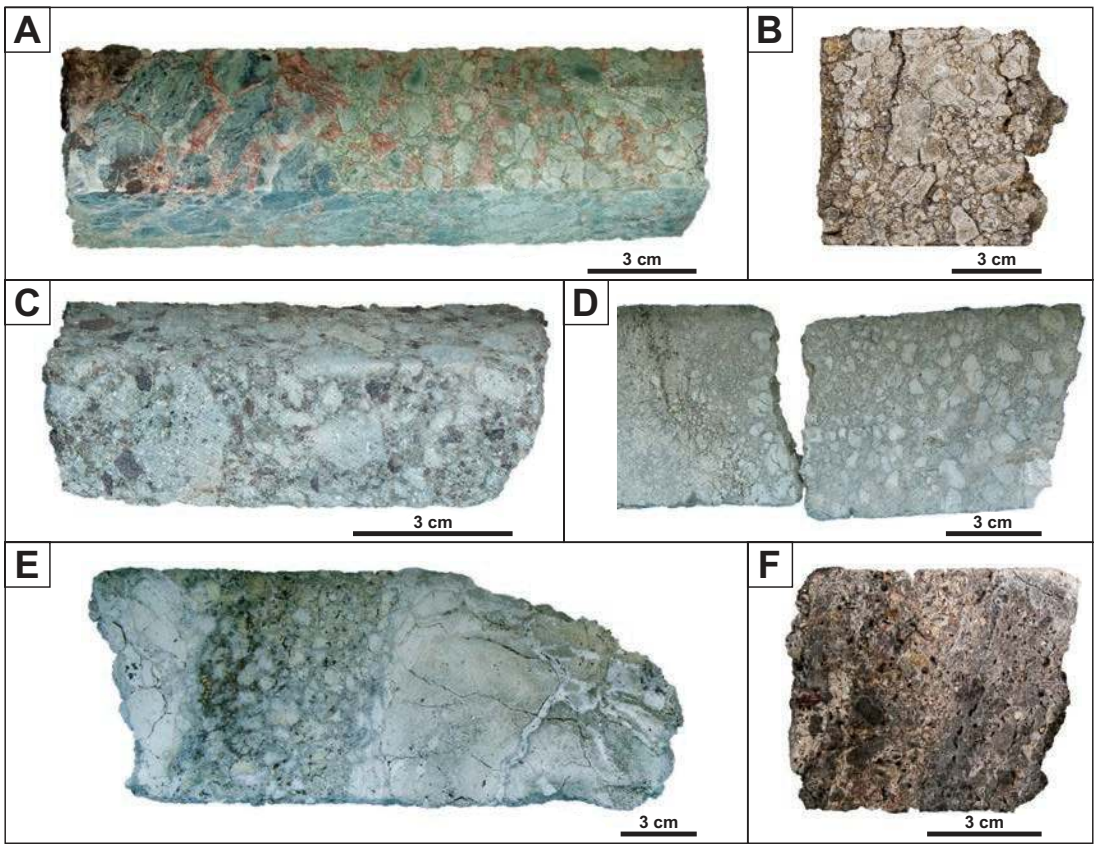

Fig. 3. Volcanic and hydrothermal features of the footwall of the Tinakula deposit. (A) Variably clay altered, monomict, matrix-supported hyaloclastite breccia with flow foliation and local jigsaw-fit, sulfate-cemented with minor iron oxides (dark red) and chlorite alteration (green) (sample P003). (B) Intensely clay altered, monomict, clast-supported volcanic breccia (hyaloclastite), weakly sulfate-cemented (sample MA13-074). (C) Variably clay altered, polymict, clast-supported lapillistone, sulfate-cemented (sample P002). (D) Intensely clay altered, monomict, clast-supported lapillistone, sulfate-cemented and weakly graded (sample MA13-092). (E) Intensely clay altered, monomict, matrix-supported lapillistone with fine-grained beds and larger blocks, sulfate-cemented with late sulfate + sulfide veins (sample MA13-087). (F) Variably altered, polymict, matrix-supported proximal reworked volcanic breccia, silicified, with preserved primary porosity (sample MA13-023).

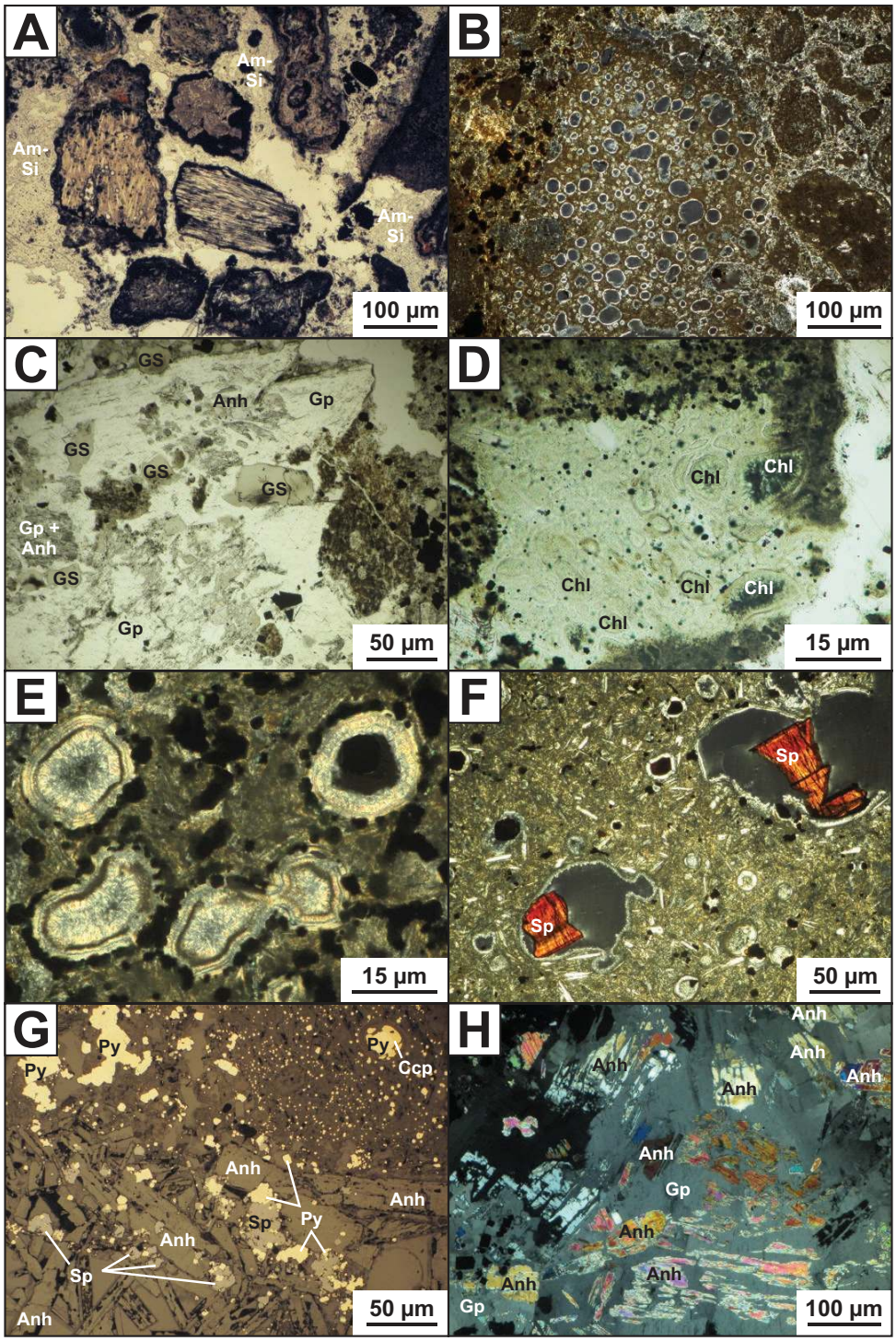

Fig. 4. Microscopic volcanic and hydrothermal features of the footwall of the Tinakula deposit, shown by transmitted-light photomicrograph in plane-polarized light (TL-PPL) or cross-polarized light (TL-XPL) or reflected-light photomicrograph in plane-polarized light (RL-PPL). (A) TL-PPL photomicrograph of polymict clast types, including glass-rich volcanic clasts and tube pumice, cemented by amorphous silica (sample MA13-023). (B) TL-XPL photomicrograph of clay-altered scoriaceous clasts with intense clay alteration of clasts and matrix (sample MA13-068). (C) TL-PPL photomicrograph of volcanic clasts and glass shards surrounded by gypsum after anhydrite (sample MA13-040). (D) TL-PPL photomicrograph of tube pumice with late chlorite infill (sample MA13-053). (E) TL-PPL photomicrograph of intensely clay altered clast with multiple generations of clay infilling vesicles (sample MA13-044). (F) TL-XPL photomicrograph of clay-altered clast, with clay lining of vesicles and late sphalerite (red) (sample MA13-072). (G) RL-PPL photomicrograph of fine-grained pyrite disseminated throughout altered clast and late sulfides (pyrite, sphalerite, chalcopyrite) surrounded by anhydrite (blades) (sample MA13-045). (H) TL-XPL photomicrograph of anhydrite altered to gypsum (sample MA13-040). Abbreviations: Am-Si = amorphous silica, Anh = anhydrite, Ccp = chalcopyrite, Chl = chlorite, Gp = gypsum, GS = glass shard, Py = pyrite, Sp = sphalerite.

monomict breccia characterized by clasts with glassy curviplanar margins, flow-banded phenocrysts, and local jigsaw-fit textures (Figs. 3A, B, 4B); (2) monomict breccia composed of vesicular volcanic clasts associated with variable amounts of juvenile clasts, glass shards, and crystal fragments and rare blocks or bombs (Figs. 3C-E, 4C); and (3) polymict breccia associated with mass-flow bedforms with rounded to subangular clasts, ranging from relatively unaltered to completely clay altered clasts (Fig. 3F). The predominant facies is massive to crudely bedded monomict breccia (lapillistone) with clasts containing up to 20% vesicles (uniformly distributed) and no evidence of welding. Basaltic-andesitic lava flows were the last products to be erupted along the row of cinder cones at Tinakula. These facies are consistent with cinder cones on land, which form via Strombolian-type eruptions, progressing from cone-building activity to lava flows during the waning stages as the magma loses most of its gas (Vergnoille and Mangan, 2000). Cinder cones of the type at Tinakula are generally considered to be monogenic, having formed during one eruptive cycle over a period of days to months (e.g., Wood, 1980).

Dark-colored mafic(?) volcaniclastic sediment covers most of the map area around the Tinakula deposit, interpreted to be fallout from nearby eruptions. The material ranges from coarse sand- to pebble-sized, with a few larger volcanic fragments or bombs (with elongate vesicles and quenched margins) and no fine ash-sized fraction. The sediment ranges in thickness from 1.5 to >8 m and is massive to crudely bedded with weak grading. Abundant ripple marks are observed in the sediment, with large-scale dunes (up to 7 m wide and 124 m long) visible in the bathymetric data.

Two large (55–87 m tall and 327–512 m wide) composite cones with dacite lava flows in the northwest corner of the mapped area (Fig. 2) appear to be unrelated to the central fissure. Large dacitic lava flows in the southwest corner of the map have a distinctly different morphology, with sinuous ridges that are characteristic of channelized flow. The relative ages of the flows are interpreted from ROV dive observations of sediment thickness, with higher degrees of sediment associated with older relative ages. The ages of these flows relative to other eruptions in the area are unknown.

Deposit Geology

The Tinakula SMS deposit consists of a series of over 900 chimneys and mound complexes distributed over a strike length of ~1,050 m along the row of cinder cones and composite cones (Fig. 2). The chimneys and mounds are located mainly at the tops and along the flanks of the cinder cones, as well as inside the summit craters (Fig. 5). They also occur in the center of each of the maar-like craters in the north. West of the row of cinder cones, over a strike length of ~400 m, the chimneys and mounds are not spatially associated with observable volcanic features at the seafloor but instead appear to occur along two partially buried northeast-southwest and northwest-southeast structures (between sites F and D and between sites F and E; Fig. 2).

The chimneys at Tinakula are <1 to 15 m high (typically 2–8 m) and include typical multispired sulfide structures with central vent orifices (Fig. 6A, B) and, more commonly, chimneys with irregular morphologies (bulbous, drooping, with smooth or popcorn-textured outer surfaces; Fig. 6C, D). The bulbous chimneys lack central orifices and have a morphology similar to those of beehives or flange-type chimneys (e.g., Koski et al., 1994; Zhu et al., 2007). The chimneys are commonly surrounded by sulfide talus and grow on top of low-relief hydrothermal mounds that typically rise ~2 to 3 m from the seafloor. The extent of these mounds is largely unknown due to burial by volcaniclastic sediments, but they appear to make up the bulk of the mineralization at the seafloor, accounting for about two-thirds of the total amount of identified massive sulfide. Individual chimney mound complexes can be traced for up to 70 m on the seafloor. Where exposed, the mound material is distinctly laminated with layers of barite and sulfide minerals up to 0.5 m thick, and they have unexpectedly smooth surfaces (Fig. 6C). The layered barite-sulfide mounds are most similar to features described by Hein et al. (2014) from the East Diamante caldera in the Mariana arc. The sulfide deposits are mostly inactive, and the surrounding volcaniclastic sediment is widely indurated and locally mineralized (Fig. 6D). Active venting is limited to a few sites with shimmering water at the base of chimneys or along fractures in the indurated sediments, associated with bacterial mats (Fig. 6A). Venting of white to gray smoke from chimney spires is rare (Fig. 6B). Fe-Mn oxides are widespread along fractures in the seafloor, extending up to 100 m away from the chimney complexes and mounds (Fig. 2). Abundant <1-m-tall Fe and Mn oxyhydroxide chimneys and silica-rich chimneys are associated with bacterial mats (Fig. 6E) and occur along the fractures (Fig. 6F).

The surface expression of hydrothermal precipitates covers ~77,000 m^2, including ~13,800 m^2 of active chimneys and mounds, 51,800 m^2 of inactive chimneys and mounds, and 9,300 m^2 of partially buried chimneys and mounds (Fig. 2). Areas of low-temperature venting, dominated by Fe and Mn oxides, occur over an additional 130,000 m^2 (91,000 m^2 of Fe oxides and 38,000 m^2 of Mn oxides), although these areas commonly overlap those of the chimneys and mounds. The area of subseafloor sulfide mineralization is not completely known, so the full size of the deposit could be much larger. The areal extent of this deposit is significant compared to others discovered along mid-ocean ridges and along arcs and back-arc basins; fewer than 10% have dimensions larger than 5,000 m^2 (Hannington et al., 2010). Modern sulfide deposits with comparable sizes (by area) include the Solwara 1 deposit in the Eastern Manus basin (90,000 m^2) and the Mir zone, Ashadze-1, and Ashadze-2 deposits on the Mid-Atlantic Ridge (50,000 m^2 each) (Hannington et al., 2010, 2011). It should be emphasized, however, that the large areal footprint of the Tinakula deposit may not necessarily correlate with a large tonnage of massive sulfide.

Methods

Ship-based multibeam bathymetry operating at 50 kHz (RESON SeaBat 8160) was collected over 685.6 km^2 in the Starfish-Tinakula area, and the data were gridded with a cell size of 50 m. Higher-resolution bathymetry was collected over ~2.2 km^2 that includes the Tinakula deposit, using an ROV-mounted multibeam system (RESON SeaBat 7125-ROV2 at 400 kHz with inertial navigation) and gridded with a cell size of 0.2 m. Bottom observations and grab samples were collected during 13 ROV dives. Shallow seafloor drilling,

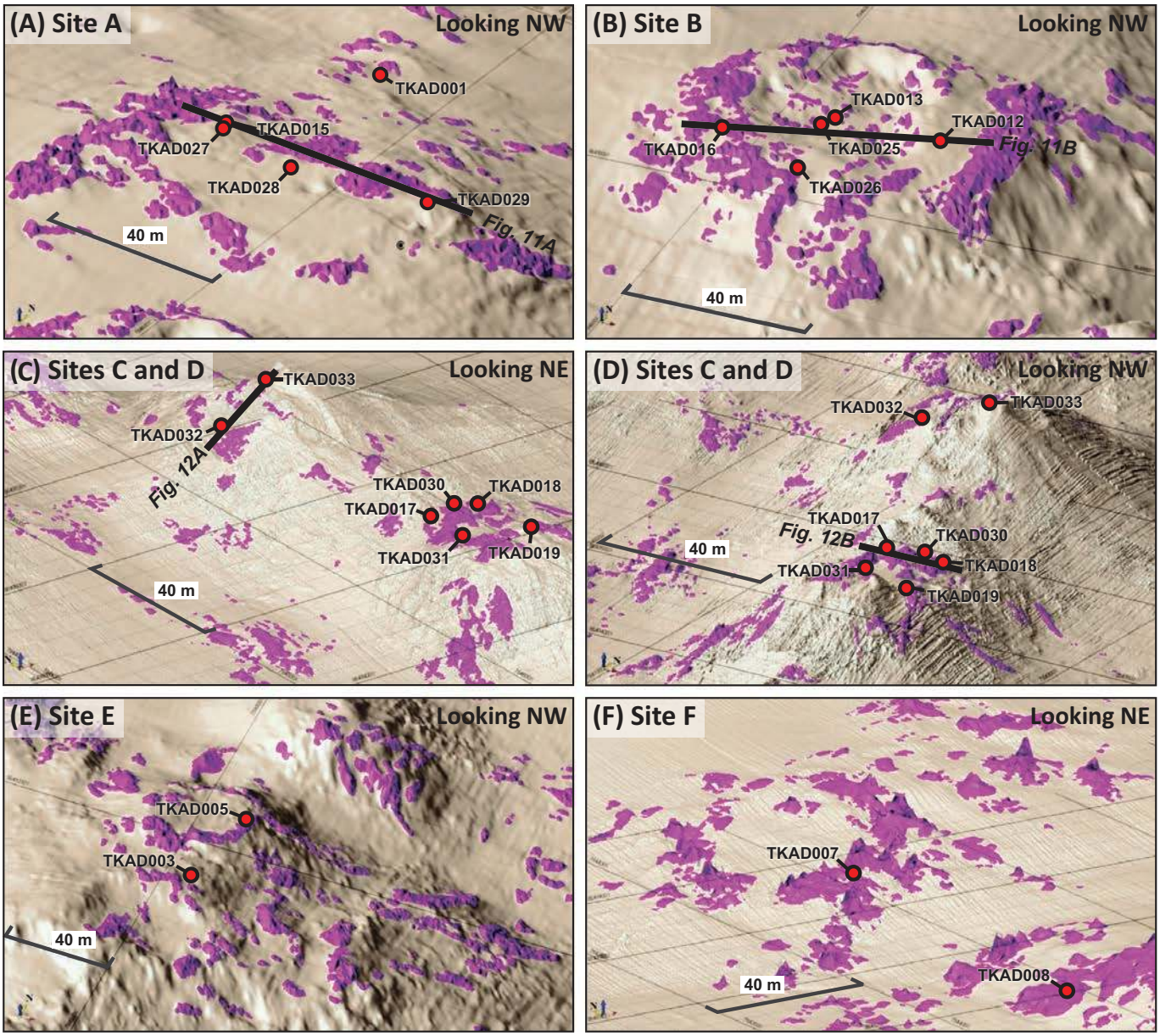

Fig. 5. 3-D close-up of the bathymetry of study sites in the Tinakula area (RESON SeaBat 7125-ROV2 400-kHz multibeam bathymetry; 0.2-m resolution), with chimney complexes and mounds (purple) and locations of drill holes (red circles) examined in this study. (A) Site A, looking northwest. (B) Site B, looking northwest. (C) Sites C and D, looking northeast. (D) Sites C and D, looking northwest. (E) Site E, looking northwest. (F) Site F, looking northeast. Locations of cross sections (Figs. 10, 11) are shown by thick black lines.

including push-coring and rotary diamond drilling, was carried out using the Benthic Geotech portable remotely operated drill PROD-3. Approximately 270 m of drill core was logged and sampled to establish between-hole correlations along the length of the NS-trending eruptive fissure (sites A-D; Fig. 2; App. Figs. A2-A18). Mineralogical and chemical data are reported here on 41 ROV grab samples and 21 drill core samples of chimney and mound material and on 61 drill core samples of clay-altered volcaniclastic rocks. Polished thin sections of the sulfide-sulfate chimney samples and epoxy-impregnated clay-altered volcaniclastic samples were prepared by Dettmar Dissection Technology (Bochum, Germany). Clay-altered samples were cut using an industry-standard water-free technique that employs kerosene in order to prevent clay swelling, slaking, and dissolution of anhydrite. Thin sections were analyzed by transmitted- and reflected-light microscopy.

Whole-rock geochemistry was determined on 45 bulk samples of sulfide-sulfate material and 47 samples of fine (<63 μm) clay-altered volcaniclastic material at Activation Laboratories (Ontario, Canada). For the sulfide samples, a sodium peroxide fusion was used; major elements (Al, Ca, K, Mg, P, Si, Ti) were analyzed by inductively coupled plasma-optical emission spectrometry (ICP-OES) and trace elements

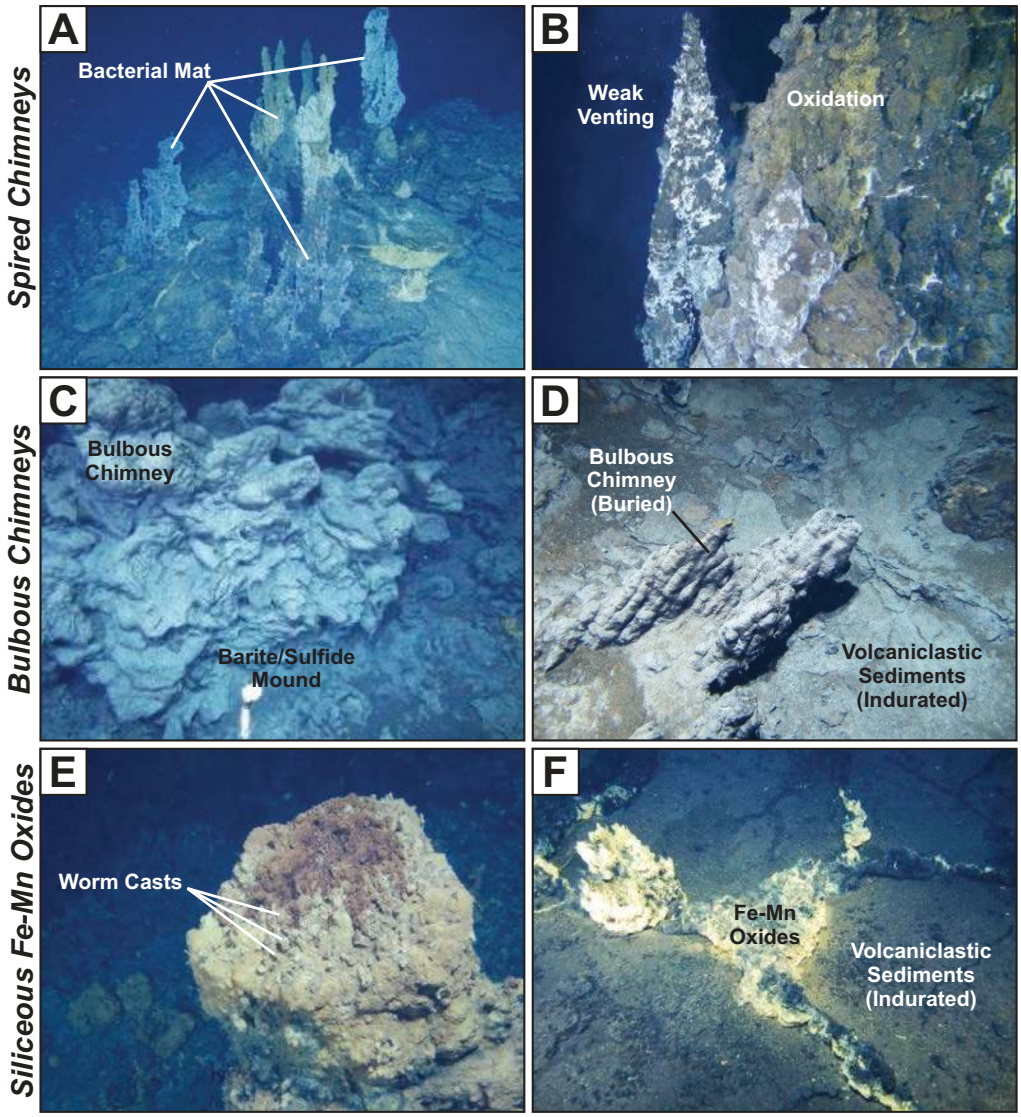

Fig. 6. Chimney morphologies encountered during ROV dive operations. (A) Partly oxidized inactive spired chimneys with bacterial mat, field of view ~15 m. (B) Weakly venting spire with minor oxidation, field of view ~3 m. (C) Inactive bulbous chimney on top of layered barite-sulfide mound, field of view ~5 m. (D) Inactive bulbous chimney partially buried by volcaniclastic sediment (indurated), field of view ~3 m. (E) Siliceous iron oxide chimney with small worm casts, field of view ~1 m. (F) Iron and manganese oxyhydroxides forming dendritic oxide chimneys in fractures within indurated volcaniclastic sediment, field of view ~5 m.

(B, Ba, Be, Bi, Cd, Co, Cs, Cu, Ga, Ge, In, Li, Mn, Mo, Nb, Ni, Pb, Rb, Sn, Sr, Ta, Th, U, V, W, Y, Zn, and rare earth elements [REEs]) by inductively coupled plasma-mass spectrometry (ICP-MS). For the clay-altered samples, a lithium metaborate/tetraborate fusion was used; the major elements (SiO_2, Al_2O_3, $Fe_2O_{3(T)}$, MnO, MgO, CaO, Na_2O, K_2O, TiO_2, P_2O_5) were analyzed by ICP-OES, and trace elements (Ba, Be, Bi, Co, Cs, Ga, Ge, Hf, In, Mo, Nb, Rb, Sr, Ta, Th, Tl, U, V, W, Y, Zr, REEs) by ICP-MS, with additional elements (Ag, Cd, Cu, Ni, Pb, Zn) analyzed by ICP-OES following a total acid digestion technique. In both sample types, cold-vapor atomic absorption spectrometry (AAS) was used to determine Hg; infrared (IR) detection was used to determine total S. Instrumental neutron activation analysis (INAA) was used to determine Au, Ag, As, Ba, Br, Cr, Fe, Hf, Ir, Lu, Na, Sb, Sc, and Zn in the sulfides and Au, As, Br, Cr, Ir, Sc, Se, and Sb in the clay-altered samples. Duplicates and standard reference materials were analyzed after every 10 to 15 samples and indicated a precision of better than 10% and accuracy of better than 5% for most elements in samples where the analytical values are well above the limit of detection, with values degrading rapidly as the limits of detection are approached.

Sulfide mineral compositions were determined in 16 sulfide-sulfate samples using a JEOL-JXA 8200 electron probe microanalyzer (EPMA) equipped with five wavelength dispersive spectrometers and one energy dispersive detector at the GEOMAR Helmholtz Centre for Ocean Research in Kiel. A 15-keV accelerating potential and 50-nA probe (cup) current were used for the analyses. Standards used were chalcopyrite (FeK_α, SK_α, CuK_α), rhodonite (MnK_α) gallium arsenide

(GaL_α, AsK_β), sphalerite (ZnK_α), silver telluride (AgL_α), indium antimonide (InL_α, SbL_α), cadmium sulfide (CdL_α), gold (AuL_α), cinnabar (HgM_α), and galena (PbM_α).

Alteration mineralogy was determined by X-ray diffraction (XRD) analysis of bulk samples of the altered footwall rocks. Fine (<63 μm) and coarse (>63 μm) fractions were separated by wet sieving, followed by separation into silt (2–63 μm) and clay (<2 μm) by settling in cylinders of standing water, following the technique of Moore and Reynolds (1997). The mineralogy of the <2-μm clay fraction from 58 samples was determined using a Philips PW 1710 X-ray diffractometer, equipped with a Co tube and an automatic divergence slit and monochromator, located at GEOMAR. Operating conditions were 40 kV and 35 mA. Oriented mounts were prepared by wet suspension followed by air drying and were measured with a 2θ scanning angle of 3° to 40° at a scan rate of 1 s per 0.01° step. Samples were then saturated with ethylene glycol following a standard vaporization technique and reanalyzed. MacDiff v.4.2.6 software was used for mineral identification and display of the XRD data.

Short-wave infrared (SWIR) reflectance spectroscopy was also used to identify alteration assemblages and compositional variations in the altered footwall rocks. Spectral measurements of fine (<63 μm) fractions were conducted using a Fieldspec® Pro spectroradiometer at the University of Ottawa, with a spectral bandwidth of 3 to 10 nm and a scan time of 100 ms. Duplicate measurements were made for every sample; white reference measurements were made every fifth sample. The data were normalized, and mineral phases were automatically identified using The Spectral Geologist (TSG) 7 software and a built-in reference library (e.g., Jinfeng et al., 2014). The spectra were then manually assessed to confirm mineral identifications based on the shape and wavelength minima of the absorption features.

Five samples consisting of hydrothermally altered and sulfate-cemented volcaniclastic material were selected from drill hole TKAD001 for fluid inclusion studies. Doubly polished thick sections (~130 μm) were prepared at Dettmar Dissection Technology using a water-free technique. Fluid inclusion petrography in barite, anhydrite, and sphalerite is described in detail in Anders (2016). Microthermometric measurements were made on a Linkam™ THMS 600 heating and freezing stage at GEOMAR. Salinities were calculated from freezing-point depression values following Bodnar and Vityk (1994). Homogenization temperatures were corrected for pressure at the sample depth (1,107.61 m b.s.l.; 108.65 bar) following Zhang and Frantz (1987). Accuracy was determined by measuring phase transitions in synthetic fluid inclusions (Syn Flinc®); replicate measurements of homogenization and freezing-point depression temperatures were performed every five to 10 analyses, resulting in estimated errors of less than ±0.2°C for salinity measurements and ±4°C for homogenization temperature measurements. The critical points, bulk molar volumes, densities, and isochores were calculated using the program FLINCOR (Brown, 1989).

Oxygen and hydrogen isotope analyses were performed on 14 samples of monomineralic clays (<2 μm), free from Fe and Mn oxides as determined by XRD. The analyses were carried out by the Queen's Facility for Isotope Research (Queen's University, Ontario, Canada). Oxygen was extracted from 5-mg samples at 550° to 600°C using the BrF_5 technique of Clayton and Mayeda (1963). Samples were analyzed via dual inlet on a Thermo-Finnigan Delta^{Plus} XP isotope ratio mass spectrometer (IRMS). For hydrogen isotope measurements, samples were weighed into silver capsules, degassed for 1 h at 100°C, and then crushed and loaded into a zero blank autosampler. Hydrogen isotope compositions were measured using a Finnigan thermos-combustion elemental analyzer (EA) coupled to a Thermo-Finnigan Delta^{Plus} XP continuous-flow IRMS. All values are expressed in the conventional δ notation as per mil (‰) deviation from V-SMOW (Vienna-Standard Mean Ocean Water), with analytical precision and accuracy for $\delta^{18}O$ values of ±0.1‰ (1σ) and for δD of ±3‰ (1σ) and ±1.5‰ (1σ), respectively.

Sulfur isotope measurements were conducted on 57 hand-picked mineral separates, including anhydrite, gypsum, barite, chalcopyrite, and sphalerite, at the Westfälische Wilhelms-Universität Münster, Germany (described in detail by Wienkenjohann, 2015). For 35 pure monomineralic samples (as defined optically), the sulfur isotope composition was determined directly without prior chemical treatment, using a Carlo Erba EA interfaced to a ThermoFinnigan Delta Plus mass spectrometer (EA-IRMS). Repeat analyses showed a precision of better than ±0.3‰ (1σ), and standard measurements (IAEA-S1, S2, S3, NBS127, Ag_2S-lab) gave an accuracy of better than ±0.2‰ (1σ). For 22 samples of intergrown sulfide-sulfate mineral assemblages, a mineral-specific, wet-chemical pretreatment protocol was applied, yielding four different sulfur phases. Briefly, anhydrite and gypsum were dissolved using a 10% NaCl-solution for 24 h, and dissolved sulfate was precipitated as $BaSO_4$ using standard procedures (e.g., Dogramaci et al., 2001). $BaSO_4$ precipitates were then converted into silver sulfide using Thode solution (a mixture of HI, HCl, and H_3PO_2; Thode and Monster, 1961). Sphalerite sulfur was liberated as hydrogen sulfide (acid volatile sulfide [AVS]) with HCl (25%) for 1 h at 85°C. Subsequently, disulfides such as chalcopyrite and pyrite were extracted using chromous-chloride solution (chromium-reducible sulfide [CRS] fraction, cf. Canfield et al., 1986). Each time, resulting hydrogen sulfide was precipitated first as zinc sulfide (using zinc acetate) and ultimately as silver sulfide (using silver nitrate) as described in Canfield et al. (1986) and Rice et al. (1993). Following the quantitative removal of all sulfide minerals using acidic (HCl) $CrCl_2$ solution (cf. Canfield et al., 1986), acid-insoluble sulfate (barite) was liberated as hydrogen sulfide, following Thode and Monster (1961), and ultimately precipitated as silver sulfide. All silver sulfide precipitates, representing water-soluble sulfates (WSS) such as anhydrite and gypsum (Ag_2S_{WSS}), acid-insoluble sulfates (AISs) such as barite (Ag_2S_{AIS}), AVSs (i.e., sphalerite), and CRSs (i.e., chalcopyrite and pyrite), were subjected to fluorination IRMS, following the procedure outlined by Ono et al. (2006), using a ThermoScientific Mat 253 mass spectrometer. Results are reported in the standard delta notation as per mil difference relative to Vienna-Canyon Diablo Troilite (V-CDT). Precision and accuracy were better than ±0.03‰ (1σ).

The $^{226}Ra/Ba$ dating of hydrothermal barite from 23 sulfide-sulfate samples was carried out following the methods of Jamieson et al. (2013), modified after Ditchburn et al. (2004). Samples were crushed and powdered, with one split used to

determine Ba concentrations by INAA (described above) and another split used to determine ^{226}Ra activity via gamma spectrometry at the Elemental Tracer Laboratory at the University of Ottawa. The daughter product of ^{226}Ra is ^{222}Rn, with a half-life of 3.8 d. A daughter isotope from the decay of ^{222}Rn, ^{214}Pb, was measured as a proxy to avoid peak overlap with ^{235}U. Prior to measurements, the sample tubes were sealed for 21 d to prevent the escape of ^{222}Rn gas and obtain secular equilibrium between ^{226}Ra and ^{214}Pb. Measurements were made using an XLB-GWL-SV digital gamma spectrometer (DSPec, Ortec®) containing a high-purity germanium crystal, 54.7 × 66.2 mm, with an active well depth of 40 mm. Counting times ranged from 2 to 12 h, depending on the activity of ^{226}Ra in each sample. Spectral signatures were calibrated using IAEA-312 reference material and analyzed using a custom program developed and provided by Peter Appleby (University of Liverpool) to correct for background, detector efficiency, sample volumes, and matrix effects. Ages were determined relative to a zero-age end member selected from one of the actively venting chimneys and assumed to represent the initial ^{226}Ra/Ba ratio (1,022 ± 68 Bq/kg·wt %; sample GMA13-024). All ages are considered minimum values, as incorporation of young barite in the samples cannot be ruled out (e.g., Ditchburn and de Ronde, 2017).

Drill Sites

Shallow seafloor drilling was focused along the main NS-trending fissure (sites A-E), targeting areas with accumulations of chimneys and mounds and spatially associated with buried circular structures that may be manifestations of the cinder cones, with an additional site to the west of this structure (site F) (Fig. 2). Three subseafloor rock types were encountered in most drill holes, in order of increasing depth: (1) unconsolidated volcaniclastic sediment (cover sequence), (2) mineralized intervals consisting of mixed chimney talus, and (3) intensely clay altered volcaniclastic material (footwall sequence). In addition, several drill holes intersected intervals of oxidized ferruginous mud associated with rounded to subrounded chimney fragments, interpreted to be paleoseafloor horizons.

Site A

Site A is a local topographic high at the northern end of the row of craters. It rises ~10 m above background sediments over an area of ~100 × 80 m (Figs. 2, 5A). Chimneys and mounds are distributed around what may be a buried crater, partially covered by volcaniclastic material. The volcaniclastic cover sequence (up to 13.8 m thick) is underlain by 0.7 to 2.6 m of chimney talus, followed by intensely clay altered monomictic lapillistone that is crudely bedded with both matrix-supported and clast-supported intervals, extending to the bottom of the drill holes. The northernmost drill hole, TKAD001, is located next to an active chimney complex and reaches a depth of 22.3 m below seafloor (b.s.f.; App. Fig. A2). The upper ~14 m consists of variably altered volcaniclastic cover material with three discrete oxidized intervals, followed by altered lapillistone. The upper part of the clay-altered lapillistone sequence is unconsolidated to poorly consolidated, with increasing cementation by anhydrite downhole, and is cut by a few anhydrite veins (2–5 mm wide). Disseminated sulfides (pyrite, sphalerite, and minor chalcopyrite, galena, covellite, and bornite) occur with anhydrite that has been partly hydrated to gypsum, both in the cement and in the vein fill. To the south of this drill hole, TKAD015 and TKAD027 were drilled in close proximity (~3 m apart) to a maximum depth of 7.3 m b.s.f., next to a partially buried chimney complex. The volcaniclastic cover is <1 m thick and contains fragments of chimney material, likely sourced by mass wasting from nearby (unknown) chimneys (App. Figs. A3, A4). The mineralized interval is a ~1.5- to 2.6-m-thick layer of chimney talus. As in TKAD001, intensely clay altered and poorly sorted lapillistone occurs below the chimney talus in both drill holes. TKAD028, located ~20 m east of TKAD015/027, intersected 0.5 m of volcaniclastic cover material, followed at depth by a narrow (0.7 m) sulfide interval dominated by barite and sphalerite at the top and becoming pyrite rich downhole (App. Fig. A5). This mineralized interval appears to correlate between the drill holes. The clay-altered lapillistone at the bottom of the hole is similar but better sorted than that found in TKAD015/027. Approximately 30 m to the east, TKAD029 encountered only the variably altered volcaniclastic cover material to a depth of 7.8 m b.s.f. (App. Fig. A6). This drill hole is located at the edge of the low-relief cinder cone where the volcaniclastic cover is thickest.

Site B

Site B is another crater-like feature (70 × 80 m) on a cone at the north end of the row of cinder cones (Figs. 2, 5B). Chimneys and mounds occur along the crater walls and on the outer flanks of the cone and are variably covered by volcaniclastic material. Here, massive sulfide chimneys occur on top of chimney talus. At the western edge of the crater, TKAD016 intersected thin (0.2 m) volcaniclastic cover, followed by a layer of pyritic chimney talus ~0.4 m thick and then poorly sorted and crudely bedded monomict, matrix-supported, and intensely clay altered lapillistone (App. Fig. A7). The upper part of the lapillistone is cemented mainly by gypsum with a few large crystals up to 7 mm long; the lower part is mostly unconsolidated with patchy anhydrite cement that has been partially hydrated to gypsum, a few crosscutting veinlets of anhydrite, weak silicification, and disseminated sulfide minerals (pyrite with minor sphalerite near the top and minor to trace chalcopyrite near the bottom). At the southern wall of the crater, TKAD026 intersected massive sphalerite-barite chimney material to a depth of 1.4 m b.s.f. (App. Fig. A8). The substrate of lapillistone contains minor patchy barite cement in the upper part and anhydrite cement in the lower part, with gray-white clay alteration that generally decreases downhole. At the center of the crater, the mineralized interval of chimney talus is thicker (up to ~3.9 m) in TKAD013, cemented by anhydrite-rich and clay-altered mud and fine-grained sulfide minerals (App. Fig. A9). This interval was not recovered in TKAD025 (located ~3.6 m away) owing to poor drilling conditions (App. Fig. A10). In the center of the crater, intensely clay altered lapilli with minor disseminated sulfides occur to ~4 m b.s.f., below which is a chaotic mixture of matrix-supported volcanic and chimney fragments. The volcanic clasts are polymict (altered and unaltered), subangular to angular, and variably infilled by late-stage silica. Several short intervals within the lapilli units contain gypsum crystals up to

3 cm long. On the upper rim of the volcanic cone in the east, a thin (0.6 m) cover of unconsolidated volcaniclastic material is directly underlain by altered monomict lapillistone, with increasing sulfate cement and decreasing alteration intensity downhole to a depth of 7.4 m b.s.f. (see TKAD012, App. Fig. A11). At this site, there are fewer disseminated sulfides compared to the other drill holes and decreasing sphalerite abundance downhole.

Site C

Site C is a large volcanic cinder cone, rising to ~70 m above the seafloor and with a diameter of ~120 × 90 m (Figs. 2, 5C, D). Chimney complexes and mounds occur on the flank of this cone in the vicinity of a circular slump feature. TKAD032 intercepted unconsolidated volcaniclastic cover material to 1.8 m, followed by intensely altered volcaniclastic breccia to 6.9 m b.s.f. (App. Fig. A12). The altered sequence consists of monomict lapillistone with subrounded to subangular vesicular clasts but variable clay alteration. The uppermost lapillistone is matrix supported with variable sulfate cement and veins and disseminated pyrite, sphalerite, and chalcopyrite (decreasing downhole). Several horizons are clast supported (up to 60% clasts), with angular monomict clasts, and appear to be autobreccias. One gypsum-rich interval occurs at 6.4 to 6.6 m b.s.f. TKAD033 was drilled at the edge of a small crater or collapse feature near the summit of the cone. The recovered rock types are similar to those in TKAD032, with a transition between the volcaniclastic cover and the clay-altered footwall occurring at 1.1 m b.s.f. (App. Fig. A13). Variable alteration intensity gives this rock a polymict appearance.

Site D

Site D is an irregularly shaped topographic high, ~70 × 80 m in diameter, in the saddle between two cinder cones (Figs. 2, 5C, D). Chimneys occur on the north flank, where there is local venting of milky fluids from fractures near the base of the chimneys. On the northern side of the chimney cluster, TKAD017 intersected unconsolidated volcaniclastic cover material to ~1.4 m, separated from an interval of chimney talus by a layer of oxidized mud and chimney fragments (App. Fig. A14). The chimney talus extends to a depth of 5.2 m b.s.f. but is interrupted by a second layer of oxidized mud at depths of 2.6 to 3.3 m b.s.f. The altered footwall comprises subrounded, matrix-supported, monomict lapilli-sized clasts with minor disseminated pyrite and patchy anhydrite + gypsum cement that increases downhole to a depth of 7.4 m b.s.f. A few subrounded fragments of chimneys are also found in the footwall. The upper oxidized layer between the cover sequence and the mineralized interval can be traced ~20 m eastward to TKAD030 (App. Fig. A15). The lower oxidized layer was not recovered at TKAD030; instead, a buried sphalerite-rich chimney was intersected. The drilled sphalerite-rich chimney is underlain by chimney talus, which appears to be continuous with material in TKAD017. Altered lapillistone to 5.3 m b.s.f. consists of several beds that are distinguished by changes in grain size and proportion of clasts to matrix and by a higher proportion of sulfate cement. The two oxidized intervals encountered in TKAD017 were also traced 25 m to the south in TKAD031 (App. Fig. A16). The volcaniclastic cover sequence is absent in this drill hole, but a large chalcopyrite- and sphalerite-rich chimney block that likely came from a chimney complex located upslope to the south was drilled. The uppermost layer of chimney talus was similarly encountered here, extending to a similar depth (~5 m b.s.f.). The cover sequence is also absent in TKAD018 to the east. This hole started in oxidized chimney talus that is continuous with the uppermost oxidized interval in the other drill holes (App. Fig. A17). The chimney talus here is only ~0.6 m thick, grading to the clay-altered footwall at 1.2 m b.s.f. The clay-altered lapillistone at this location contains a higher proportion of fine-grained material (tuff). In the southeast, TKAD019 encountered only unconsolidated volcaniclastic cover material (to 6.1 m b.s.f.) that accumulated within a topographic low at the periphery of a chimney cluster (App. Fig. A18). Within the thick accumulation of cover material, there are several distinct intervals of intensely oxidized sediment, which may be continuations with the oxidized layers in the other holes.

Site E

Site E is on the southernmost cinder cone near several small craters (Figs. 2, 5E). TKAD005 is near an inactive chimney complex on the eastern margin of the northernmost crater; TKAD003 is on a small ridge south of TKAD005, near a scarp that may be a crater wall or slump and adjacent to a site of active venting. Both drill holes recovered moderately sorted, clast-supported, monomict lapillistone with weak grading and intense clay alteration. The matrix consists of anhydrite cement with minor disseminated sphalerite and pyrite that decrease in abundance downhole and are locally oxidized to hematite.

Site F

Site F is located west of the main NS-trending fissure, where chimneys and mounds are aligned in a circular pattern, but constructional volcanic features are absent (Figs. 2, 5F). TKAD007 was drilled next to a site of active venting in a sequence of clast-supported, clay-altered monomict lapillistone characterized by moderately sorted subangular clasts. The lapillistone is cemented by anhydrite, which increases in abundance downhole and is locally fracture controlled. The breccia also contains minor disseminated pyrite and fracture-controlled patchy iron oxide. A few centimeter-wide pyrite-chalcopyrite veinlets associated with the most intense clay alteration occur at the top of the recovered core. Inactive chimney complexes and mounds surround the area of active venting and appear to be aligned along structural corridors (Fig. 2). TKAD008 is located along one of these NW-SE–trending structures, 102 m south of TKAD007, on a low-relief ridge with numerous inactive chimney complexes and mounds. The upper part is matrix-supported lapillistone that grades downhole into a clast-supported lapillistone similar to that in TKAD008. Increasing clast size and angularity and decreasing alteration intensity downhole suggest that this drill hole may be at the periphery of the main hydrothermal upflow zone.

Seafloor and Subseafloor Mineralization

Isolated chimney complexes throughout the Tinakula area are most common on steep slopes that have not been completely buried by the volcaniclastic cover. Four main chimney types

are recognized: (1) chalcopyrite rich, (2) zoned (with variable proportions of chalcopyrite and sphalerite), (3) sphalerite-rich chimneys, and (4) barite rich and/or silica altered (details in App. Table A1; App. Fig. A19). Unlike the subseafloor breccia facies, the seafloor chimneys contain only minor anhydrite and gypsum. Different chimney types commonly occur together; however, higher-temperature Cu-rich chimneys are more abundant near sites A and D, and lower-temperature barite-rich chimneys are common at site B (App. Fig. A20). Mineralized volcanic breccia was recovered from the base of several chimney complexes, where the chimneys have overgrown volcaniclastic material.

The Cu-rich chimneys comprise abundant, massive, coarse-grained chalcopyrite with minor pyrite (Fig. 7A-C). Locally, minor Fe-poor sphalerite and barite line the chimney conduits. In one sample, trace amounts of microscopic gold are present as inclusions in the chalcopyrite (sample GMA13-048; Fig. 7C). Distinctly zoned chimneys have layers that are chalcopyrite, pyrite (± marcasite), and sphalerite rich (Fig. 7D-F). Both Fe-rich and Fe-poor sphalerite occur in different layers. The low-Fe sphalerite commonly has inclusions of fine-grained Pb-As-Sb sulfosalts (jordanite) and minor galena. Late-stage, coarse tabular barite, amorphous silica, and iron oxyhydroxides occupy open spaces.

The Zn-rich chimneys are most abundant and consist of dendritic sphalerite and barite with pyrite and marcasite (Fig. 7G-I). These chimneys lack clearly defined vent conduits but have alternating layers of low- and high-Fe sphalerite, similar to beehive chimneys that form by diffuse fluid venting (e.g., Koski et al., 1994). The low-Fe sphalerite commonly contains inclusions of jordanite and galena; fine-grained inclusions of chalcopyrite are present at grain boundaries but are rare. Late-stage tabular barite is followed paragenetically by minor amounts of amorphous silica and trace iron and manganese oxyhydroxides. The Ba-rich chimneys also form bulbous and beehive-like structures with variable amounts of amorphous silica filling or lining open spaces (Fig. 7J-L).

Chalcopyrite and pyrite show little compositional variation, although As is relatively enriched in both pyrite (up to 1.42 wt %) and marcasite (up to 2.71 wt %) (App. Table A2). Mercury is also present above detection limits in pyrite, together with Pb and Sb. FeS contents of sphalerite range from 0.02 to 13.98 mol %, with more than 50% of the analyses reporting <2 mol % FeS (Fig. 8). The most Fe-rich sphalerite is in chalcopyrite-rich assemblages, and the widest range of FeS values occur in the dendritic barite-rich chimneys. Cadmium (up to 2.04 wt %), In (up to 1.31 wt %), Ga (up to 1.03 wt %), and Hg (up to 1.28 wt %) are likely present in solid solution in the sphalerite (e.g., Cook et al., 2009). Cadmium concentrations in sphalerite decrease from an average of 0.33 wt % in the chalcopyrite-rich chimneys (n = 16) to 0.03 wt % in the dendritic barite-rich chimneys (n = 79), suggesting a strong temperature dependence, which is also reflected in the Fe content. Galena contains up to 1.23 wt % Ag, mainly in the barite-rich chimneys. The Pb-As-Sb sulfosalts have up to 11.91 wt % As and 0.28 wt % Sb, which is close to those of the As end member of the jordanite-geocronite series (cf. Biagioni et al., 2016).

Bulk compositions of the seafloor chimneys and mineralized volcanic breccias are listed in Table 1. The seafloor chimneys contain abundant Zn up to 52.60 wt % (avg 19.20 wt %; n = 36) and Cu up to 30.00 wt % (avg 5.82 wt %; n = 36) but generally low Pb (<0.01–2.93 wt % Pb; avg 0.35 wt %; n = 36; Fig. 9) compared to other modern back-arc basin sulfide deposits (cf. Hannington et al., 2005; Monecke et al., 2016). Calcium concentrations are low in the chimneys (avg 0.06 wt %; n = 36), but Ba (avg 6.49 wt %; n = 36) and Sr (avg 2,157 ppm; n = 36; up to 0.85 wt % in barite-rich samples) are high. The SiO_2 contents average 11.67 wt % (n = 36), but one chimney contains 75.09 wt % SiO_2 together with 1.75 wt % Ba. The Cu-rich chimneys have high Mo (avg 343 ppm; n = 2) and In (avg 262 ppm; n = 2), with high Au (9,260 ppb) present in one sample. The Zn-rich samples contain very high Ga (up to 1,540 ppm), Ge (up to 99 ppm), Hg (up to 95 ppm), and Se (up to 20 ppm). Concentrations of Ag, Sb, As, and Au are also higher than in the Cu-rich chimneys, although high As is found in both Zn- and Cu-rich samples. Mercury concentrations are especially high in samples containing marcasite and late sphalerite + galena. The four sampled barite-rich chimneys also have high Pb (avg 7,073 ppm), As (avg 299 ppm), Sb (avg 82 ppm), Au (avg 2,038 ppb), and Ag (avg 121 ppm). Statistical correlations between the different trace elements clearly reflect the higher (>250°C) and lower temperatures (<250°C) of the Cu-rich and Zn-rich assemblages, respectively (App. Figs. A21, A22), as well as various lattice substitutions in the corresponding minerals (e.g., Cd in sphalerite, Sr in barite, As and Sb in Pb-rich sulfosalts, etc.; App. Table A2; cf. Hannington et al., 2005; Monecke et al., 2016). Gallium is incorporated mainly in galena in low-temperature assemblages, whereas in higher-temperature assemblages it mainly resides in sphalerite with moderate to high Fe contents. Arsenic is high in low-temperature assemblages, reflecting the presence of As in low-temperature minerals such as galena and sulfosalts. In a single sample containing secondary bornite (chalcopyrite-rich chimney GMA13-010), Ag concentrations are 1,253 ppm. Contents of Co, Ni, Sn, W, Bi, and Te are generally below detection limits in all samples, unlike other arc-related hydrothermal systems that commonly contain discrete Bi and Te minerals, e.g., Monecke et al. (2016).

Subseafloor mineralization consists of (1) unconsolidated and locally hydrothermally cemented chimney talus (Fig. 10A, B), (2) chimney talus, mixed with altered volcanic clasts, that is generally hydrothermally cemented (Fig. 10C), (3) chimney talus associated with oxidized intervals (Fig. 10D), (4) disseminated to patchy sulfides (chalcopyrite, pyrite, sphalerite) within altered volcaniclastic rocks (Fig. 10E, F), and (5) sulfide minerals associated with late sulfate veins that extend to maximum depths of ~21 m b.s.l. (e.g., Figs. 3E, 4G, H; App. Fig. A2). Drilling shows that the majority of the mineralization at Tinakula comprises chimney talus that occurs directly beneath the unconsolidated volcaniclastic material (generally between 0.6 and 5.3 m b.s.f.). The oxidized intervals contain variable amounts of sulfide material (mostly chimney talus). Disseminated and vein-controlled sulfide mineralization (pyrite, chalcopyrite, and sphalerite) occur in the upper ~0.5 to 2.6 m of most drill holes (e.g., Fig. 4F, G). Seven samples of mineralized volcanic breccia down to 5.8 m b.s.f. contain mostly pyrite (9.7–30.1 wt % sulfide S) with minor anhydrite accounting for ~0.1 to 0.5 wt % sulfate S. Taking into account the dilution from wall rock, mineralized portions of the

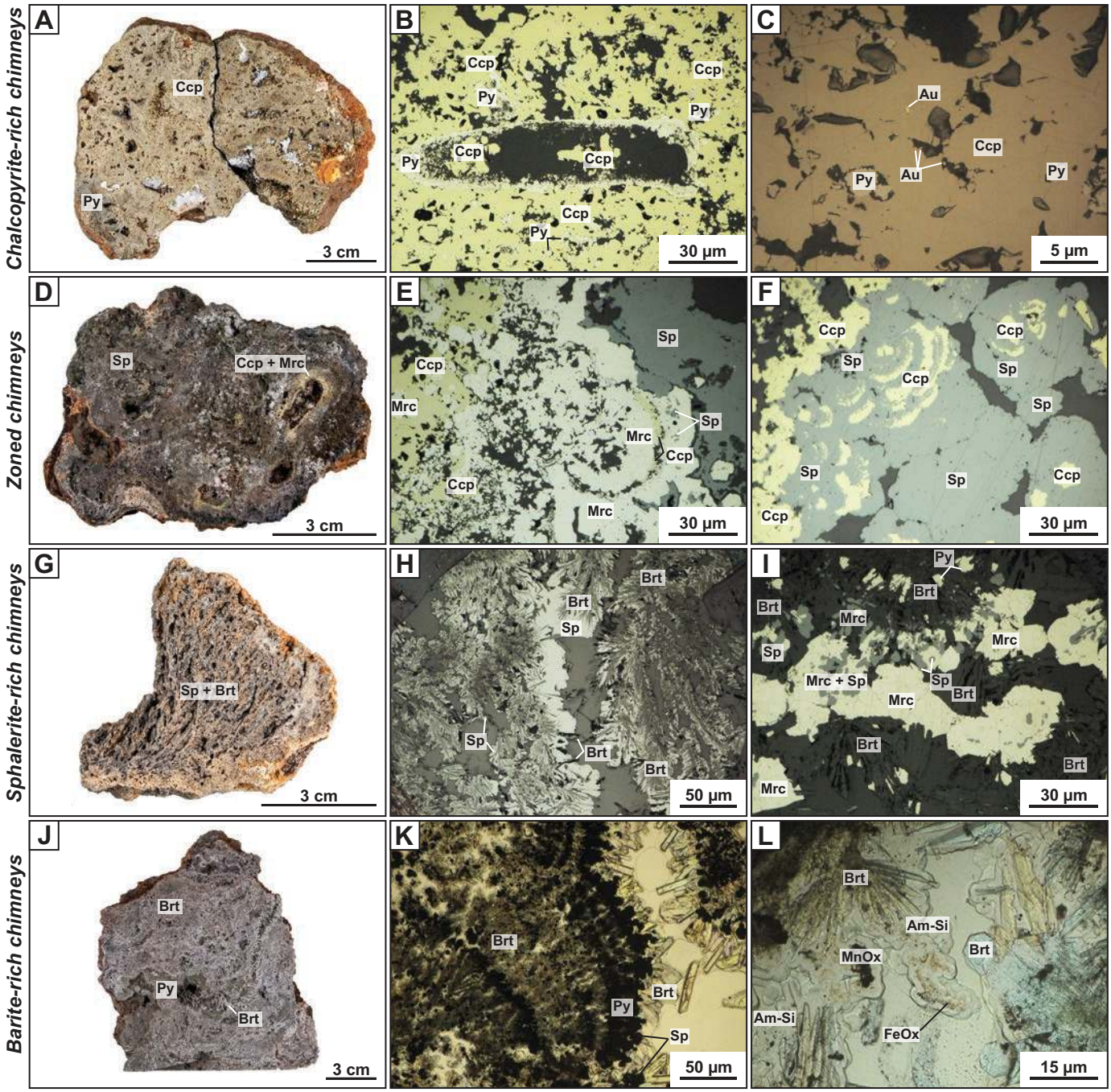

Fig. 7. Features of chimney types at the Tinakula deposit with high porosities reflecting fluid channels. (A) Hand sample photo of chalcopyrite-rich chimney (sample GMA13-048). (B) Reflected-light in plane-polarized light (RL-PPL) photomicrograph of chalcopyrite-rich chimney with pyrite lining former vent conduit (sample GMA13-038). (C) RL-PPL photomicrograph of chalcopyrite-rich chimney with fine-grained gold inclusions within chalcopyrite (sample GMA13-048). (D) Hand sample photo of zoned chimney (sample GMA13-031). (E) RL-PPL photomicrograph of zoned chimney with chalcopyrite, marcasite (filling former vent conduit), and sphalerite (sample GMA13-050). (F) RL-PPL photomicrograph of zoned chimney with banded chalcopyrite and sphalerite (sample GMA13-031). (G) Hand sample photo of sphalerite-rich chimney (sample GMA13-012). (H) RL-PPL photomicrograph of dendritic to acicular barite, followed by sphalerite with minor late barite (sample GMA13-022). (I) RL-PPL photomicrograph of sphalerite-rich chimney, with early barite + spherulitic pyrite, followed by coarse-grained barite, and marcasite replaced by sphalerite (zone refining), with a late generation of globular sphalerite + galena (not shown) (sample GMA13-058). (J) Hand sample photo of barite-rich chimney (sample GMA13-045). (K) Transmitted-light in plane-polarized light (TL-PPL) photomicrograph of banded dendritic barite + pyrite, with minor sphalerite, and late tabular barite (sample GMA13-018B). (L) TL-PPL photomicrograph of dendritic to radial barite, tabular barite, and late amorphous silica with very fine grained inclusions of iron and manganese oxyhydroxides (sample GMA13-009B). Abbreviations: Am-Si = amorphous silica, Au = gold, Brt = barite, Ccp = chalcopyrite, Fe-MnOx = iron and manganese oxyhydroxides, Mrc = marcasite, Py = pyrite, Sp = sphalerite.

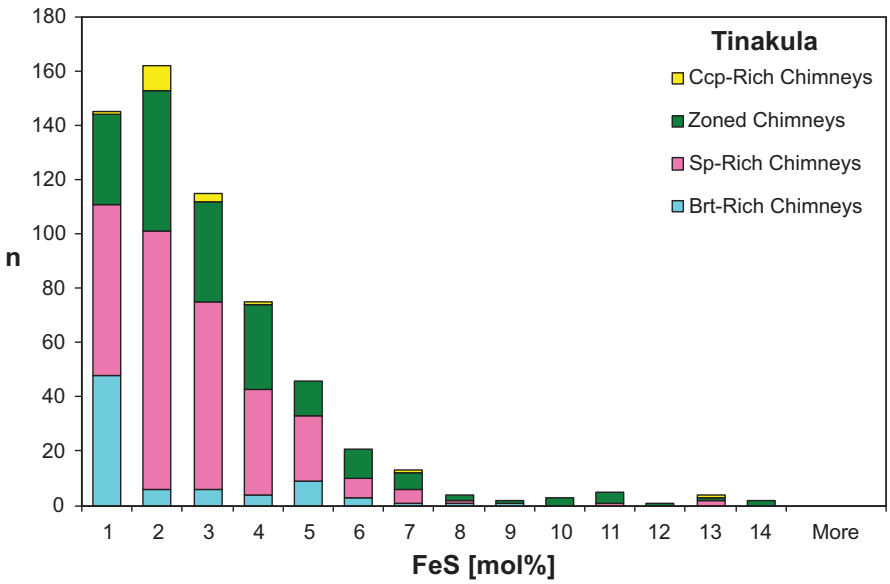

Fig. 8. Frequency histograms of FeS (mol %) concentrations in sphalerite (uncorrected for chalcopyrite inclusions) from different chimney types at the Tinakula deposit (n = 598), calculated following Scott and Barnes (1971). Abbreviations as in Figure 7.

samples contain slightly higher Co and Se and lower Cd, Hg, Sb, and Ag than the seafloor chimneys, consistent with higher temperatures of mineralization (e.g., Monecke et al., 2016).

The chimney talus and oxidized intervals appear continuous between drill holes at sites A, B, and D, but mineralization was not encountered in the two drill holes at site C (Figs. 11, 12). Since the drill platform required relatively flat slopes, drilling at this site was limited to the areas beside the known chimney mounds. Therefore, the occurrence of chimney talus below the mounds was not confirmed at the location. The buried sulfide mineralization is estimated to have an area at least three times larger than that of the seafloor chimneys and mounds, although more drilling is required to establish the full extent and continuity.

Subseafloor Alteration

Below the mineralized interval, the volcaniclastic breccias have been intensely hydrothermally altered, with clay minerals occurring as replacements of volcanic material and infills of pore spaces (e.g., Fig. 4D-F). The predominant

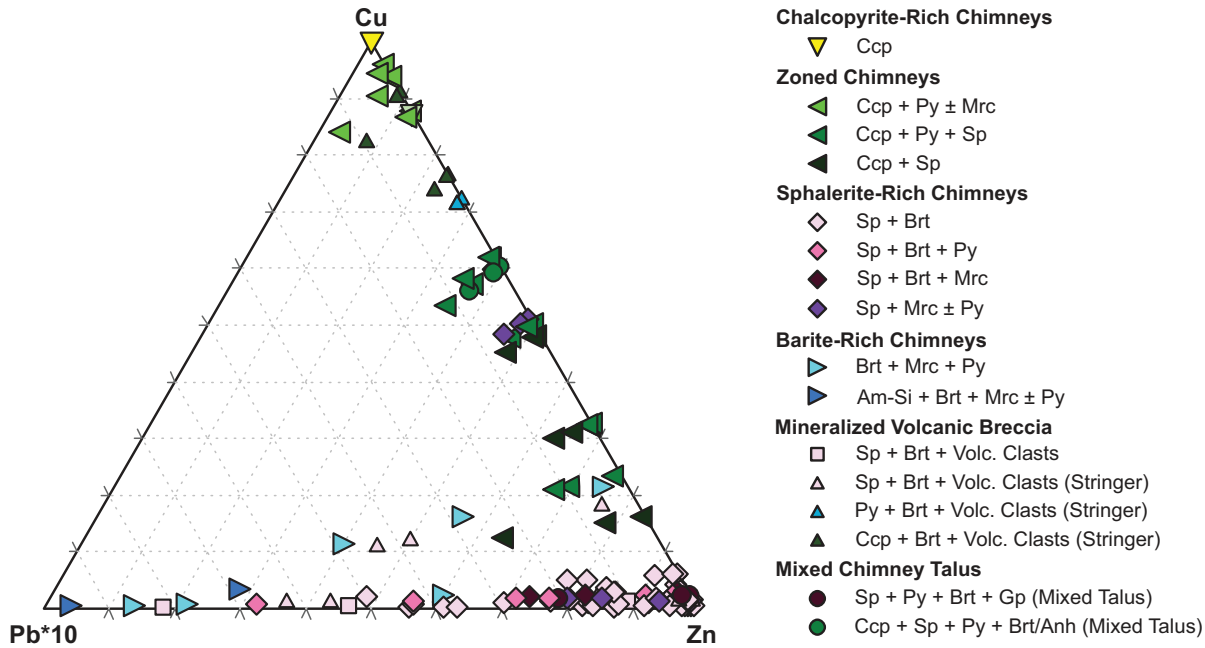

Fig. 9. Ternary diagram of Cu, Pb, and Zn concentrations in bulk whole-rock chimney samples from the Tinakula deposit, classified according to sample type (see text for classification). Abbreviations: Anh = anhydrite, Gp = gypsum, Volc. = volcanic; others as in Figure 7.

Table 1. Average Whole-Rock Geochemistry of Sulfide-Sulfate Samples by Chimney Type at Tinakula Deposit

		Chalcopyrite-rich	Zoned chalcopyrite-rich			Dendritic sphalerite-rich				Barite-rich
		Ccp $n = 2$	Ccp + Py ± Mrc $n = 3$	Ccp + Mrc + Sp $n = 5$	Ccp + Sp $n = 3$	Sp + Brt $n = 13$	Sp + Brt + Py $n = 1$	Sp + Brt + Mrc $n = 2$	Sp + Mrc/Py $n = 3$	Brt + Mrc ± Py $n = 2$
S_{Total}	wt %	33.3	35.4	34.4	27.6	23.0	19.8	21.9	30.1	35.8
Au	ppb	4,692	1,014	2,670	3,517	1,133	4,270	5,455	3,510	3,905
Fe	wt %	25.65	27.97	21.78	12.05	2.88	2.10	6.60	14.80	22.80
Cu	wt %	30.00	17.03	10.14	10.52	0.68	0.81	0.38	1.52	0.51
Mo	ppm	343	85	53	66	14	110	46	67	11
In	ppm	262	59	57	125	14	27	5	5	<0.2
Ni	ppm	<10	<10	<10	<10	<10	10	20	<10	<10
Bi	ppm	<2	<2	<2	<2	<2	<2	<2	<2	<2
Co	ppm	2	<0.2	<0.2	<0.2	<0.2	<0.2	<0.2	2	1
Zn	wt %	1.99	1.54	1.54	21.50	30.92	27.10	15.61	25.02	3.39
Cd	ppm	144	61	15.12	963	1,008	1,120	601	761	155
Ga	ppm	23	21	682	91	31	65	18	26	13
Ge	ppm	9	24	72	74	69	51	30	50	21
Se	ppm	9	8	54	11	13	12	11	13	7
Tl	ppm	1	26	12	32	17	8	38	47	11
Pb	ppm	44	428	1,401	1,927	4,441	5,300	6,600	2,444	12,600
Hg	ppb	535	11,080	30,122	10,697	19,145	6,480	19,050	35,100	27,300
As	ppm	54	568	1,091	579	641	425	567	625	488
Sb	ppm	9.3	55	158	193	143	179	364	299	119
Ag	ppm	42	42	66	138	139	124	272	112	210
Te	ppm	<6	<6	<6	<6	<6	<6	<6	<6	<6
Sn	ppm	14	6.3	19	5	9	4	1	<0.5	<0.5
W	ppm	7	1	4	2	3	1	<0.7	<0.7	<0.7
Ba	wt %	0.05	0.65	1.10	4.06	9.49	9.15	13.49	2.33	8.58
Ca	wt %	0.02	0.03	0.05	0.04	0.07	0.06	0.11	0.08	0.08
Sr	ppm	3	209	434	1,445	2,781	2,730	6,235	1,539	4,135
Mg	wt %	0.03	0.02	<0.01	<0.01	<0.01	<0.01	<0.01	<0.01	<0.01
Mn	ppm	10	205	41	189	36	227	311	2,338	578
K	wt %	<0.1	<0.1	<0.1	<0.1	<0.1	<0.1	<0.1	<0.1	<0.1
Na	wt %	0.09	0.15	0.11	0.19	0.07	0.21	0.10	0.16	0.04
Si	wt %	0.6	3.3	3.2	5.1	4.3	9.1	5.0	6.7	2.3
Al	wt %	0.22	0.21	0.18	0.10	0.03	0.17	0.17	0.09	0.02
Ti	wt %	<0.01	<0.01	<0.01	<0.01	<0.01	<0.01	<0.01	<0.01	<0.01
V	ppm	37	43	27	35	19	59	20	39	24
P	wt %	0.053	0.033	0.017	0.022	<0.005	0.012	<0.005	0.053	0.007

		Silicified barite-rich	Mineralized volcanic breccia	Mineralized volcanic breccia-stringer			Mixed chimney talus	
		Am-Si + Brt + Mrc/Py $n = 2$	Sp + Brt + Volc. Clasts $n = 1$	Sp + Brt + Volc. clasts $n = 3$	Py + Brt + Volc. clasts $n = 1$	Ccp + Brt + Volc. clasts $n = 2$	Sp + Py + Brt + Gp $n = 1$	Ccp + Sp + Py + Brt/Anh $n = 1$
S_{Total}	wt %	5.1	10.2	17.4	13.7	24.9	22.2	31.7
Au	ppb	171	221	2,397	1,220	255	356	552
Fe	wt %	2.35	1.39	5.09	11.70	18.95	0.91	22.20
Cu	wt %	0.02	0.05	0.77	5.40	10.18	0.86	7.86
Mo	ppm	9	10	29	17	163	22	143
In	ppm	<0.2	2	9	48	44	<0.2	30
Ni	ppm	<10	<10	<10	<10	<10	<10	<10
Bi	ppm	<2	<2	<2	<2	<2	<2	<2
Co	ppm	2	6	2	7	11	<0.2	2
Zn	wt %	0.23	3.39	16.74	2.09	2.45	35.60	5.16
Cd	ppm	3	20	562	77	109	1,610	263
Ga	ppm	4	9	20	33	19	3	24
Ge	ppm	2	22	79	11	19	66	32
Se	ppm	1	5	10	8	10	12	12
Tl	ppm	12	6	27	3	15	<0.1	49
Pb	ppm	1,545	3,890	6,918	97	79	539	217
Hg	ppb	35,880	25,200	23,103	1,770	905	13,700	1,070
As	ppm	112	221	830	441	255	659	306
Sb	ppm	46	47	243	19	13	530	14
Ag	ppm	32	56	110	<5	<5	401	bdl
Te	ppm	<6	<6	<6	<6	<6	<6	<6
Sn	ppm	<0.5	<0.5	<0.5	1	1	3	11
W	ppm	1	10	11	2	5	5	8

Table 1. *(Cont.)*

		Silicified barite-rich	Mineralized volcanic breccia	Mineralized volcanic breccia-stringer			Mixed chimney talus	
		Am-Si + Brt + Mrc/Py $n = 2$	Sp + Brt + Volc. Clasts $n = 1$	Sp + Brt + Volc. clasts $n = 3$	Py + Brt + Volc. clasts $n = 1$	Ccp + Brt + Volc. clasts $n = 2$	Sp + Py + Brt + Gp $n = 1$	Ccp + Sp + Py + Brt/Anh $n = 1$
Ba	wt %	15.18	15.40	6.02	0.09	0.71	9.42	0.97
Ca	wt %	0.11	0.64	0.13	0.09	0.09	0.04	0.02
Sr	ppm	3,137	5,060	2,038	6	164	1,740	303
Mg	wt %	0.03	0.27	0.01	0.08	0.04	<0.01	<0.01
Mn	ppm	63	272	58	12	36	11	192
K	wt %	<0.1	<0.1	<0.1	0.8	0.3	<0.1	<0.1
Na	wt %	0.23	0.43	0.19	0.26	0.14	0.10	0.04
Si	wt %	27.0	12.2	15.6	25.5	14.5	1.7	10.9
Al	wt %	0.14	1.79	0.55	2.95	1.30	0.09	0.13
Ti	wt %	<0.01	0.11	0.05	0.33	0.10	<0.01	<0.01
V	ppm	27	109	44	160	94	18	66
P	wt %	<0.005	0.019	<0.005	0.009	0.020	<0.005	0.012

Abbreviations: Am-Si = amorphous silica, Anh = anhydrite, bdl = below detection limit, Brt = barite, Ccp = chalcopyrite, Gp = gypsum, Mrc = marcasite, Py = pyrite, Sp = sphalerite, Volc. = volcanic

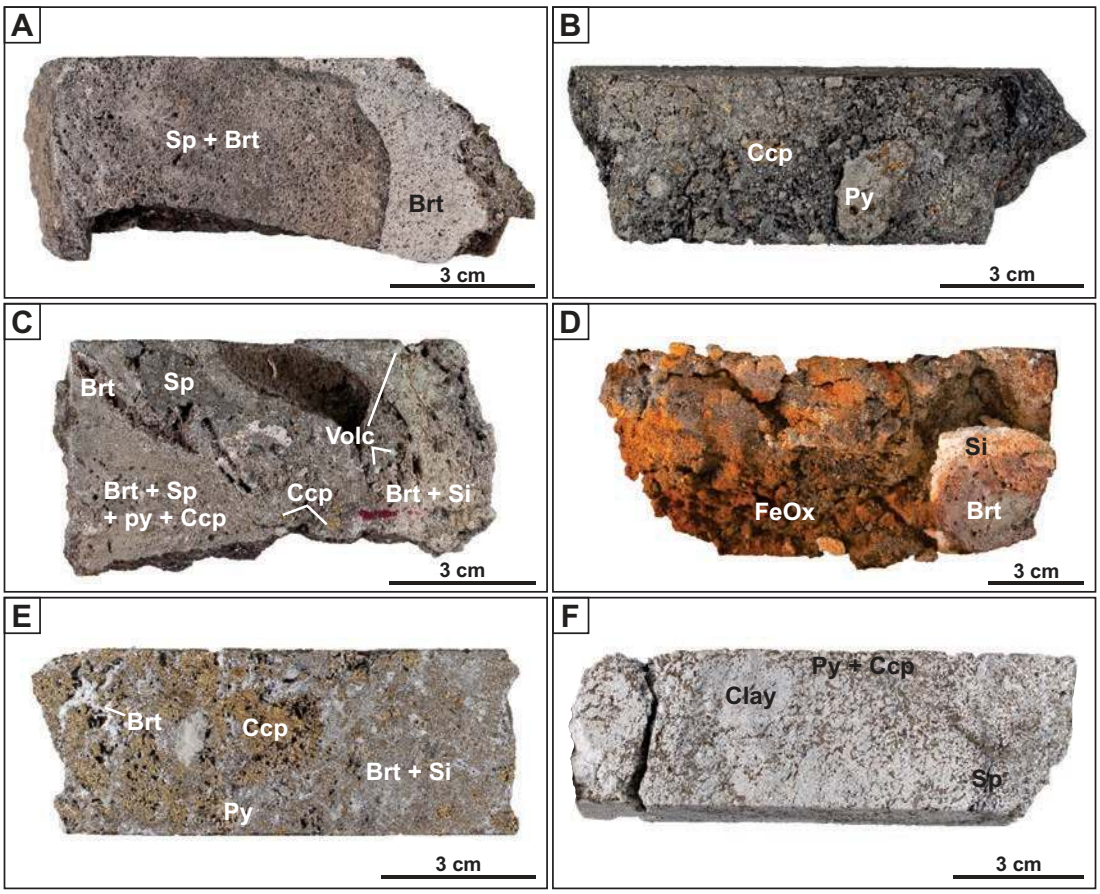

Fig. 10. Subseafloor mineralization at the Tinakula deposit. (A) Fragment of barite- and sphalerite-rich chimney with a 3-cm-wide barite rim preserved in drill core (sample MA13-011). (B) Chimney talus with clasts of various sizes, shapes, and mineralogy, cemented by fine-grained sulfides and minor sulfates (sample MA13-030). (C) Clastic massive sulfides with sphalerite, chalcopyrite, and pyrite, and altered volcanic clasts, hydrothermally cemented by barite and fine-grained amorphous silica (sample MA13-032). (D) Oxidized unit characterized by abundant orange iron oxides and chimney fragments (bottom right: fragment of barite- and silica-rich chimney), with variable rounding from transport (sample MA13-022). (E) Barite-rich silicified volcaniclastic breccia with abundant chalcopyrite + pyrite (sample P011). (F) Lapilli-rich volcaniclastic tuff intensely altered to white clay, with disseminated pyrite, chalcopyrite, and minor sphalerite (sample MA13-013). Abbreviations: Si = amorphous silicon; others as in Figure 7.

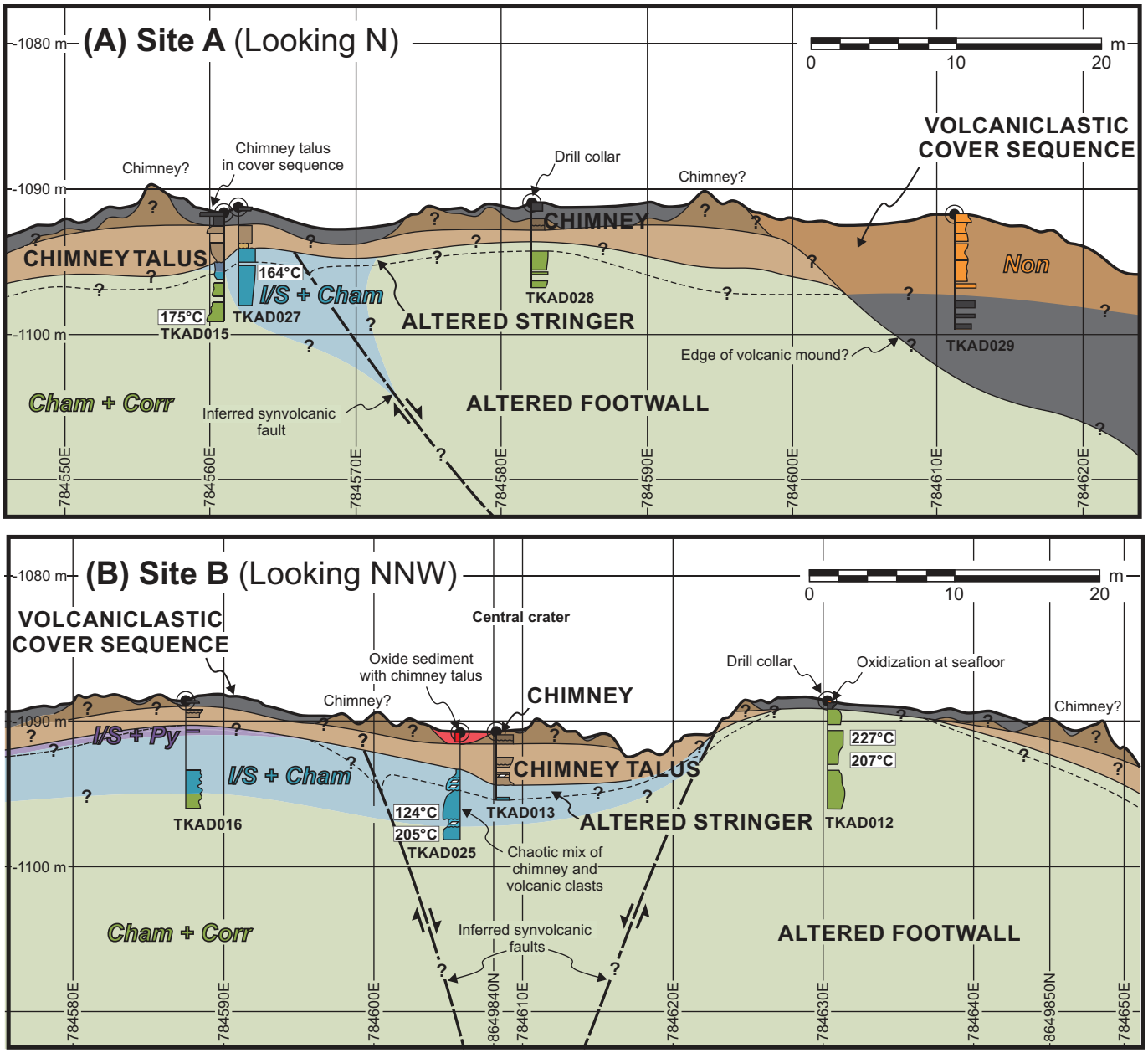

Fig. 11. Cross sections of the geology and alteration types interpreted from drill core (collars shown by circles), seafloor morphologies, and seafloor observations from (A) site A (looking north) and (B) site B (looking north-northwest). Cross section locations are shown in Figure 5A, B. Temperatures are calculated from $\delta^{18}O$ data. Abbreviations: Cham = chamosite, Corr = corrensite, I/S = illite/smectite, Non = nontronite, Py = pyrite. Datum: WGS84 Zone 58S.

lithology of the footwall is monomict to polymict lapillistone that is crudely bedded with both matrix- and clast-supported horizons. Alteration and late infill by patchy sulfate cement obscures many of the primary volcanic textures, resulting in a high degree of uncertainty regarding facies interpretations. The altered volcaniclastic material extends to maximum drilled depths of 22.32 m b.s.f.; however, the full depth and areal extent of the alteration is unknown, with most of the drilling having been focused along the central row of cinder cones (sites A-E; Fig. 2). Alteration minerals in the footwall breccias identified by XRD include dioctahedral smectite (montmorillonite and nontronite), chlorite (mainly chamosite, with minor clinochlore), minor chloritoid, illite, and mixed-layer clays: illite/smectite, muscovite/illite (rectorite), and chlorite/smectite (corrensite) (Table 2; App. Fig. A23). These minerals constitute five alteration facies that are distinguished in drill core by different colors (Table 2): (1) montmorillonite/nontronite, with yellow-orange, yellow-gray, and red-brown hues; (2) nontronite + corrensite, with greenish-yellow to greenish-gray hues; (3) illite/smectite + pyrite, with yellowish-gray to olive-gray hues; (4) illite/smectite + chamosite, with bluish-white, olive, olive-gray, and greenish-yellow hues; and (5) chamosite + corrensite, with greenish-yellow to pale olive, with minor brown to reddish-brown hues.

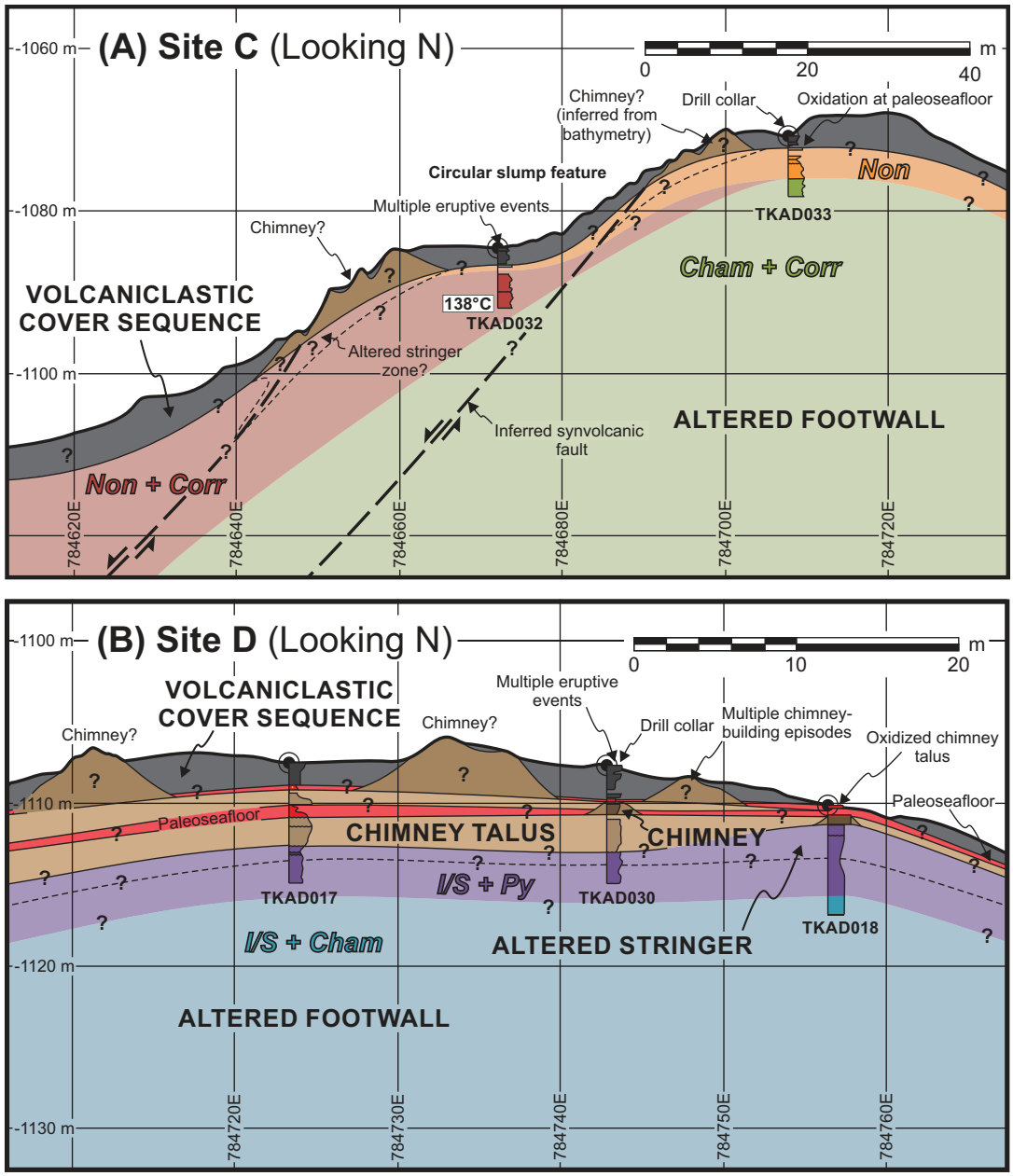

Fig. 12. Cross sections of the geology and alteration interpreted from drill core (collars shown by circles), seafloor morphologies, and seafloor observations from (A) site C (looking north) and (B) site B (looking north). Cross section locations are shown in Figure 5C, D. Temperatures are calculated from $\delta^{18}O$ data. Abbreviations as in Figure 11. Datum: WGS84 Zone 58S.

The alteration assemblages vary with location and depth, generally progressing downward from the seafloor in the order montmorillonite/nontronite to nontronite + corrensite, to illite/smectite + pyrite, to illite/smectite + chamosite, to chamosite + corrensite. Footwall breccias from site A are dominated by chamosite + corrensite alteration, with localized illite/smectite + chamosite alteration that varies in abundance over short distances and is interpreted to reflect proximity to inferred synvolcanic faults (Fig. 11A). Alteration at site B is semiconformable, varying downhole from illite/smectite + pyrite, to illite/smectite + chamosite, to chamosite + corrensite (Fig. 11B). Site C is characterized by nontronite near the surface, followed by nontronite + corrensite and chamosite + corrensite at depth (Fig. 12A). Alteration at site D varies from illite/smectite + pyrite near the surface, to illite/smectite + chamosite at depth (Fig. 12B). End-member illite and rectorite is present in all samples from site D, reflecting high temperatures (>220°C) and a progression from argillic to phyllic alteration at depth (e.g., Inoue et al., 1990). The variations in alteration assemblages identified at different sites along the NS-trending fissure appear to reflect variable thermal gradients and permeability structure.

Smectite is ubiquitous throughout the footwall in every alteration assemblage as discrete montmorillonite/nontronite replacing volcanic glass and/or mixed-layer clays. Mixed-layer illite/smectite clays range in composition from 50% illite to ~91% illite, with an average of 74% illite (n = 30) (App. Table

Table 2. Clay Minerals Identified by XRD from Samples of Altered Volcaniclastic Footwall from Tinakula Deposit, with Drill Holes Arranged According to Site from North to South (locations shown on Fig. 2)

Location Drill hole	Sample	Depth (m b.s.f.)	Munsell clay color	Smectite		Chlorite			Mixed-layer clays				Illite		Feldspar	Nonclay minerals								Alteration assemblage
				Mnt	Non	Cld	Clc	Cham	Corr	Alie(?)	Rect	I/S	Ill	Pg	Pl	Qz	Py	Mrc	Hem	Ata(?)	Anh	Brt	Cel	
Site A (North)																								
TKAD001	MA13-078	4.54–4.68	Moderate yellowish brown	++											++									Mnt/Non + Pl
	MA13-082	7.00–7.10	Light yellowish orange	++											++									Mnt/Non + Pl
	P002	10.39–10.50	Dusky yellow		++						(?)				+									Mnt/Non + Pl
	MA13-085	12.90–13.00	Dark yellowish orange		++										++									Mnt/Non + Pl
	MA13-086	14.00–14.12	Moderate reddish brown	(?)	++														Tr					Mnt/Non + Pl
	P003	14.81–14.95	Greenish gray		++	Tr			+															Non + Corr
	P004	15.65–15.80	Light greenish gray			Tr			++		++		Tr											Non + Corr
	MA13-087	16.05–16.22	Pale greenish yellow	(?)	++				Tr															Non + Corr
	MA13-088	17.40–17.50	Light greenish gray					++	++			++									Tr			I/S + Cham
	MA13-089	17.90–18.00	Light gray					++			++					Tr								I/S + Cham
	MA13-090	18.40–18.57	Light greenish gray					++			++	Tr	Tr	Tr										I/S + Cham
	P005	19.11–19.30	Very light gray					+			++	Tr	Tr	Tr			(?)							I/S + Cham
	MA13-091	20.77–21.00	Pale greenish yellow	Tr				+				++					(?)							I/S + Cham
	MA13-092	21.30–21.45	Light greenish gray					++	Tr			Tr		+										I/S + Cham
TKAD015	MA13-050	3.49–3.63	Pale olive	Tr				Tr				++		Tr						(?)				I/S + Cham
	MA13-051	4.34–4.43	Pale greenish yellow					++				+												Cham + Corr
	MA13-052	6.42–6.52	Grayish yellow green					++				Tr												Cham + Corr
	MA13-053	7.23–7.34	Grayish yellow green					++				Tr												Cham + Corr
TKAD027	MA13-056	2.50–2.60	Light olive					++			++									(?)		(?)	(?)	I/S + Cham
	MA13-057	4.60–4.70	Light greenish gray					++				Tr												I/S + Cham
	MA13-058	6.50–6.59	Grayish yellow green					++				+												I/S + Cham
TKAD028	MA13-099	4.50–4.60	Pale greenish yellow					++			(?)	+					Tr							I/S + Cham
TKAD029	MA13-095	3.60–3.70	Light yellowish orange		++										++									Non + Pl
Site B																								
TKAD016	MA13-034	2.02–2.13	Greenish gray							(?)	++							Tr						I/S + Py
	MA13-035	5.65–5.71	Pale greenish yellow					+			++	(?)												I/S + Cham
	MA13-036	7.00–7.05	Yellowish gray					++	(?)	+														Cham + Corr
TKAD025	MA13-039	5.50–5.60	Pale olive					++				Tr												I/S + Cham
	MA13-040	6.91–7.00	Pale olive	(?)				++	Tr															Cham + Corr
TKAD026	MA13-067	2.90–3.00	Light bluish gray					Tr			++						Tr							I/S + Cham
	MA13-068	3.60–3.68	Light greenish gray	Tr				++			(?)	++												I/S + Cham
	MA13-069	5.64–5.75	Light greenish gray					++			(?)	+												I/S + Cham
TKAD012	MA13-062	2.81–2.90	Pale olive					Tr	++															Cham + Corr
	MA13-063	4.25–4.36	Light greenish yellow				Tr		++					Tr										Cham + Corr
	MA13-064	6.49–6.60	Greenish gray						++			(?)							Tr					Cham + Corr
Site C																								
TKAD032	MA13-072	2.05–2.17	Yellowish gray		++																Tr			Mnt/Non + Pl
	MA13-073	3.90–4.00	Greenish gray		++				Tr										Tr		Tr			Non + Corr
	MA13-074	5.31–5.40	Grayish yellow		++				Tr												Tr			Non + Corr
	MA13-075	6.42–6.54	Greenish gray		++				Tr								Tr				(?)			Non + Corr

Table 2. *(Cont.)*

Location Drill hole	Sample	Depth (m b.s.f.)	Munsell clay color	Smectite		Chlorite			Mixed-layer clays				Illite		Feldspar	Nonclay minerals								Alteration assemblage
				Mnt	Non	Cld	Clc	Cham	Corr	Alie(?)	Rect	I/S	Ill	Pg	Pl	Qz	Py	Mrc	Hem	Ata(?)	Anh	Brt	Cel	
Site C *(Cont.)*																								
TKAD033	MA13-025	3.00–3.10	Dusky yellow		++										++		Tr				(?)			Mnt/Non + Pl
	MA13-026	4.76–4.88	Moderate brown		++		(?)								++				Tr					Mnt/Non + Pl
	MA13-027	7.30–7.40	Moderate brown				Tr		++						Tr				(?)					Cham + Corr
Site D																								
TKAD017	MA13-020	6.90–7.00	Yellowish gray	Tr							Tr	++	+				+				+			I/S + Py
TKAD030	MA13-005	5.06–5.21	Grayish yellow		++						+		Tr				Tr				Tr			I/S + Py
	MA13-006	6.45–6.60	Yellowish gray								++	+	Tr						+		+			I/S + Py
TKAD018	MA13-014	3.00–3.10	Light grayish yellow	+								++	Tr				Tr				Tr			I/S + Py
	MA13-015	5.00–5.10	Yellowish gray	Tr							Tr	++	Tr						Tr		Tr			I/S + Py
	MA13-016	6.60–6.71	Light grayish yellow	+				Tr				++	+						Tr		Tr			I/S + Cham
TKAD031	MA13-044	5.64–5.69	Grayish Yellow	Tr								++	Tr				(?)				Tr			I/S + Py
	MA13-045	6.60–6.67	Grayish Yellow	Tr								++	Tr				(?)				Tr			I/S + Py
Site E (South)																								
TKAD005	P020	20.55–20.67	Moderate greenish gray	(?)				++			++	(?)												I/S + Cham
TKAD003	P012	11.11–11.20	Light greenish gray	(?)				++				+												I/S + Cham
	P013	13.40–13.50	Bluish white					++				++												I/S + Cham
	P014	16.41–16.50	Bluish white					++				+												I/S + Cham
Site F (West)																								
TKAD007	P021	3.50–3.60	Light olive gray						++			(?)					Tr							I/S + Py
	P022	11.23–11.34	Bluish white					++			(?)	Tr												I/S + Cham
	P023	22.35–22.45	Pale greenish yellow					++				Tr	(?)											I/S + Cham
TKAD008	P025	7.50–7.56	Moderate reddish brown	Tr				+	++										(?)					Cham + Corr
	P024	18.13–18.20	Moderate reddish brown		++														(?)					Mnt/Non + Pl

Amounts indicated are major (++), minor (+), and trace (Tr); uncertain identifications are indicated by (?)

Mineral abbreviations: Alie = aliettite, Anh = anhydrite, Ata = paratacamite(?), Brt = barite, Cel = celestine, Cham = chamosite, Clc = clinochlore, Cld = chloritoid, Corr = corrensite, Hem = hematite, Ill = illite, I/S = illite/smectite, Mnt = montmorillonite, Mrc = marcasite, Non = nontronite, Pg = paragonite, Ph = phillipsite, Pl = plagioclase, Py = pyrite, Qz = quartz, Rect = rectorite

A3). The proportion of illite increases progressively downhole, indicating a process of continuous transformation of smectite to illite (e.g., Inoue et al., 1990). Chlorite may form directly from smectite or through an intermediate corrensite step (e.g., Shau et al., 1990). At Tinakula, chamosite appears before corrensite in the downhole progression of alteration assemblages, suggesting that corrensite is not an intermediate phase. Corrensite appears after illite/smectite, following a transition from illite/smectite + chamosite to chamosite + corrensite. This suggests that corrensite forms as an alteration product of the mixed-layer illite/smectite clays.

Alteration minerals were also characterized by SWIR spectroscopy (Table 3; App. Fig. A24). The white micas are identified by the distinct Al-OH absorption feature between 2,180 and 2,228 nm, with wavelengths of 2,189 to 2,195 nm for paragonite and 2,200 to 2,213 nm for muscovite and illite (this study; Thompson et al., 1999). In addition, small absorption features are present at 2,350 and 2,450 nm for the white micas. Montmorillonite is distinguished by a narrow and symmetrical 2,200-nm feature with a small shoulder on the H_2O + OH absorption feature at 1,450 to 1,460 nm. Chlorite is identified by the strong absorption feature at 2,340 nm, the wavelength of which increases from 2,324 nm for Mg-rich compositions to >2,350 nm for Fe-rich compositions. Gypsum is identified by the OH + H_2O feature at 1,400 nm, together with the OH feature at 1,800 nm. The alteration mineral assemblages observed in the SWIR analysis progress downhole from smectite (montmorillonite/nontronite), to white mica (paragonite

Table 3. Clay Minerals Identified by SWIR Spectroscopy from Samples of Altered Volcaniclastic Footwall from Tinakula Deposit, with Drill Holes Arranged from North to South (see Fig. 2)

Location		Depth	Smectite		Chlorite	White mica				Sulfate	AlO(OH)
Drill hole	Sample	(m b.s.f.)	Mnt (%)	Non (%)	Chl (%)	Pg (%)	Pgl (%)	Msl (%)	Ms (%)	Gp (%)	Dsp (%)
Site A (North)											
TKAD001	MA13-086-C	14.00–14.12	+++							+	
	MA13-087-C	16.05–16.22	+++				++				
	MA13-088-C	17.40–17.50						(?)	+++		
	P005-C	19.11–19.30	(?)					+++			
	MA13-091-CM	20.77–21.00			++				++		
TKAD015	MA13-052-C	6.42–6.52			(?)	+++				+	
	MA13-053-C	7.23–7.34			(?)	+++				++	
TKAD028	MA13-099-C	4.50–4.60								++	+++*
Site B											
TKAD016	MA13-034-C	2.02–2.13								++	+++*
	MA13-036-C	7.00–7.05	(?)		+++	++					
TKAD025	MA13-039-C	5.50–5.60	(?)		(?)					+++	
	MA13-040-C	6.91–7.00			+++					+	
TKAD026	MA13-067-C	2.90–3.00	++			+++					
	MA13-068-C	3.60–3.68	(?)		(?)	+++					
	MA13-069-C	5.64–5.75				(?)*				(?)*	
TKAD012	MA13-062-C	2.81–2.90	++		(?)		++				
Site C											
TKAD032	MA13-072-C	2.05–2.17	+++								
	MA13-073-C	3.90–4.00	+++								
	MA13-074-C	5.31–5.40	+++		(?)		++				
	MA13-075-C	6.42–6.54	+++		(?)		++				
TKAD033	MA13-026-C	4.76–4.88	+++								
	MA13-026-M	4.76–4.88	+++								
	MA13-027-C	7.30–7.40	+++								
	MA13-027-M	7.30–7.40									+++*
Site D											
TKAD030	MA13-005-C	5.06–5.21	(?)			+++					
	MA13-006-C	6.45–6.60	(?)			+++					
TKAD018	MA13-015-C	5.00–5.10				++				+++	
TKAD031	MA13-044-C	5.64–5.69		++			+++				
Site E (South)											
TKAD003	P013-C	13.40–13.50	++		(?)		+++				
	P014-C	16.41–16.50	(?)		++			++			
Site F (West)											
TKAD007	P022-C	11.23–11.34	(?)		++		+++				

Amounts indicated are >50% (+++), 25–50% (++), <25% (+); * = unreliable results

(?) indicates manual search of the spectral library; all others by Spectral Assist automated identification using TSG 7 software

Abbreviations: C = clast separate, Chl = chlorite, CM = clast + matrix, Dsp = diaspore, Gp = gypsum, M = matrix separate, Mnt = montmorillonite, Ms = muscovite, Msl = muscovitic illite, Pg = paragonite, Pgl = paragonitic illite

→ paragonitic illite → muscovitic illite → illite), to chlorite (e.g., App. Fig. A25), consistent with the XRD results. However, SWIR analyses with both montmorillonite and white mica reflect the presence of mixed-layer illite/smectite clays rather than discrete end members, with progressive increases downhole in aluminum content that shift the Al-OH absorption feature to lower wavelengths (e.g., Velde, 1980).

Alteration Geochemistry

Least altered volcanic rocks from the Tinakula deposit range from basaltic andesite and andesite to dacite, with basaltic andesite most abundant within and near the volcanic cones. Representative whole-rock geochemical analyses of altered volcaniclastic rocks from drill core are given in Table 4, with the associated alteration assemblages indicated. The least altered host rocks, described by Anderson (2018), were identified petrographically by a lack of alteration minerals, loss on ignition (LOI) <1.2 wt %, low base metal values (<183 ppm Cu + Zn + Pb), and no obvious Na_2O depletion (>4.0 wt %). Data for the three least altered basaltic andesite samples lie on linear trends, with those for the altered samples in plots of TiO_2 versus Zr and TiO_2 versus Al_2O_3 (Fig. 13). Excursions from this linear trend (e.g., Zr >160 ppm at ~1.5 wt % TiO_2; Fig. 13A) may reflect variability in the parental rock compositions, as volcanic rocks in this area show progressive fractionation from basaltic andesite to andesite (e.g., Anderson, 2018). The concentration ranges of immobile and mobile elements for each alteration assemblage are shown in Figure 14. The narrow range of concentrations of Zr, Y, Sc, Nb, Ti, and Al reflect the fact that these elements are least mobile. Concentrations of Ba, Si, Al, Fe, S, Mg, Ca, Na, and K show significant variation, consistent with their inferred mobility during hydrothermal alteration. High Ba, Ca, and $S_{(T)}$ reflect the abundance of barite and anhydrite/gypsum in the samples. High $Fe_2O_{3(T)}$ and $S_{(T)}$ are related to pyrite occurrence. Illite-smectite alteration is characterized by relative enrichments in K_2O compared to the least altered basaltic andesite, whereas chamosite + corrensite alteration is dominated by MgO addition. The bulk compositions are transitional between illite/smectite + pyrite to illite/smectite + chamosite to chamosite + corrensite end members (Fig. 15).

The chondrite-normalized REE profiles for the altered volcaniclastic rocks and the least altered basaltic andesite samples (Fig. 16) show pronounced positive Eu anomalies, as Eu becomes concentrated in hydrothermal fluids after it is released from plagioclase during water-rock interactions. Smectite-rich assemblages (nontronite/montmorillonite and nontronite + corrensite) show slight REE depletion and have flat profiles. The illite/smectite + pyrite assemblage displays significant light REE (LREE) enrichment and steeper profiles, whereas the chamosite-rich assemblages (illite/smectite + chamosite and chamosite + corrensite) show moderate LREE enrichment and flat profiles. The change in slope of the LREEs during the main stage of alteration (illite/smectite + pyrite) relative to the least altered rock indicates strong mobility. In contrast, the heavy REEs (HREEs) have slopes similar to those of the least altered rocks, which indicates that they are immobile during hydrothermal alteration. The HREEs are simply moved up or down relative to the least altered values due to the total mass gain or loss of the rock during alteration.

Major element mass changes were calculated for all alteration assemblages following the single precursor method of MacLean and Barrett (Maclean, 1990; Maclean and Barrett, 1993; Barrett and MacLean, 1999) using the average concentration of the three least altered samples as the precursor. In this method, the ratio of the concentration of an immobile element in an altered rock to the concentration of that element in the least altered precursor is proportional to the total mass change in the rock due to hydrothermal alteration. We used the proportion of the least mobile element, Zr, in the precursor sample relative to the altered sample to calculate

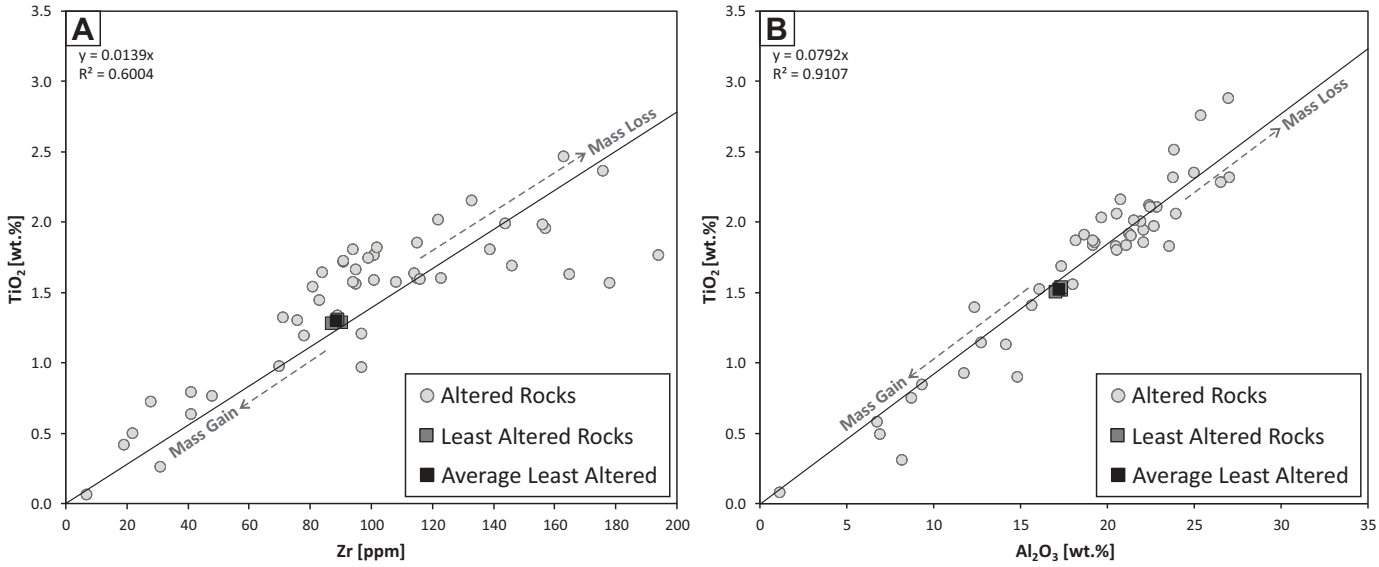

Fig. 13. Immobile element ratios of altered volcanic rocks and least altered precursor (average of three samples, from Anderson, 2018) showing linear trends of relative mass gains and losses, with increasing alteration intensity reflected by increasing distance from average least altered precursor composition: (A) Zr versus TiO_2 and (B) Al_2O_3 versus TiO_2.

Table 4. Whole-Rock Geochemical Analyses of Select Altered Volcaniclastic Rocks from Tinakula Deposit with Associated Alteration Assemblages, Normalized to 100% LOI-Free, and of Average Least Altered Basaltic-Andesite Composition (average of three samples: GMA13-057, P0016, and P0040; Anderson, 2018)

Element	Detection limit	Method	MA13-086-C TKAD001 Mnt/Non	MA13-073-C TKAD032 Non + Corr	MA13-006-C TKAD030 I/S + Py	MA13-088-C TKAD001 I/S + Cham	MA13-036-C TKAD016 Cham + Corr	Average least altered $n = 3$ B-A
SiO_2 (%)	0.01	FUS-ICP	47.03	51.72	41.65	52.34	35.27	54.39
TiO_2	0.001	FUS-ICP	1.586	1.718	2.467	1.983	1.804	1.30
Al_2O_3	0.01	FUS-ICP	19.28	21.93	27.00	23.80	22.85	17.27
$Fe_2O_{3(T)}$	0.01	FUS-ICP	11.89	13.69	20.24	8.99	23.18	9.98
MnO	0.001	FUS-ICP	0.078	0.045	0.010	0.253	0.079	0.189
MgO	0.01	FUS-ICP	13.38	7.65	0.63	6.42	9.11	3.57
CaO	0.01	FUS-ICP	4.20	0.65	0.69	1.16	3.43	8.50
Na_2O	0.01	FUS-ICP	1.58	2.34	1.50	1.05	1.33	4.09
K_2O	0.01	FUS-ICP	0.85	0.24	5.72	3.94	2.85	0.55
P_2O_5	0.01	FUS-ICP	0.14	0.04	0.07	0.06	0.11	0.14
$S_{(T)}$	0.01	CS	1.34	7.00	13.30	2.73	12.70	0.01
Cu (ppm)	1	TD-ICP[1]	11	237	128	141	2,250	73
Zn	1	TD-ICP[1]	625	1,080	135	928	120	98
Ag	0.3	TD-ICP	<0.3	3.1	1.3	0.6	0.6	<0.3
As	0.5	INAA	8.8	56.3	226.0	24.5	28.4	1.75
Bi	0.1	FUS-MS	<0.1	<0.1	<0.1	<0.1	<0.1	<0.1
Cd	0.5	TD-ICP	<0.5	1.4	<0.5	2.1	<0.5	<0.5
Ga	1	FUS-MS	17	17	28	23	22	17
Ge	0.5	FUS-MS	1.7	0.9	<0.5	1.0	<0.5	1.3
Au (ppb)	2	INAA	<2	42	94	82	51	<2
Hg	5	1G	5	902	14	298	0.6	9
In (ppm)	0.1	FUS-MS	<0.1	0.3	0.3	0.3	<0.2	0.1
Sb	0.2	INAA	11.3	10.4	3.4	1.3	<3	0.5
Se	3	INAA	<3	<3	<3	<3	<3	<3
Sn	1	FUS-MS	<1	<1	<1	1	1	7
Tl	0.05	FUS-MS	<0.05	1.14	0.40	0.76	0.34	0.07
Ir	5	INAA	<5	<5	<5	<5	<5	<5
Mo	2	FUS-MS	<2	12	8	<2	7	<2
Co	1	FUS-MS	9	27	11	17	17	23
Cr	5	INAA	<5	26	<5	13	<5	7
Ni	1	TD-ICP	5	24	5	7	6	8
Sc	0.1	INAA	21.6	24.8	32.6	28.8	21.2	24.8
V	5	FUS-ICP	90	316	350	360	283	351
Ba	2	FUS-ICP	130	7,194	2,228	1,559	395	108
Pb	3	TD-ICP	67	522	40	30	<3	<3
Rb	1	FUS-MS	14	4	64	56	28	6
Cs	0.1	FUS-MS	0.9	0.2	0.3	0.3	0.2	0.2
Sr	2	FUS-ICP	354	202	234	88	58	278
Zr	1	FUS-ICP	101	91	163	156	139	89
Hf	0.1	FUS-MS	2.4	2.1	3.6	3.9	3.3	2.0
Nb	0.2	FUS-MS	4.6	3.8	6.6	6.7	5.8	2.9
Ta	0.01	FUS-MS	0.22	0.18	0.43	0.36	0.22	0.18
Th	0.05	FUS-MS	0.84	0.67	1.25	1.35	1.03	0.68
U	0.01	FUS-MS	6.29	13.20	16.6	12.90	8.15	0.38
Be	1	FUS-ICP	2	2	<1	1	<1	<1
W	0.5	FUS-MS	1.0	0.6	178.0	2.8	124.0	0.6
Y	0.5	FUS-MS	27.8	20.8	38.4	33.3	37.1	29.2
La	0.05	FUS-MS	6.16	4.98	75.50	14.90	15.20	6.89
Ce	0.05	FUS-MS	14.90	12.10	157.00	31.90	33.90	16.10
Pr	0.01	FUS-MS	2.19	1.76	18.80	4.37	4.45	2.42
Nd	0.05	FUS-MS	11.00	8.86	74.00	19.20	20.10	11.0
Sm	0.01	FUS-MS	3.04	2.89	13.60	4.89	5.23	3.32
Eu	0.005	FUS-MS	1.32	1.41	7.58	2.53	2.67	1.27
Gd	0.01	FUS-MS	3.90	3.25	8.24	5.58	5.90	4.15
Tb	0.01	FUS-MS	0.69	0.6	1.13	0.95	1.01	0.73
Dy	0.01	FUS-MS	4.71	3.91	7.48	6.12	6.61	4.80
Ho	0.01	FUS-MS	1.04	0.77	1.45	1.31	1.37	1.00
Er	0.01	FUS-MS	2.98	2.25	4.50	3.77	4.11	2.85
Tm	0.005	FUS-MS	0.468	0.333	0.656	0.545	0.608	0.427
Yb	0.01	FUS-MS	3.10	2.27	4.39	3.39	4.12	3.72
Lu	0.002	FUS-MS	0.485	0.365	0.726	0.521	0.655	0.596

Method abbreviations refer to laboratory methods used by ActLabs: 1G = aqua regia Hg cold vapor flow injection technique, CS = total sulfur by IR, FUS = fusion, TD = total digestion; ICP = inductively coupled plasma, INAA = instrumental neutron activation analysis, MS = mass spectrometry

Mineral abbreviations: B-A = basaltic-andesite, Cham = chamosite, Corr = corrensite, I/S = illite/smectite, Mnt = montmorillonite, Non = nontronite, Pl = plagiolcase, Py = pyrite

[1]In the original data, several analyses of Cu and Zn that were over limits were reanalyzed with a different method; averages shown here include both the TD-ICP and 4 acid ICP-OES data

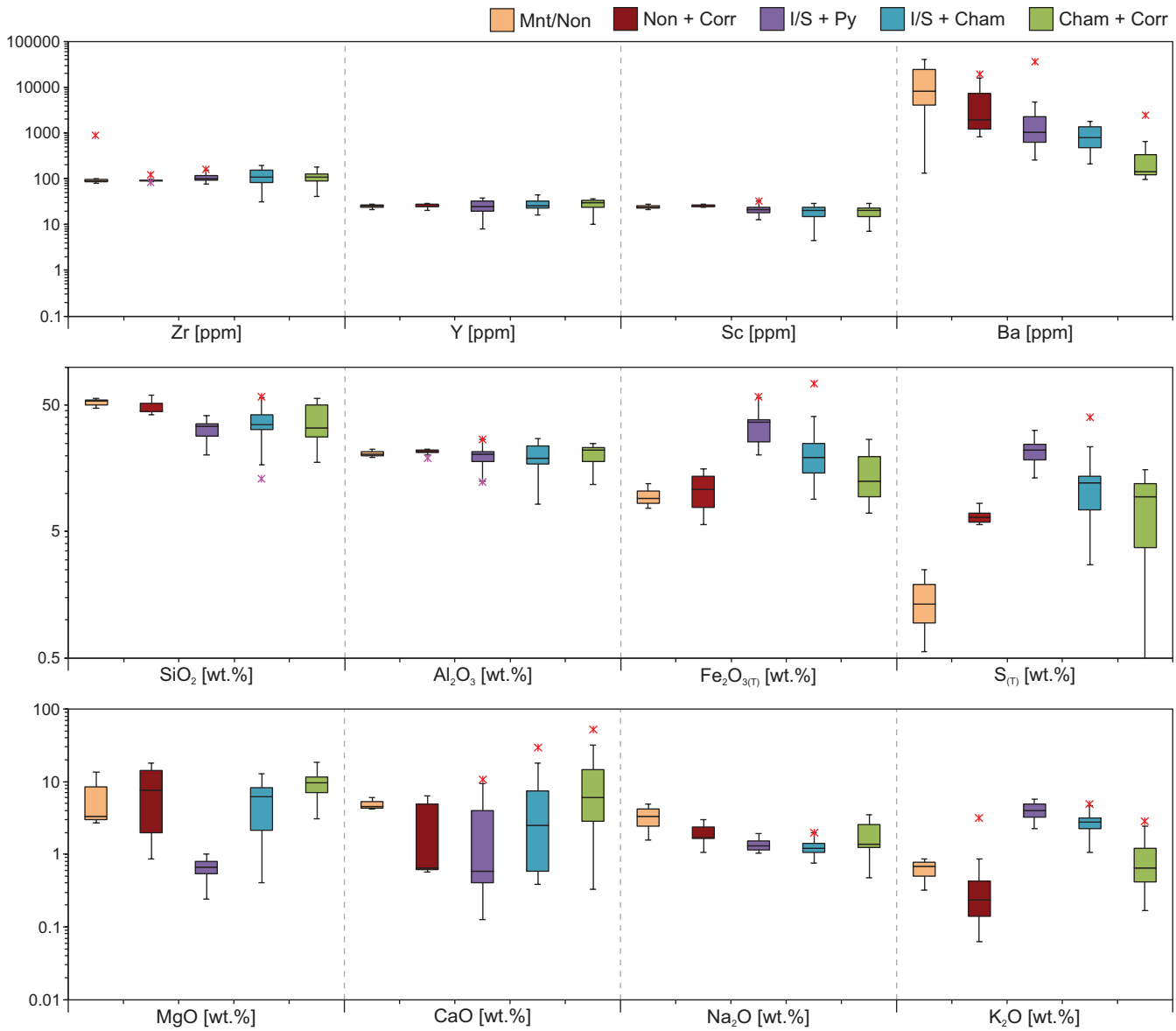

Fig. 14. Box plots of selected whole-rock immobile and mobile elements associated with each alteration assemblage (full data in Anderson, 2018). Top of each box represents the 75th percentile, bottom is the 25th percentile, central line represents median, bars show range of data, and outliers are indicated by stars (*). Abbreviation: Mnt = montmorillonite; others as in Figure 11.

the enrichment factor (EF). The reconstructed composition (RC) of the altered sample was calculated for each element by multiplying its concentration in the altered sample (normalized to 100% volatile free) by the EF. Finally, the mass change for each element in the sample was calculated by subtracting the precursor concentration of that element in the least altered sample from the RC. The largest mass changes are associated with moderate to intense alteration, generally increasing with depth (App. Figs. A26, A27). Mass changes for each assemblage are outlined below (Fig. 17; Table 5):

1. Montmorillonite/nontronite alteration is associated with Si and Na losses in smectite-rich samples, Ca loss in all samples, no gains in Al or Fe (either conserved or lost), and no change in K.
2. Nontronite + corrensite alteration is associated with Si, Ca, and Na losses, Mg gains, no losses of Al or Fe (either conserved or gained), and no change in K.
3. Illite/smectite + pyrite alteration is associated with losses in Si, Mg, Na, and Ca and gains in both Fe (due to pyrite) and K.
4. Illite/smectite + chamosite alteration is associated with Si and Na losses, K gains, and variable gains and losses in Fe and Mg (Mg losses where illite/smectite is more abundant than chamosite; Fe losses where illite/smectite and chamosite are equally abundant).
5. Chamosite + corrensite alteration is associated with Si and Na losses, Mg gains, Fe gains when chamosite is more abundant than corrensite and Fe losses when corrensite is more abundant, K gains when minor illite/smectite is

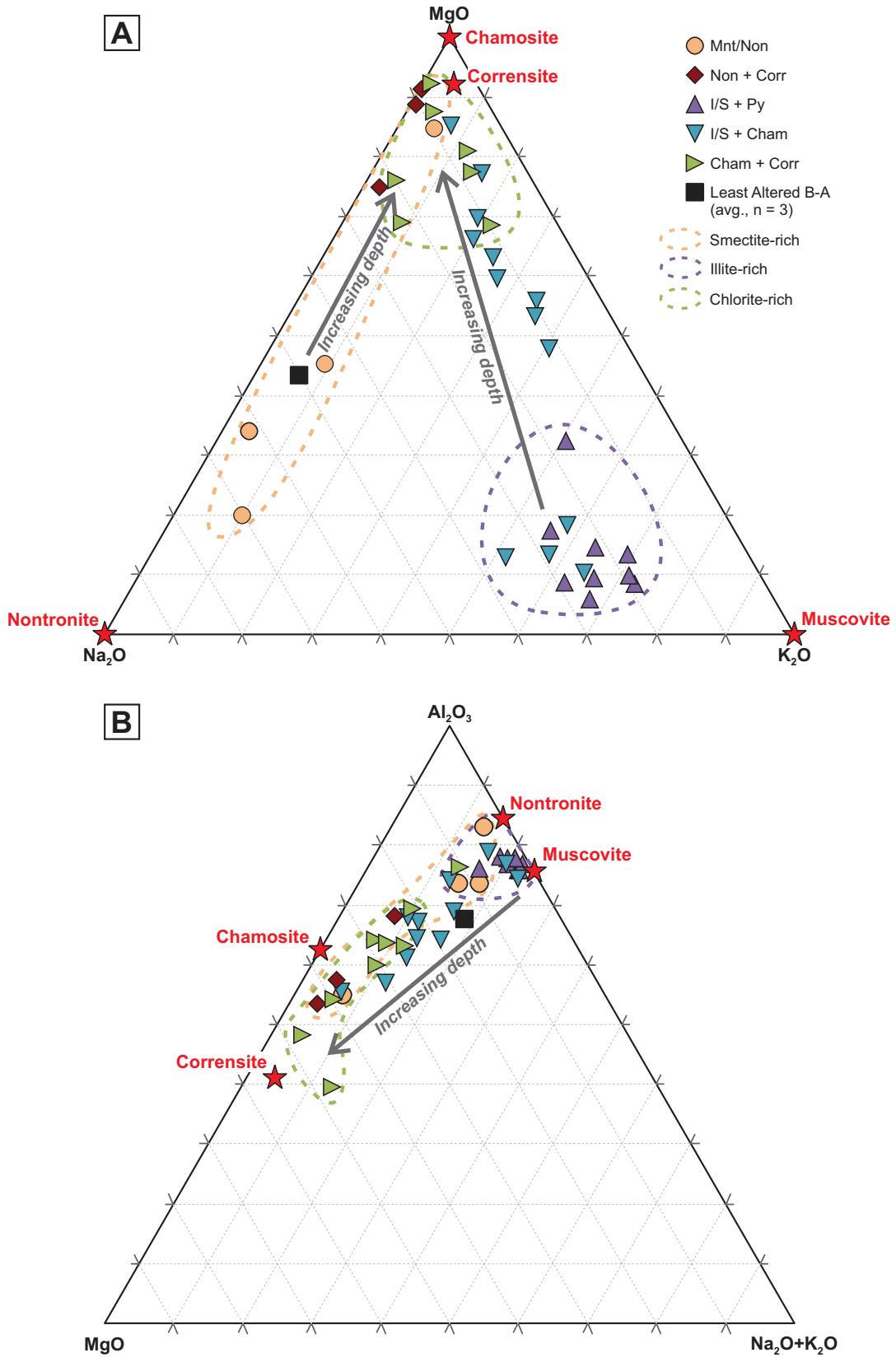

Fig. 15. Ternary plots of whole-rock geochemistry distinguishing alteration types. (A) MgO-Na_2O-K_2O distinguishing chlorite + smectite from illite alteration. (B) Al_2O_3-MgO-Na_2O+K_2O distinguishing chlorite from illite alteration (modified from MacDonald et al., 1996). General trends associated with increasing depth are shown. Abbreviations: B-A = basaltic andesite, Mnt = montmorillonite; others as in Figure 11.

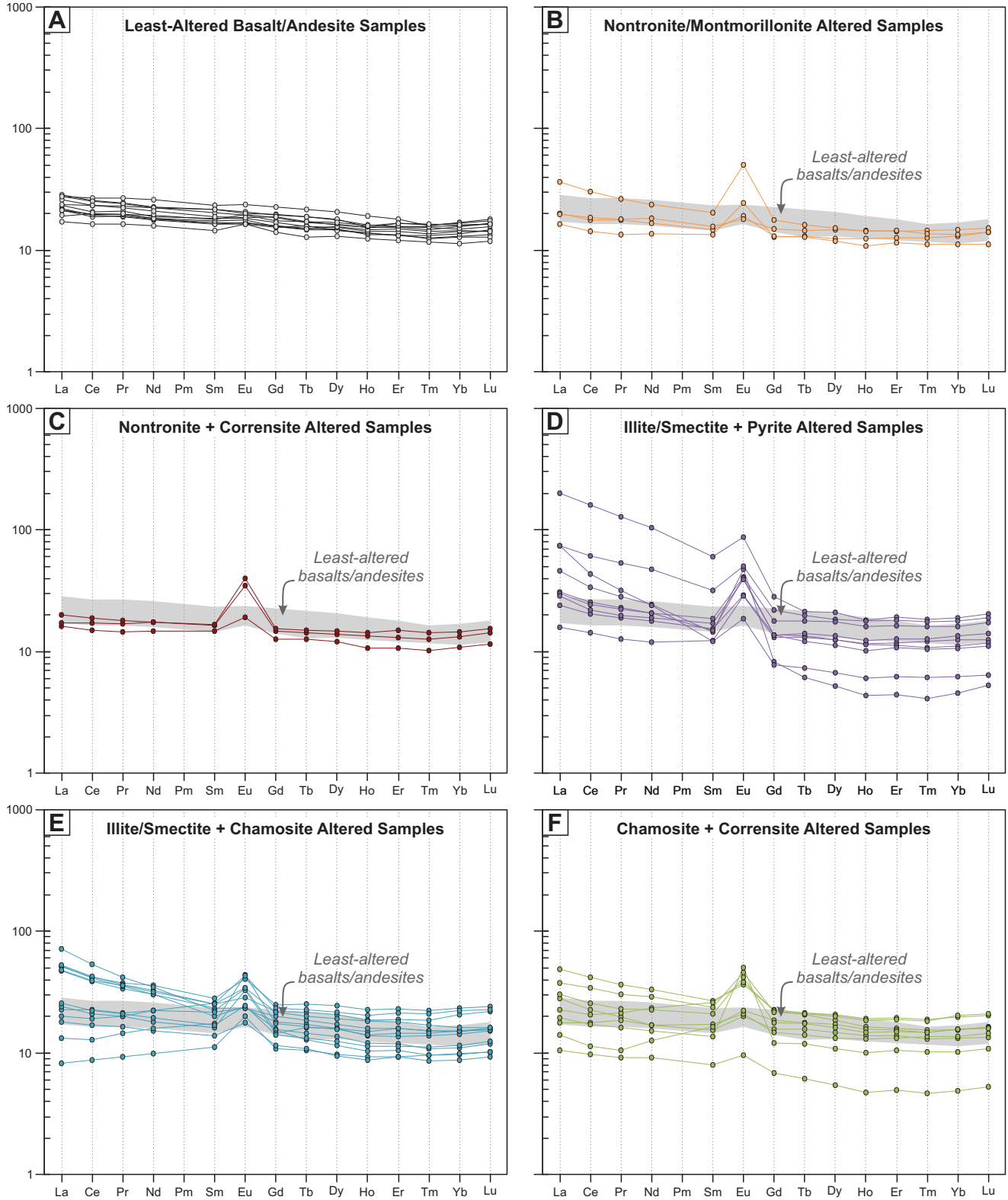

Fig. 16. Chondrite-normalized REE plots of different alteration assemblages compared to least altered basalts/andesites (Anderson, 2018). (A) Least altered basalt/andesite samples. (B) Nontronite/montmorillonite-altered samples with REE depletion and flat profiles. (C) Nontronite + corrensite-altered samples with REE depletion and flat profiles. (D) Illite/smectite + pyrite-altered samples with LREE enrichment in some samples and downward-sloping REE profiles. (E) Illite/smectite + chamosite-altered samples with moderate LREE enrichment in some samples and flat to downward-sloping profiles. (F) Chamosite + corrensite-altered samples with slight LREE enrichment in most samples and slightly downward sloping profiles. All alteration types are associated with pronounced positive Eu anomalies. Chondrite data from Boynton (1984).

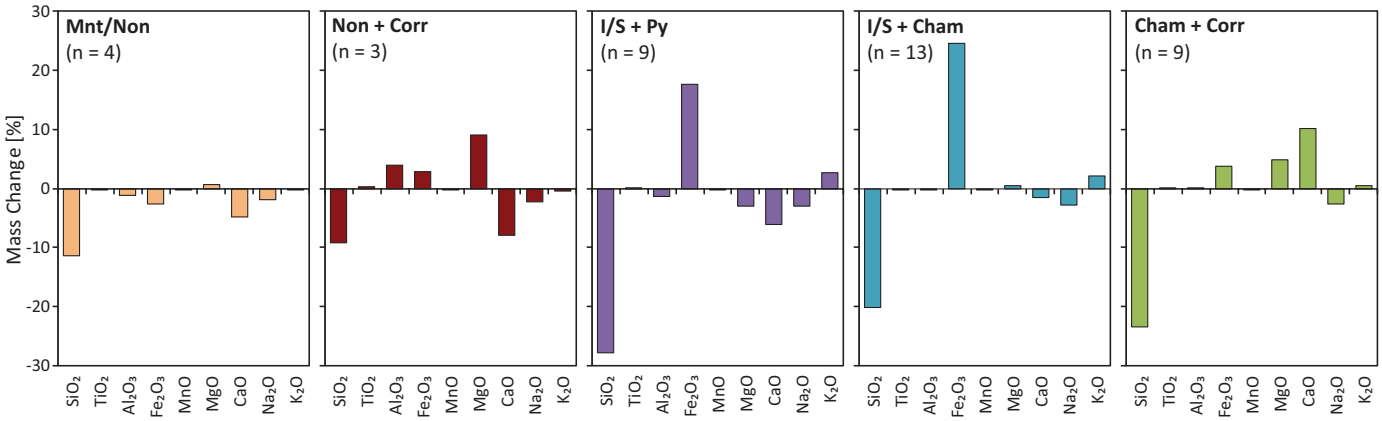

Fig. 17. Average mass changes for each alteration mineral assemblage. Abbreviation: Mnt = montmorillonite; others as in Figure 11.

Table 5. Mass Changes Associated with Alteration Mineral Assemblages in Altered Volcaniclastic Rocks Relative to at Least Altered Basaltic Andesite Precursor

Alteration	Sample	SiO_2	TiO_2	Al_2O_3	Fe_2O_3	MnO	MgO	CaO	Na_2O	K_2O	Comment
Mnt/Non ± Pl											
	MA13-086-C	L	0	0	0	0	G	L	L	0	Non-rich
	MA13-025-C	G	0	0	0	0	0	L	0	0	Pl-rich
	MA13-026-C	L	0	L	L	0	L	L	L	0	Non = Pl
	MA13-072-C	G	0	L	L	0	L	L	L	0	Non-rich
Non + Corr											
	MA13-073-C	L	0	G	G	0	G	L	L	0	Corr > Non
	MA13-074-C	L	0	G	G	0	G	L	L	0	Corr > Non
	MA13-075-C	L	0	0	0	0	G	L	L	0	Corr > Non
I/S + Py											
	MA13-087-C	L	0	L	L	0	L	L	L	G	Minor Corr
	MA13-034-C	L	0	0	G	0	L	G	L	G	Rect
	MA13-019-CM	L	0	G	G	0	G	L	L	G	
	MA13-020-CM	L	0	G	G	0	L	L	L	G	I/S, Mnt, Rect
	MA13-044-C	L	0	L	G	0	L	L	L	G	I/S
	MA14-045-C	L	0	G	G	0	L	L	L	G	I/S, Mnt, Pl?
	MA13-005-M	L	0	L	G	0	L	L	L	G	Non, Rect
	MA13-006-C	L	0	L	G	0	L	L	L	G	Rect, I/S
	MA13-014-C	L	0	L	G	0	L	L	L	G	Mont, I/S
	MA13-015-C	L	0	L	G	0	L	L	L	G	I/S, Mont, Rect
I/S + Cham											
	MA13-088-C	L	0	L	L	0	0	L	L	G	I/S = Cham
	MA13-090-C	L	0	L	G	0	0	L	L	G	Cham > I/S
	MA13-091-CM	G	0	0	G	0	0	L	L	G	Cham > I/S
	MA13-050-C	G	0	G	G	0	L	L	L	G	I/S > Cham
	MA13-056-CM	L	0	G	G	0	L	L	L	G	I/S > Cham
	MA13-057-C	L	0	G	G	0	G	G	L	G	Cham > I/S
	MA13-058-C	L	0	0	G	0	G	L	L	G	Cham > I/S
	MA13-035-C	L	0	L	L	0	0	L	L	G	Rect = Cham
	MA13-039-C	L	0	L	G	0	G	G	L	G	Cham > I/S
	MA13-067-C	L	0	G	G	0	L	L	L	G	I/S > Cham
	MA13-068-C	L	0	L	L	0	G	L	L	G	I/S = Cham
	MA13-069-C	L	0	L	L	0	G	L	L	G	I/S = Cham
	MA13-016-C	L	0	G	G	0	L	G	L	G	I/S > Cham
Cham + Corr											
	MA13-051-CM	L	0	L	G	0	G	L	L	G	Minor I/S
	MA13-052-C	L	0	G	G	0	G	G	L	G	Minor I/S
	MA13-053-C	L	0	G	G	0	G	G	L	G	Minor I/S
	MA13-036-C	L	0	L	G	0	G	L	L	G	Minor I/S(?)
	MA13-040-C	L	0	L	G	0	G	L	L	0	Cham > Corr
	MA13-062-C	L	0	L	L	0	G	L	L	0	Corr > Cham
	MA13-063-C	L	0	L	L	0	G	L	L	0	Corr > Cham
	MA13-064-C	L	0	G	G	0	G	G	L	0	Cham > Corr
	MA13-027-CM	L	0	G	L	0	0	L	L	0	Corr > Cham

Notes: G = gain, L = loss, 0 = no change

Mineral abbreviations: Cham = chamosite, Corr = corrensite, I/S = illite/smectite, Mnt = montmorillonite, Non = nontronite, Pl = plagioclase, Py = pyrite, Rect = rectorite

present, and no changes in K where no illite/smectite is present.

Mass dilution effects caused by anhydrite and pyrite precipitation were partially mitigated through handpicking of individual altered clasts, avoiding veins and cement/infill. Despite this procedure, not all of these materials could be omitted, thus contributing CaO, Fe_2O_3, and S and accounting for some apparent loss of SiO_2. The main difference between the low-temperature alteration stage (dominated by illite/smectite + pyrite) and the higher-temperature alteration stage (dominated by chamosite + corrensite) is the mass change of MgO (higher in chamosite) and K_2O (higher in illite/smectite), typical of VMS-style alteration in permeable volcaniclastic rocks (e.g., Shikazono et al., 1995; Franklin et al., 2005).

Conditions of Alteration and Mineralization

The high permeability of the volcanic substrate at Tinakula has had a large impact on the composition, size, and morphology of the seafloor mineralization and subseafloor alteration. The conditions of alteration and mineralization have been constrained in this study by fluid inclusion microthermometry, stable isotope data, and dating of the hydrothermal barite.

Fluid inclusion microthermometry

Fluid inclusions were investigated in five samples of hydrothermally altered volcaniclastic rocks recovered in drill hole TKAD001 between 14.8 and 19.3 m b.s.f. Details of the petrography and microthermometry are provided in Appendix Table A4. Fluid inclusions occur in three distinct paragenetic stages: early anhydrite in veins and rimming altered volcanic clasts, sphalerite at the margins of the early anhydrite veins in the deepest samples (MA13-090 and P005), and later infills of anhydrite and barite.

Primary and secondary inclusions in large (up to 1.4 mm), tabular anhydrite crystals are generally 10 to 20 μm, reaching maximum diameters of 60 μm (Fig. 18A). All inclusions

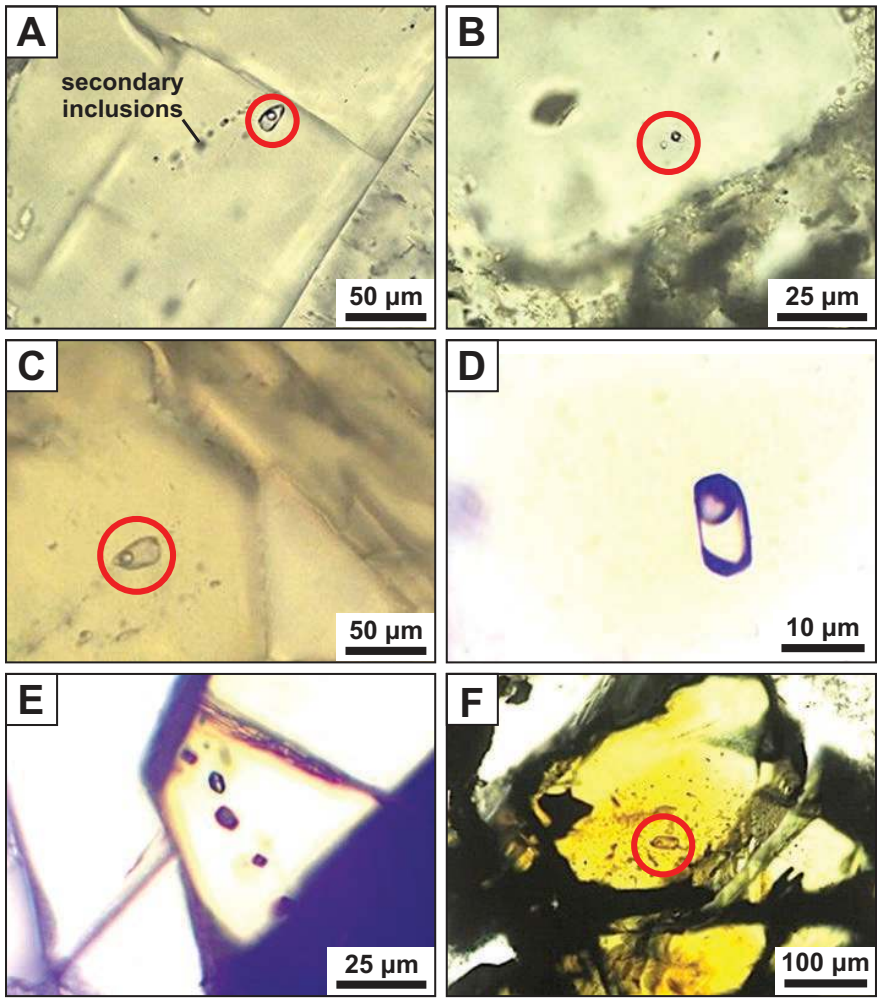

Fig. 18. Transmitted-light in plane-polarized light (TL-PPL) photomicrographs of fluid inclusions from samples from drill hole TKAD001. (A) Single primary fluid inclusion (red circle) in tabular anhydrite next to secondary inclusions formed as a result of crack healing (sample P004_E_g03). (B) Two primary fluid inclusions in anhydrite with a vapor phase (red circle; sample P003_A_g01). (C) A large primary inclusion in barite (red circle; sample P004_R_g01). (D) Large primary inclusion within sphalerite (sample P005_P_g03). (E) Row of secondary fluid inclusions in sphalerite with negative crystal shapes (sample MA13-090_I_g01). (F) Sphalerite crystal containing numerous secondary fluid inclusions, including large one within red circle (sample P005_G_g01). Fluid inclusion groups are outlined in Appendix Table A4.

are liquid dominated with 1 to 10 vol % vapor (Fig. 18B). Large crystals of barite (up to 1 mm), after anhydrite, contain mostly secondary inclusions, between 4 and 40 μm in size and with a maximum of 10 vol % vapor (Fig. 18C). The inclusions in sphalerite (after anhydrite) include both primary liquid-vapor inclusions up to 50 μm in diameter with 5 to 30 vol % vapor (Fig. 18E) and groups of smaller secondary inclusions (<10 μm) distributed along healed cracks (Fig. 18F). Two inclusions in sphalerite contained a dark solid phase (3–5 vol %) with a tabular habit, likely a sulfide mineral.

Estimated trapping temperatures of primary fluid inclusions in anhydrite reach 295°C with salinities close to that of seawater (2.8–3.8 wt % NaCl equiv). Inclusions in barite have slightly lower trapping temperatures (median 218°C) with a bimodal distribution from 202° to 220°C and 256° to 266°C (Fig. 19A) and salinities from 2.8 to 3.4 wt % NaCl equiv (Fig. 19B). However, it is known that barite can stretch during heating (e.g., Ulrich and Bodnar, 1988), so these homogenization temperatures may be biased toward higher values. Trapping temperatures of primary fluid inclusions in sphalerite are up to 298°C (Fig. 19C) with salinities of 2.6 to 4.5 wt % NaCl equiv (Fig. 19D).

The highest inclusion trapping temperatures are only ~10° to 20°C lower than the minimum temperature of boiling for Tinakula fluids (308°–311°C at 1,070–1,204 m water depth; Fig. 20), and the highest salinities clearly exceed that of seawater. Although coexisting vapor-rich and brine fluid inclusions associated with boiling were not encountered in the investigated minerals, elevated salinities in several inclusions likely reflect mixing between a brine (derived from boiling) and seawater. This strongly suggests that the highest-temperature fluids have boiled at depth and cooled by mixing on ascent to the seafloor. Cooling of deep fluids from a higher temperature at depth (e.g., 350°C for typical end-member hydrothermal fluids) would have resulted in the deposition of most of the Cu-rich sulfides below the seafloor, which could account for the predominance of Zn-rich sulfide in the chimneys (e.g., Hannington et al., 2005).

Oxygen and hydrogen isotopes in clay minerals

Clean separates of monomineralic nontronite (n = 2), chamosite (n = 9), corrensite (n = 2), and rectorite (n = 1) were analyzed for oxygen and hydrogen isotopes, spanning sample depths of 2.8 to 22.5 m b.s.f. (Table 6; Fig. 19E, F). Values of $\delta^{18}O_{V\text{-}SMOW}$ range from 12.3 to 12.5‰ for nontronite, 2.2 to 8.3‰ for chamosite, 9.6 to 11.1‰ for corrensite, and 5.9‰ for one sample of rectorite. The large range and high $\delta^{18}O$ values reflect substantial shifts relative to those of hydrothermally modified seawater (e.g., Huston, 1999). Temperatures were calculated following Savin and Lee (1988) assuming $\delta^{18}O$ of the hydrothermal fluid is close to that of typical mid-ocean ridge hydrothermal vent fluids ($\delta^{18}O$ = 1.3‰; Shanks et al., 1995; Jean-Baptiste et al., 1997). The calculated temperatures range from 124° to 251°C, with an error of ±10% (Fig. 19F), showing a systematic increase from nontronite (136°–138°C), to chamosite (124°–205°C), corrensite (207°–227°C), and rectorite (256°C), with the highest temperatures close to trapping temperatures of fluid inclusions in the anhydrite and sphalerite. The $\delta^{18}O$ value of the hydrothermal fluid in equilibrium with the analyzed

Table 6. Oxygen and Hydrogen Isotope Measurements and Calculated Temperatures of Formation of Clay Minerals from Footwall of Tinakula Deposit and Initial Oxygen and Hydrogen Isotope Values for Hydrothermal Fluid Calculated at 240°C

Site	Drill hole	Sample	Depth (m b.s.f.)	Mineral	δD_{rock} (‰ V-SMOW)	$\delta^{18}O_{rock}$ (‰ V-SMOW)	Fractionation factors			Temperature (°C)	$\delta^{18}O_{water, initial}$ (‰ V-SMOW)	$\delta D_{water, initial}$ (‰ V-SMOW)
							A	B	Reference			
A	TKAD001	MA13_087	16.1–16.2	Nontronite	–86	12.5	2.55	4.05	1	136	6.9	
A	TKAD027	MA13_057	4.6–4.7	Chamosite	–53	4.9	3.10	12.63	3	164	4.8	–11.3
A	TKAD015	MA13_053	7.2–7.3	Chamosite	–53	4.1	3.10	12.63	3	175	5.0	–10.5
B	TKAD025	MA13_039	5.5–5.6	Chamosite	–65	8.3	3.10	12.63	3	124	9.2	–23.1
B	TKAD025	MA13_040	6.9–7.0	Chamosite	–52	2.2	3.10	12.63	3	205	3.1	–9.8
B	TKAD026	MA13_067	2.9–3	Rectorite	–69	5.9	2.458	4.19	2	256	0.8	
B	TKAD026	MA13_069	5.6–5.8	Chamosite	–61	5.1	3.10	12.63	3	161	6.0	–18.7
B	TKAD012	MA13_062	2.8–2.9	Corrensite	–85	9.6	4.28	8.78	3	227	2.1	
B	TKAD012	MA13_063	4.3–4.4	Corrensite	–80	11.1	4.28	8.78	3	207	3.6	
C	TKAD032	MA13_075	6.4–6.5	Nontronite	–92	12.3	2.55	4.05	1	138	6.7	
E	TKAD003	PO012	11.1–11.2	Chamosite	–56	4.6	3.10	12.63	3	169	5.4	–14.1
E	TKAD003	PO014	16.4–16.5	Chamosite	–57	4.0	3.10	12.63	3	177	4.9	–15.1
F	TKAD007	PO022	11.2–11.3	Chamosite	–54	5.8	3.10	12.63	3	152	6.7	–11.7
F	TKAD007	PO023	22.4–22.5	Chamosite	–53	3.3	3.10	12.63	3	187	4.2	–10.6

Fractionation factors after (1) Sheppard and Gilg (1996), (2) Savin and Lee (1988), and (3) Buatier et al. (1995); initial $\delta^{18}O_{water}$ and δD_{water} calculated for equilibrium temperature of 240°C; hydrogen fractionation factor for chlorite-water (α = 0.954) after Marumo et al. (1980)

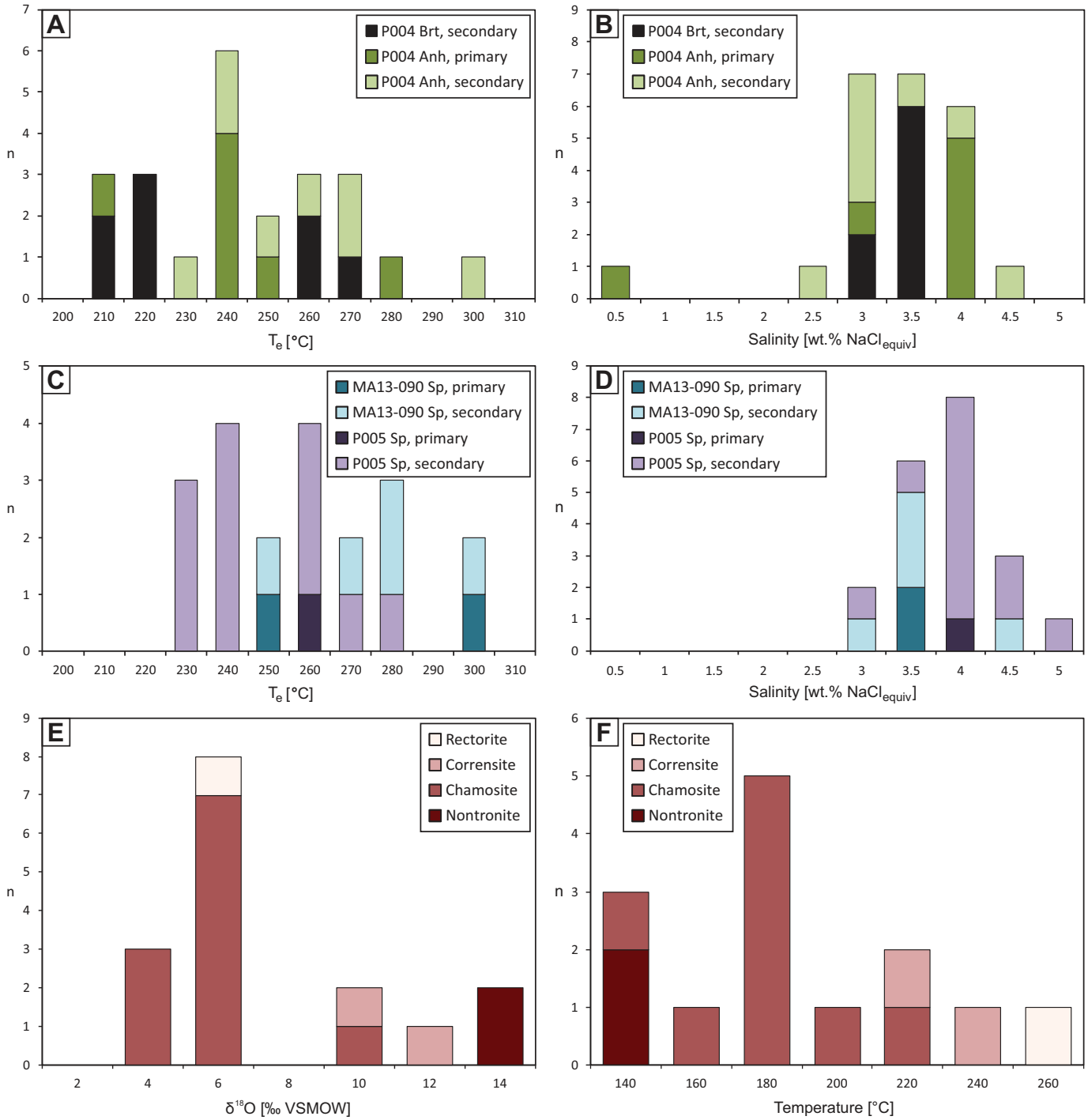

Fig. 19. Homogenization temperatures and salinities of fluid inclusions (A-D) from TKAD001 and oxygen isotopes and calculated temperatures (E, F) in clay alteration assemblages. (A) Entrapment temperatures (T_e) of inclusions in barite and anhydrite from sample P004 (15.7 m b.s.f.). (B) Salinities of inclusions in barite and anhydrite from sample P004 (15.7 m b.s.f.). (C) Entrapment temperatures (T_e) of inclusions in sphalerite from samples MA13-090 (18.5 m b.s.f.) and P005 (19.3 m b.s.f.). (D) Salinities of inclusions in sphalerite from samples MA13-090 (18.5 m b.s.f.) and P005 (19.3 m b.s.f.). (E) Frequency distribution histograms for $\delta^{18}O$ values in clay mineral assemblages. (F) Calculated temperatures from oxygen isotopes for the different clay mineral phases. Abbreviations: Anh = anhydrite, Brt = barite, Sp = sphalerite.

clay minerals could have been closer to 5.0‰, if we assume a temperature of formation of 240°C (Table 6), following Sheppard and Gilg (1996). The large range of calculated $\delta^{18}O_{H_2O}$ values at the inferred temperatures of alteration is consistent with boiling of the hydrothermal fluids (e.g., Huston, 1999; see Fig. 21).

Values of $\delta D_{V\text{-}SMOW}$ range from –92 to –86‰ for nontronite, –65 to –52‰ for chamosite, –85 to –80‰ for corrensite,

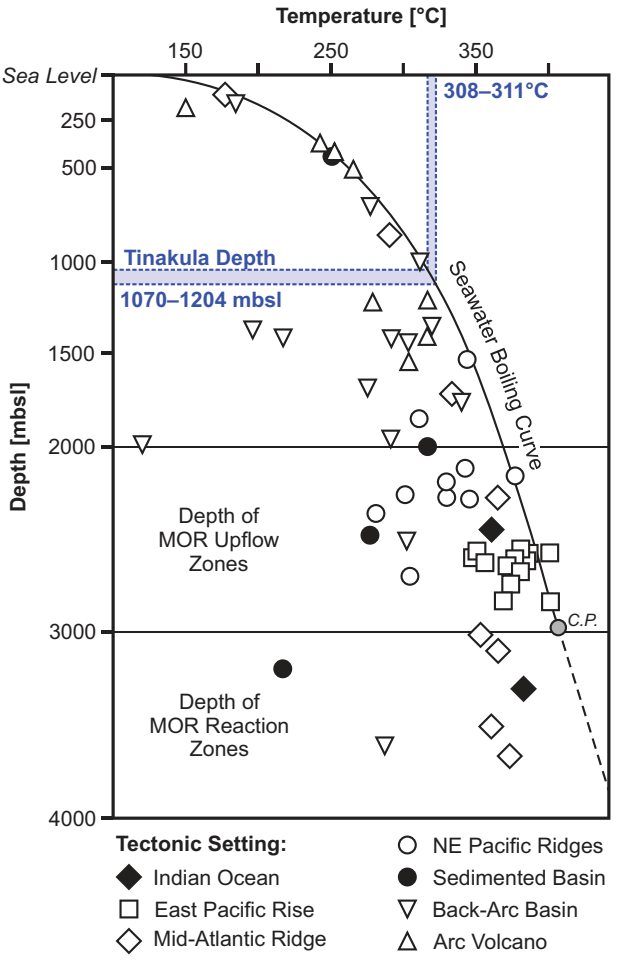

Fig. 20. Seawater boiling curve showing maximum temperatures of submarine hydrothermal vents, with examples from different tectonic settings (Hannington et al., 2005) with data from Stoffers et al. (2006). Depth range of Tinakula deposit (gray) corresponds to maximum temperature range of 308° to 311°C. Depths of mid-ocean ridge (MOR) upflow and reaction zones are approximate; C.P. = critical point of seawater.

and –69‰ in the single sample of rectorite. There is a general increase in $\delta D_{V\text{-}SMOW}$ with depth, consistent with the downhole increase in calculated temperature. Importantly, no accepted hydrogen isotope fractionation factors exist for 2:1 phyllosilicate minerals in order to calculate initial δD_{water} values. Gilg and Sheppard (1996) proposed approximating the fractionation factors of Al-rich and Fe- and Mg-free smectites using kaolinite factors; however, the smectites in this study are Fe-rich nontronite. Initial δD_{water} values in equilibrium with chamosite, using a chlorite-water fractionation factor of α = 0.954 from Marumo et al. (1980), are –18.7 to –9.8‰ (Table 6). However, hydrogen isotope fractionation in chlorite is strongly dependent on mineral chemistry (e.g., Marumo et al., 1980; Savin and Lee, 1988), thus adding uncertainty to the initial δD_{water} values.

High $\delta^{18}O_{water}$ values have been reported for Kuroko-type hydrothermal fluids (up to 10.8‰; Ohmoto, 1983, 1996). The shifts in $\delta^{18}O_{water}$ to lower values at higher temperatures (e.g., minimum of 0.8‰ in equilibrium with rectorite during chalcopyrite deposition) are typical of the stringer zones of ancient VMS deposits (e.g., Cathles, 1993). The ^{18}O-rich fluids at Tinakula may be derived from isotopic exchange with ^{18}O-rich rocks, boiling, or direct contributions from magmatic fluids. At high temperatures, water-rock interactions can shift $\delta^{18}O_{water}$ but not δD_{water} (Huston, 1999). We interpret the combination of higher $\delta^{18}O_{water}$ and lower δD_{water} at Tinakula as a result of subseafloor boiling, which is likely because of the shallow water depths there and the fluid inclusion trapping temperatures, which are close to the boiling curve (Fig. 22). The lack of low-pH mineral assemblages and the seawater-dominated S isotope signature (see below) suggest that there was no magmatic contribution to the hydrothermal fluids or only a limited one.

Sulfur isotopes

The $\delta^{34}S$ values of chalcopyrite range from –0.8 to 2.0‰ and are, on average, slightly lower in the Cu-rich chimneys than in the Zn-rich chimneys (Fig. 23A). Pyrite has $\delta^{34}S$ values of –0.4 to 3.1‰ (Fig. 23B), and sphalerite has $\delta^{34}S$ of 0.3 to 3.4‰ (Fig. 23C), both minerals having higher values in Zn-rich chimneys. Fe-poor (light-colored) sphalerite has slightly higher $\delta^{34}S$ values than Fe-rich (dark-colored) sphalerite from the same sample. However, there is no systematic spatial variation in $\delta^{34}S$ of the sulfides along the main NS-trending fissure at Tinakula, suggesting that the sulfur source was uniform. Barite from chimney samples yielded $\delta^{34}S$ of 19.3 to 22.5‰ (Fig. 23D). Anhydrite from the altered volcaniclastic rocks has $\delta^{34}S$ of 20.6 to 22.2‰, whereas gypsum has $\delta^{34}S$ of 21.3 to 21.8‰ (Fig. 23D), all close to that of seawater sulfate ($\delta^{34}S$ = 21.24‰; Tostevin et al., 2014), with a slight decrease with depth (App. Table A5).

The isotopic composition of the sulfate minerals records predominantly seawater sulfate in pore spaces of the volcaniclastic rocks. Sulfide values are generally close to mid-ocean ridge basalt (MORB) values but lower than those of typical arc lavas (e.g., Alt et al., 1993; Labidi et al., 2012, 2014). This pattern may result from degassing of magmatic volatiles, which can produce H_2S with low $\delta^{34}S$ values from the disproportionation of SO_2 (Gamo et al., 1997; Kusakabe et al., 2000). However, there is no evidence at Tinakula of significant volatile contributions that elsewhere produce advanced argillic alteration and very light sulfide sulfur with negative $\delta^{34}S$ values and no evidence of bacterial sulfate reduction that would also produce negative $\delta^{34}S$ values (cf. Hannington et al., 2005).

Timing of alteration and mineralization

Results of $^{226}Ra/Ba$ dating of hydrothermal barite are shown in Table 7 and Figure 24. The calculated ages indicate that hydrothermal venting has been ongoing for at least 5,600 ± 240 years. Approximately 60% of the data yield ages between 792 and 2,369 years. Although there is no obvious spatial variation in the ages (App. Fig. A28), the two oldest samples (>4,000 yr, MA13-011 and MA13-030) were collected from drill core, whereas younger samples were collected primarily from chimneys. Drilling at site D intersected two discrete oxidized intervals that are interpreted as paleoseafloor horizons. The upper paleoseafloor horizon displays lateral continuity over ~20 m east-west and ~25 m north-south, but the lower horizon was not recovered in drill hole TKAD030 (App.

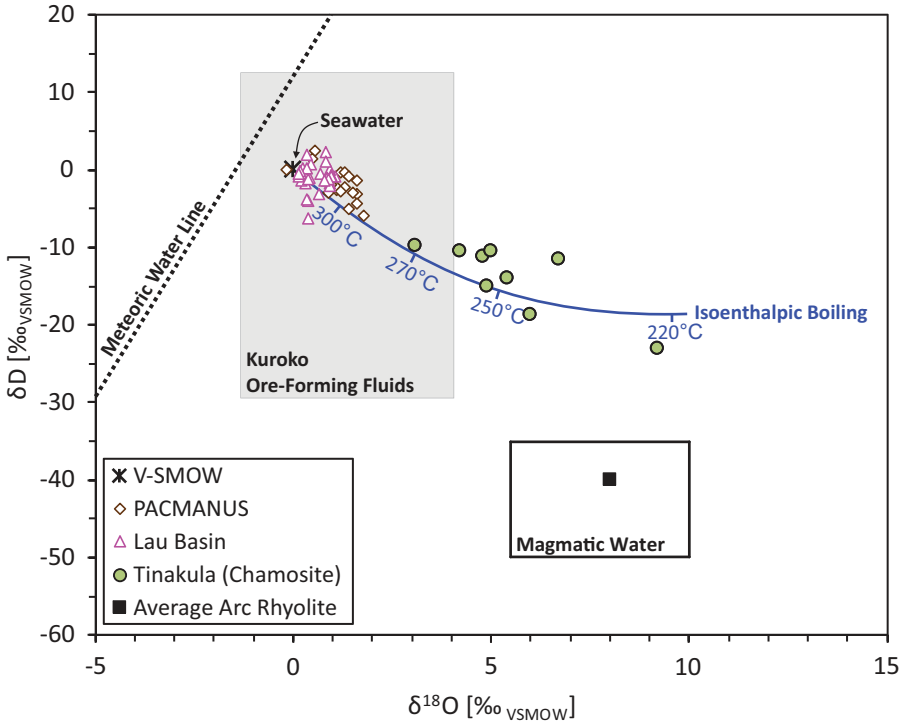

Fig. 21. $\delta^{18}O$-δD diagram showing isotopic values for the hydrothermal fluid at Tinakula equilibrated at a temperature of 240°C (see Table 6), compared to data from Lau basin (Mottl et al., 2011), PACMANUS deposit in Manus basin (Reeves et al., 2011), and Kuroko ore-forming fluids (Ohmoto, 1996). Fields for seawater and magmatic water (Sheppard, 1986; Taylor, 1992) and global meteoric water line (Craig, 1961) are also shown. Data from Tinakula closely follow adiabatic boiling path from Huston (1999), associated with increasing $\delta^{18}O$ values and slightly decreasing δD values with progressive boiling.

Fig. A15); instead, an intact, buried sphalerite-rich chimney was cored. This shows that different parts of the mound were actively venting at different times. The ages of the talus samples confirm that the paleoseafloor horizon on which the talus was deposited is at least 1,000 years old and gives a minimum age for the volcaniclastic cover sequence, which is variably altered and mineralized throughout the Tinakula deposit. Because of the low solubility (Blount, 1977) and high preservation potential of barite, even the oldest barite chimneys are well preserved. One fully intact (inactive) chimney has a calculated age of 3,450 ± 229 years (Table 7). Currently, the system appears to be in a waning phase of hydrothermal activity, with widespread late-stage precipitation of low-temperature amorphous silica and Fe and Mn oxyhydroxides.

Discussion and Conclusions

Drilling of the Tinakula deposits has revealed widespread hydrothermal alteration within ~10 m of the seafloor in the highly permeable volcaniclastic substrate. The alteration assemblages reported here are consistent with a near-neutral or slightly acidic pH (cf. Reyes, 1990; Corbett and Leach, 1998). Salinities of primary fluid inclusions (2.8–4.5 wt %

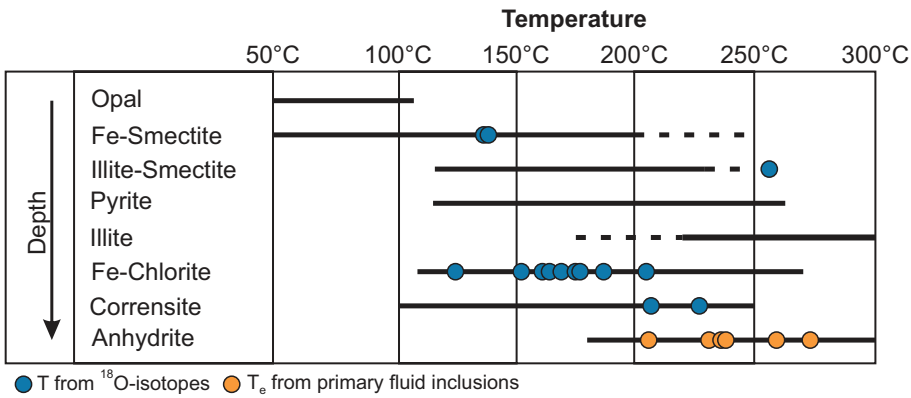

Fig. 22. Temperature ranges for the formation of hydrothermal alteration minerals from Reyes (1990), with significant overlap shown among minerals. Temperature calculations for the Tinakula deposit using ^{18}O isotopes (blue circles; Table 6) and primary fluid inclusions in anhydrite (orange circles; App. Table A4) are shown.

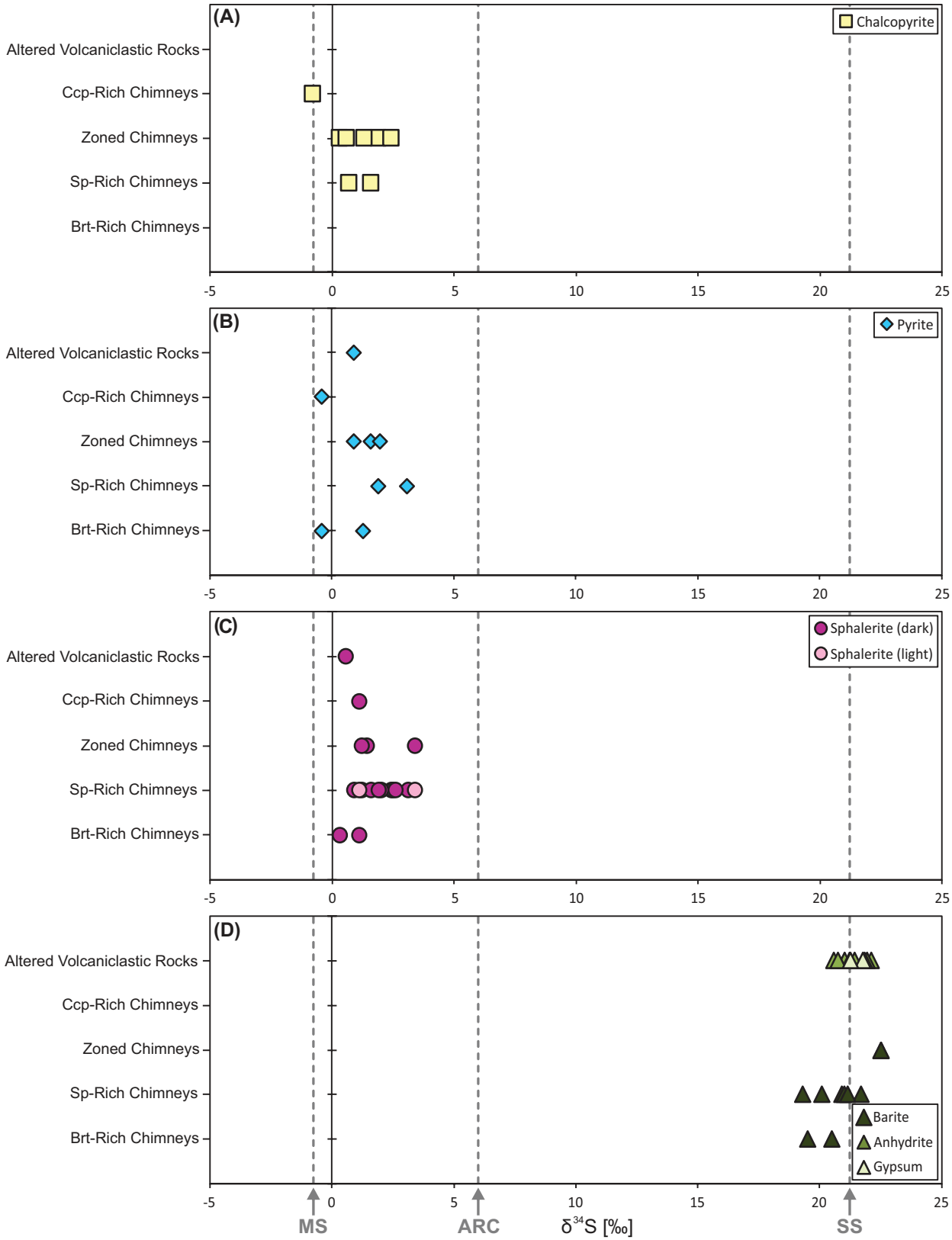

Fig. 23. Variations in $\delta^{34}S$ (V-CDT) values in minerals from chimneys at the Tinakula deposit: (A) chalcopyrite, (B) pyrite, (C) sphalerite (dark and light), and (D) anhydrite, gypsum, and barite. Rock types are shown on left. Composition of MORB sulfur (MS: $\delta^{34}S$ = –0.9 to –0.6‰; Labidi et al., 2012, 2014), island-arc andesite sulfur (ARC: $\delta^{34}S$ = 6.00‰; Alt et al., 1993), and seawater sulfate (SS: $\delta^{34}S$ = 21.24‰; Tostevin et al., 2014) are shown by dashed lines. Complete S isotope data are in Appendix Table A5. Abbreviations: Brt = barite, Ccp = chalcopyrite, Sp = sphalerite.

Table 7. Results of ^{226}Ra Dating of Hydrothermal Barite from the Tinakula Deposit

Site	Sample	Comment	Latitude (deg)	Longitude (deg)	Seafloor depth (m b.s.l.)	Drill hole depth (m b.s.f.)	Ba (wt %)	^{226}Ra Activity (Bq/kg)	^{226}Ra/Ba (Bq/kg×wt %)	Age (years)
ROV grab samples										
A	GMA13-040	Inactive chimney	–12.193892	167.614811	1,123.4	-	9.15	2,828 ± 162	309	2,760 ± 233
B	GMA13-019A	Talus	–12.195040	167.615151	1,100.6	-	7.34	3,102 ± 157	423	2,038 ± 224
B	GMA13-021	Inactive chimney	–12.195794	167.615009	1,087.5	-	0.04	24 ± 4	666	988 ± 390
B	GMA13-022	Talus	–12.195428	167.615430	1,090.3	-	14.10	5,162 ± 252	366	2,369 ± 222
B	GMA13-045	Talus	–12.195959	167.615924	1,089.7	-	13.50	5,153 ± 247	382	2,273 ± 221
C	GMA13-032	Inactive chimney	–12.197044	167.616683	1,074.3	-	0.46	188 ± 15	411	2,101 ± 265
C	GMA13-061	Talus	–12.196961	167.616188	1,081.6	-	8.48	3,319 ± 170	391	2,215 ± 225
D	GMA13-010	Active chimney	–12.197393	167.616495	1,074.5	-	2.72	2,593 ± 209	953	160 ± 267
D	GMA13-024	Active chimney	–12.197836	167.616620	1,094.1	-	3.65	3,729 ± 162	**1,022**	**0**
D	GMA13-029	Inactive	–12.198487	167.616818	1,109.7	-	16.90	9,187 ± 407	544	1,457 ± 217
D	GMA13-031	Talus	–12.196567	167.616119	1,103.3	-	9.04	5,322 ± 248	589	1,273 ± 220
D	GMA13-034	Active chimney	–12.198043	167.616941	1,108.3	-	1.85	1,333 ± 71	720	807 ± 227
D	GMA13-062	Talus	–12.197878	167.616395	1,099.7	-	6.36	1,728 ± 100	272	3,057 ± 234
E	GMA13-002	Inactive chimney	–12.198648	167.616513	1,109.4	-	14.50	3,323 ± 181	229	3,450 ± 229
Drill core samples										
B	MA13-028	Drill hole TKAD013	–12.196126	167.615524	1,090.8	0.6–0.7	0.07	-	-	-
B	MA13-029	Drill hole TKAD013	–12.196126	167.615524	1,090.8	2.2–2.3	4.07	2,950 ± 149	725	792 ± 224
B	MA13-030	Drill hole TKAD013	–12.196126	167.615524	1,090.8	3.6–3.7	9.42	1,337 ± 87	142	4,556 ± 244
B	MA13-031	Drill hole TKAD013	–12.196126	167.615524	1,090.8	4.9–5.0	0.64	420 ± 36	659	1,014 ± 274
B	MA13-065	Drill hole TKAD026	–12.196357	167.615549	1,089.0	0.5–0.7	8.19	3,691 ± 187	451	1,891 ± 224
D	MA13-011	Drill hole TKAD018	–12.198291	167.616920	1,110.2	1.1–1.2	12.80	1,158 ± 73	90	5,597 ± 240
D	P0043	Drill hole TKAD031	–12.198549	167.616643	1,110.3	2.9–3.0	1.21	963 ± 56	795	578 ± 234
E	P0010	Drill hole TKAD003	–12.201212	167.617034	1,113.8	1.0–1.1	0.97	583 ± 40	599	1,234 ± 248
E	P0011	Drill hole TKAD003	–12.201212	167.617034	1,113.8	5.8–5.9	0.78	699 ± 47	896	304 ± 247

Bold values indicate the initial ^{226}Ra/Ba ratio of the zero-age chimney; - = not applicable/not determined; sample MA13-028 contained insufficient Ba for analyses

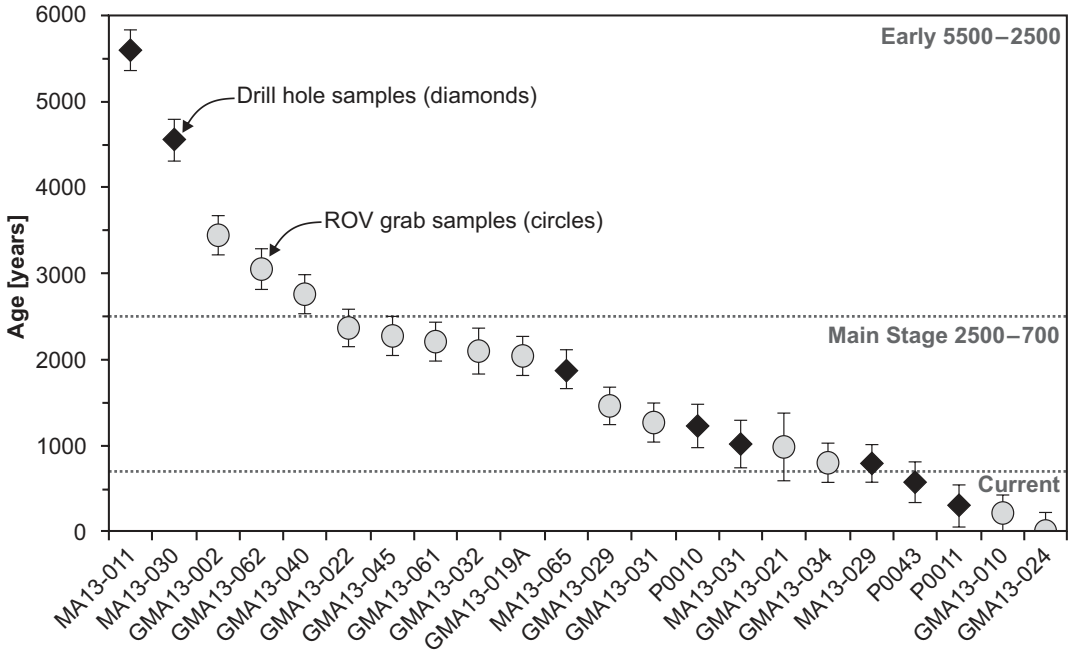

Fig. 24. Distribution of ^{226}Ra ages of hydrothermal barite from sulfide chimney material at the Tinakula massive sulfide deposit. Ages are relative to zero age of sample GMA13-024. Data are in Table 7.

NaCl equiv) and isotopic data on the sulfide, sulfate, and silicate minerals indicate seawater-dominated fluids, possibly with a component of condensed vapor-phase liquid, and abundant fluid mixing between hydrothermal fluids and ambient seawater. The calculated temperatures of clay formation range from 124° to 256°C, lower than the calculated trapping temperatures of primary fluid inclusions in anhydrite and sphalerite, suggesting that the late sulfate-sulfide veins were likely transporting hotter fluids. The highest-temperature fluids likely boiled at a depth just below the deepest drill holes. Several lines of evidence indicate increasing temperature with depth: (1) the transition from barite near the surface to anhydrite at depth, (2) the progressive transition from smectite to mixed-layer illite/smectite (with increasing proportions of illite) to corrensite to chamosite (e.g., Fig. 11A, B), and (3) decreasing $\delta^{18}O$ and increasing δD values of monomineralic clays. Calculated temperatures of formation increase by ~130°C from nontronite → chamosite → corrensite → rectorite. Downhole temperature gradients are as high as 80°C in just over 1 m (e.g., TKAD025 at site B). However, several drill holes show reverse temperature gradients. In particular, data for TKAD026 suggests decreasing temperatures from 256°C at 2.9 m b.s.f. to 161°C at 5.6 m b.s.f., reflecting the control of variable subseafloor permeability on lateral fluid flow and variable subsurface mixing with entrained seawater.

The alteration mineralogy at Tinakula is similar to proximal footwall alteration associated with Kuroko-type VMS deposits (e.g., Shirozu, 1974; Date et al., 1983; Shikazono et al., 1995). In these deposits, the shallow subseafloor strata surrounding the fossil upflow zones is dominated by low-temperature montmorillonite/nontronite, with higher-temperature illite/smectite + pyrite present in the immediate footwall of the massive sulfide and illite/smectite + chamosite and chamosite + corrensite at depth, similar to sites A, C, and D at Tinakula. Sites A and D are interpreted to be at the center of the highest-temperature upflow, where there is active venting, chalcopyrite-rich chimneys, and extensive formation of illite. The alteration mineralogy at sites B, C, E, and F reflects relatively lower temperatures, consistent with the dominant sphalerite- and barite-rich chimneys.

The alteration assemblages are all associated with Si loss (Fig. 17; Table 5), which may be partially related to dilution associated with anhydrite precipitation at depth, with net mass changes of as much as 49%. Similar loss of Si has been documented in association with phyllosilicate alteration at the PACMANUS hydrothermal system in the Manus back-arc basin (Giorgetti et al., 2006; Paulick and Bach, 2006; Monecke et al., 2007). In contrast, at Tinakula Si gains occur at the tops of drill holes TKAD015, TKAD032, and TKAD033 (App. Figs. A26, A27), representing local silicification near the seafloor in the form of opaline silica filling void spaces. Large gains in Ca near the bottom of drill holes TKAD015, TKAD012, and TKAD018 likely record the deposition of anhydrite at the higher subseafloor temperatures at depth, which could reflect incomplete removal of the anhydrite-rich matrix material during clast separations. Large mass gains in K_2O (and LREEs) in the illite/smectite + pyrite assemblages are similar to the observed mass changes in the feeder zones of VMS deposits hosted by felsic volcaniclastic rocks (e.g., Mattabi-type alteration; Morton and Franklin, 1987). Alteration in the immediate upflow zone at Tinakula might also be enhanced by the pyrite precipitation, which generates acid. In the surrounding permeable rocks, drawdown of seawater has added MgO. Intuitively, this process should be associated with cooling, but the higher temperatures of chlorite formation at depth in the Tinakula drill holes, based on $\delta^{18}O$ data (Fig. 22), may also have increased the drawdown, resulting in the observed Mg addition.

In permeable volcaniclastic rocks, an important question is how the permeability becomes sealed enough to allow focusing of the hydrothermal fluids to the seafloor. Here, we propose that the pervasive alteration of the volcaniclastic units close to the seafloor coincided with a progressive downward increase in subseafloor temperatures, from initial low temperatures during precipitation of nontronite (136°–138°C), increasing to chamosite (124°–205°C), corrensite (207°–227°C), and eventually rectorite (256°C). At 150°C, the temperatures were high enough to form anhydrite at depths of only a few meters below the seafloor, sealing off some permeability and focusing the fluids into channelized pathways to the seafloor. Continued hydrothermal circulation resulted in overpressuring and fracturing of this relatively impermeable layer, precipitating late sulfate veins with minor sulfide minerals (Fig. 3E), including sphalerite, at temperatures up to 298°C. A similar model has been proposed for the anhydrite-cemented breccias in the Pacmanus deposit in the Manus basin (Binns and Scott, 1993; Binns et al., 2007) and the Suiyo seamount and Iheya North Knoll field in the Izu-Bonin-Mariana arc (Ishibashi et al., 2013, 2015). This process has been investigated using numerical modeling (Kawada and Yoshida, 2010); in ancient deposits, anhydrite is rarely preserved because of its retrograde solubility; the only evidence remaining of an anhydrite seal would be the presence of alteration minerals formed at temperatures that would have caused anhydrite deposition. Chlorite-rich alteration pipes in otherwise permeable volcaniclastic sequences may have been shielded from infiltrating seawater by anhydrite that is no longer present in the rocks. Although rarely preserved in ancient VMS deposits, anhydrite and gypsum are locally abundant in the Kuroko ores (e.g., Shikazono et al., 1983) and may have played an important role in the focusing of hydrothermal upflow in those deposits, as at Tinakula.

Barite and silica, which form close to the seafloor at much lower temperatures than anhydrite, may also have been important in forming an initial cap on the permeable units, promoting lateral flow of fluids and allowing subseafloor temperatures to reach the point of anhydrite precipitation (>150°C; Bischoff and Seyfried, 1978). Early cooling of the fluids and mixing near the seafloor was likely, given the highly permeable volcaniclastic cover. The style of hydrothermal upflow also plays an important role in the nature of the seafloor mineralization. Jamieson et al. (2016) showed a high proportion of seawater mixing in chimneys with predominant dendritic barite; similar diffuse venting is likely responsible for the formation of porous beehive-like structures and unusual bulbous chimneys observed at Tinakula (cf. Koski et al., 1994). This style of venting, which has been inferred for the origin of layered barite-sulfide mounds in the East Diamante caldera (Hein et al., 2014) and at Clark seamount (de Ronde et al., 2014), may be common where seafloor venting occurs through permeable volcaniclastic substrates. Diffuse discharge over a large area is also consistent with the bottom-hugging plume signal originally detected at Tinakula (McConachy et al., 2002).

The Tinakula SMS deposit is the first documented example of a modern SMS deposit developed mainly in bimodal-mafic volcaniclastic rocks. The particular mineralization and alteration styles recognized here are a direct result of the volcanic setting, which is dominated by a permeable substrate rather than the coherent lava flows typical of mid-ocean ridges. Morphologies of the volcanic cones at Tinakula and the volcaniclastic facies successions are consistent with extensive Strombolian-type eruptions, forming a row of cinder cones along a NS-trending fissure. The eruptions likely occurred over days to months (cf. Sigurdsson, 2000), while geothermal activity at Tinakula may have lasted thousands of years. The massive sulfide mineralization may not be closely related temporally to formation of the cinder cones, but instead the hydrothermal systems most likely exploited the same structural corridor. Lateral fluid flow and semiconformable alteration at Tinakula are similar to those described in a class of ancient VMS deposits hosted by volcaniclastic rocks (e.g., Franklin et al., 2005; Galley et al., 2007), such as the Sturgeon Lake VMS district (e.g., Morton and Franklin, 1987; Morton et al., 1991; Hudak et al., 2004; Mueller et al., 2004; Holk et al., 2008). In ancient VMS deposits of this type, semiconformable alteration is commonly observed at depths of several hundred meters below the paleoseafloor, associated with subseafloor deposition of massive sulfide (e.g., Allen et al. 2002; Doyle and Allen, 2003). What is unusual at Tinakula is that hydrothermal fluids affected such a large area so close to the seafloor: ~150,000 m^2 at the seafloor and possibly three times as large below the seafloor. The shallow alteration and anhydrite likely acted as an insulating layer for hydrothermal circulation and mineralization at depth, as seen in ancient VMS deposits.

Acknowledgments

The authors gratefully acknowledge Neptune Minerals, Inc., for providing samples, data, and other in-kind contributions that made this study possible. In particular, K. Allen, J. Carpenter, and R. Sharpe are thanked for assistance with sample and data collection. We would also like to thank the following people from GEOMAR: N. Augustin, A. Jegen, and S. Lange for assistance in preparing and analyzing clays, M. Thörner for help with EPMA, and J. Heinze for assistance with XRD. Funding for this project was provided by a Natural Sciences and Engineering Research Council of Canada (NSERC) Alexander Graham Bell Canada Graduate Scholarship (Doctoral) (CGS-D) award to M. Anderson and an NSERC Discovery Grant to M. Hannington. This manuscript was greatly improved by reviews provided by J.F. Slack, R. Allen, G.J. Hudak, and S. Piercey. This is contribution MERC-ME-2019-168 to the modern-ancient crust project of the Canadian Metal Earth program.

REFERENCES

Allen, R.L., Weihed, P., and The Global VMS Research Project Team, 2002, Global comparisons of volcanic-associated massive sulfide deposits, *in* Blundell, D.J., Neubauer, F., and von Quadt, A., eds., The timing and location of major ore deposits in an evolving orogen: Geological Society of London, Special Publication 204, p. 13–38.

Alt, J.C., Shanks, W.C. III., and Jackson, M.C., 1993, Cycling of sulfur in subduction zones: The geochemistry of sulfur in the Mariana island arc and back-arc trough: Earth and Planetary Science Letters, v. 119, p. 477–494.

Anders, M., 2016, Fluid inclusions and mineralogy at the seafloor massive sulfide deposit, New Hebrides arc/backarc, Solomon Islands: Unpublished M.Sc. thesis, Kiel, Germany, Christian Albrechts University of Kiel, 96 p.

Anderson, M.O., 2018, Relationships between tectonics, volcanism, and hydrothermal venting in the New Hebrides and Mariana back-arc basins,

western Pacific: Unpublished Ph.D. thesis, Ottawa, Canada, University of Ottawa, 1030 p.
Anderson, M.O., Hannington, M.D., Haase, K.M., Schwarz-Schampera, U., Augustin, N., McConachy, T.F., and Allen, K., 2016, Tectonic focusing of voluminous basaltic eruptions in magma-deficient backarc rifts: Earth and Planetary Science Letters, v. 440, p. 43–55.
Auzende, J.-M., Pelletier, B., and Eissen, J.-P., 1995, The North Fiji basin: Geology, structure, and geodynamic evolution, *in* Taylor, B., ed., Backarc basins: Tectonics and magmatism: New York, Plenum Press, p. 139–175.
Barrett, T.J., and MacLean, W.H., 1999, Volcanic sequences, litho-geochemistry, and hydrothermal alteration in some bimodal volcanic-associated massive sulfide systems: Reviews in Economic Geology, v. 8, p. 101–131.
Barrie, C.T., and Hannington, M.D., 1999, Classification of volcanic-associated massive sulfide deposits based on host-rock composition: Reviews in Economic Geology, v. 8, p. 1–11.
Beaulieu, S.E., and Szafranski, K., 2018, InterRidge Global database of active submarine hydrothermal vent fields: Prepared for InterRidge, Version 3.4, http://vents-data.interridge.org.
Bergeot, N., Bouin, M.N., Diament, M., Pelletier, B., Régnier, M., Calmant, S., and Ballu, V., 2009, Horizontal and vertical interseismic velocity fields in the Vanuatu subduction zone from GPS measurements: Evidence for a central Vanuatu locked zone: Journal of Geophysical Research, v. 114, p. 1–20.
Biagioni, C., Dini, A., Orlandi, P., Moëlo, Y., Pasero, M., and Zaccarini, F., 2016, Lead-antimony sulfosalts from Tuscany (Italy). XX. Members of the jordanite-geocronite series from the Pollone mine, Valdicastello Carducci: Occurrence and crystal structures: Minerals, v. 6, p. 1–15.
Binns, R.A., and Scott, S.D., 1993, Actively forming polymetallic sulfide deposits associated with felsic volcanic rocks in the eastern Manus back-arc basin, Papua New Guinea: Economic Geology, v. 88, p. 2226–2236.
Binns, R.A., Barriga, F.J.A.S., and Miller, D.J., 2007, Leg 193 synthesis: Anatomy of an active felsic-hosted hydrothermal system, eastern Manus basin, Papua New Guinea, *in* Barriga, F.J.A.S., Binns, R.A., Miller, D.J., and Herzig, P.M., eds., Proceedings of the Ocean Drilling program, scientific results, v. 193: College Station, Texas, Ocean Drilling Program, p. 1–17.
Bischoff, J.L., and Seyfried, W.E. Jr., 1978, Hydrothermal chemistry of seawater from 25°C to 350°C: American Journal of Science, v. 278, p. 838–860.
Blount, C.W., 1977, Barite solubilities and thermodynamic quantities up to 300°C and 1400 bars: American Mineralogist, v. 62, p. 942–957.
Bodnar, R., and Vityk, M., 1994, Interpretation of microthermometric data for H_2O-NaCl fluid inclusions, *in* De Vivo, B., and Frezzotti, M., eds., Fluid inclusions in minerals: Methods and applications: Blacksburg, Virginia, Virginia Polytechnic and State University, p. 117–130.
Boynton, W.V., 1984, Cosmochemistry of the rare earth elements: Meteorite studies, *in* Henderson, P., ed., Rare earth element geochemistry: Amsterdam, Elsevier, p. 63–114.
Brown, P.E., 1989, FLINCOR: A computer program for the reduction of and investigation of fluid inclusion data: American Mineralogist, v. 74, p. 1390–1393.
Buatier, M.D., Früh-Green, G.L., and Karpoff, A.M., 1995, Mechanism of Mg-phyllosilicate formation in a hydrothermal system at a sedimented ridge (Middle Valley, Juan de Fuca): Contributions to Mineralogy and Petrology, v. 122, p. 134–151.
Canfield, D.E., Raiswell, R., Westrich, J.T., Reaves, C.M., and Berner, R.A., 1986, The use of chromium reduction in the analysis of reduced inorganic sulfur in sediments and shales: Chemical Geology, v. 54, p. 149–155.
Cashman, K.V., 2004, Volatile controls on magma ascent and eruption, *in* Sparkes, R.S.J., and Hawkesworth, C.J., eds., The state of the planet: Frontiers and challenges in geophysics: Washington, D.C., American Geophysical Union, p. 109–124.
Cathles, L.M., 1993, Oxygen isotope alteration in the Noranda mining district, Abitibi greenstone belt, Quebec: Economic Geology, v. 88, p. 1483–1511.
Clayton, R.N., and Mayeda T.K., 1963, The use of bromine pentafluoride in the extraction of oxygen from oxides and silicates for isotopic analysis: Geochimica et Cosmochimica Acta, v. 27, p. 43–52.
Cook, N., Ciobanu, C.L., Pring, A., Skinner, W., Shimizu, M., Danyushevsky, L., Saini-Eidukat, B., and Melcher, F., 2009, Trace and minor elements in sphalerite: A LA-ICPMS study: Geochimica et Cosmochimica Acta, v. 73, p. 4761–4791.
Corbett, G.J., and Leach, T.M., 1998, Southwest Pacific rim gold-copper systems: Structure, alteration and mineralization: Society of Economic Geologists, Special Publication 6, 238 p.
Craig, H., 1961, Standard for reporting concentrations of deuterium and oxygen-18 in natural waters: Science, v. 133, p. 1833–1834.
Date, J., Watanabe, Y, and Saeki, Y., 1983, Zonal alteration around the Fukazawa Kuroko deposits, Akita Prefecture, northern Japan: Economic Geology Monograph 5, p. 365–386.
de Ronde, C.E.J., Walker, S.L., Ditchburn, R.G., Caratori Tontini, F., Hannington, M.D., Merle, S.G., Timm, C., Handler, M.R., Wysoczanski, R.J., Dekov, V.M., Kamenov, G.D., Baker, E.T., Embley, R.W., Lupton, J.E., and Stoffers, P., 2014, The anatomy of a buried submarine hydrothermal system, Clark volcano, Kermadec arc, New Zealand: Economic Geology, v. 109, p. 2261–2292.
Ditchburn, R., Graham, I., Barry, B., and de Ronde, C.E.J., 2004, Uranium series disequilibrium dating of black smoker chimneys: New Zealand Science Reviews, v. 61, p. 54–56.
Ditchburn, R.G., and de Ronde, C.E.J., 2017, Evidence for remobilization of barite affecting radiometric dating using ^{228}Ra, ^{228}Th, and ^{226}Ra/Ba values: Implications for the evolution of sea-floor volcanogenic massive sulfides: Economic Geology, v. 112, p. 1231–1245.
Dogramaci, S.S., Herczeg, A.L., Schiff, S.L., and Bone, Y., 2001, Controls on δ^{34}S and δ^{18}O of dissolved SO_4 in aquifers of the Murray basin, Australia, and their use as indicators of flow processes: Applied Geochemistry, v. 16, p. 475–488.
Doyle, M.G., and Allen, R.L., 2003, Subsea-floor replacement in volcanic-hosted massive sulfide deposits: Ore Geology Reviews, v. 23, p. 183–222.
Franklin, J.M., Kasarda, J., and Poulsen, K.H., 1975, Petrology and chemistry of the alteration zone of the Mattabi massive sulfide deposit: Economic Geology, v. 70, p. 63–79.
Franklin, J.M., Lydon, J.W., and Sangster, D.F., 1981, Volcanic-associated massive sulfide deposits: Economic Geology 75th Anniversary Volume, p. 485–627.
Franklin, J.M., Gibson, H.L., Jonasson, I.R., and Galley, A.G., 2005, Volcanogenic massive sulfide deposits: Economic Geology 100th Anniversary Volume, p. 523–560.
Galley, A.G., 1993, Characteristics of semi-conformable alteration zones associated with volcanogenic massive sulphide districts: Journal of Geochemical Exploration, v. 48, p 175–199.
Galley, A.G., Watkinson, D.H., Jonasson, I.R., and Riverin, G., 1995, The subsea-floor formation of volcanic-hosted massive sulfide; evidence from the Ansil deposit, Rouyn-Noranda, Canada: Economic Geology, v. 90, p. 2006–2017.
Galley, A.G., Hannington, M.D., and Jonasson, I., 2007, Volcanogenic massive sulfide deposits, *in* Goodfellow, W.D., ed., Mineral deposits of Canada: A synthesis of major deposit-types, district metallogeny, the evolution of geological provinces, and exploration methods: Mineral Deposits Division, Geological Association of Canada, Special Publication 5, p. 141–161.
Gamo, T., Okamura, K., Charlou, J.-L., Urabe, T., Auzende, J.-M., Ishibashi, J., Shitashima, K., Chiba, H., and Shipboard Scientific Party, 1997, Acidic and sulfate-rich hydrothermal fluids from the Manus back-arc basin, Papua New Guinea: Geology, v. 25, p. 139–142.
Gibson, H.L., and Galley, A.G., 2007, Volcanogenic massive sulfide deposits of the Archean, Noranda district, Quebec, *in* Goodfellow, W.D., ed., Mineral deposits of Canada: A synthesis of major deposit-types, district metallogeny, the evolution of geological provinces, and exploration methods: Mineral Deposits Division, Geological Association of Canada, Special Publication 5, p. 533–552.
Gibson, H.L., Watkinson, D.H., and Comba, C.D.A., 1983, Silicification; hydrothermal alteration in an Archean geothermal system within the Amulet Rhyolite Formation, Noranda, Quebec: Economic Geology, v. 78, p. 954–971.
Gibson, H.L., Watkinson, D.H., Watkins, J.J., Labrie, M., and Doiron, G., 1993, Volcanological reconstruction of the Corbet breccia pile and Cu-Zn massive sulphide deposit, Noranda, Quebec: Exploration and Mining Geology, v. 2, p. 1–16.
Gifkins, C.C., and Allen, R.L., 2001, Textural and chemical characteristics of diagenetic and hydrothermal alteration in glassy volcanic rocks: Examples from the Mount Read Volcanics, Tasmania: Economic Geology, v. 96, p. 973–1002.
Gilg, H.A., and Sheppard, S.M.F., 1996, Hydrogen isotope fractionation between kaolinite and water revisited: Geochimica et Cosmochimica Acta, v. 60, p. 529–533.
Gill, J., Torssander, P., Lapierre, H., Taylor, R., Kaiho, K., Koyama, M., Kusakabe, M., Aitchison, J., Cisowski, S., Dadey, K., Fujioka, K., Klaus, A., Lovell, M., Marsaglia, K., Pezard, P., Taylor, B., and Tazaki, K., 1990, Explosive deep water basalt in the Sumisu backarc rift: Science, v. 248, p. 1214–1217.

Giorgetti, G., Monecke, T., Kleeberg, R., and Hannington, M.D., 2006, Low-temperature hydrothermal alteration of silicic glass at the Pacmanus hydrothermal vent field, Manus basin, an XRD, SEM, and AEM-TEM study: Clays and Clay Minerals, v. 54, p. 240–251.

Hannington, M.D., de Ronde, C.E.J., and Petersen, S., 2005, Sea-floor tectonics and submarine hydrothermal systems: Economic Geology 100th Anniversary Volume, p. 111–141.

Hannington, M.D., Jamieson, J., Monecke, T., and Petersen, S., 2010, Modern sea-floor massive sulfides and base metal resources: Toward an estimate of global sea-floor massive sulfide potential: Society of Economic Geologists Special Publication 15, v. 2, p. 317–338.

Hannington, M.D., Jamieson, J., Monecke, T., Petersen, S., and Beaulieu, S., 2011, The abundance of seafloor massive sulfide deposits: Geology, v. 39, p. 1155–1158.

Hein, J.R., de Ronde, C.E.J., Koski, R.A., Ditchburn, R.G., Mizell, K., Tamura, Y., Stern, R.J., Conrad, T.A., Ishizuka, O., and Leybourne, M.I., 2014, Layered hydrothermal barite-sulfide mound field, East Diamante caldera, Mariana volcanic arc: Economic Geology, v. 109, p. 2179–2206.

Holk, G.J., Taylor, B.E., and Galley, A.G., 2008, Oxygen isotope mapping of the Archean Sturgeon Lake caldera complex and VMS-related hydrothermal system, northwestern Ontario, Canada: Mineralium Deposita, v. 43, p. 623–640.

Hudak, G.J., Morton, R.L., Franklin, J.M., and Peterson, D.M., 2004, Morphology, distribution, and estimated eruption volumes for intracaldera tuffs associated with volcanic-hosted massive sulfide deposits in the Archean Sturgeon Lake caldera complex, northwestern Ontario: American Geophysical Union, Geophysical Monograph 140, p. 345–360.

Huston, D.L., 1999, Stable isotopes and their significance for understanding the genesis of volcanic-hosted massive sulfide deposits: A review: Reviews in Economic Geology, v. 8, p. 157–179.

Inoue, A., Watanabe, T., Kohyama, N., and Brusewitz, A.M., 1990, Characterization of illitization of smectite in bentonite beds at Kinnekulle, Sweden: Clays and Clay Minerals, v. 38, p. 241–249.

Ishibashi, J.-I., Miyoshi, Y., Inoue, H., Yeats, C., Hollis, S.P., Corona, J.C., Bowden, S., Yang, S., Southam, G., Masaki, Y., Hartnet, H., and IODP Expedition 331 Scientists, 2013, Subseafloor structure of a submarine hydrothermal system within volcaniclastic sediments: A modern analogue for "Kuroko-type" VMS deposits [ext. abs.]: Society for Geology Applied to Mineral Deposits (SGA) Biennial Meeting, 12th, Uppsala, Sweden, 2013, Extended Abstracts, p. 542–544.

Ishibashi, J.-I., Ikegami, F., Tsuji, T., and Urabe, T., 2015, Hydrothermal activity in the Okinawa trough back-arc basin: Geological background and hydrothermal mineralization, *in* Ishibashi, J.-I., Okino, K., and Sunamura, M., eds., Subseafloor biosphere linked to hydrothermal systems: Tokyo, Springer, p. 337–359.

Jamieson, J.W., Hannington, M.D., Clague, D.A., Kelley, D.S., Delaney, J.R., Holden, J.F., Tivey, M.K., and Kimpe, L.E., 2013, Sulfide geochronology along the Endeavour segment of the Juan de Fuca Ridge: Geochemistry, Geophysics, Geosystems, v. 14, p. 2084–2099.

Jamieson, J.W., Hannington, M.D., Tivey, M.K., Hansteen, T., Williamson, N.M.-B., Stewart, M., Fietzke, J., Butterfield, D., Frische, M., Allen, L., Cousens, B., and Langer, J., 2016, Precipitation and growth of barite within hydrothermal vent deposits from the Endeavour segment, Juan de Fuca Ridge: Geochimica et Cosmochimica Acta, v. 173, p. 64–85.

Jean-Baptiste P., Charlou, J.L., and Stievenard, M., 1997, Oxygen isotope study of mid-ocean ridge hydrothermal fluids: Implication for the oxygen-18 budget of the oceans: Geochimica et Cosmochimica Acta, v. 61, p. 2669–2677.

Jinfeng, Y., Xing, L., Liang, L., Pan, J., and Meng, T., 2014, Application of short-wave infrared (SWIR) spectroscopy in quantitative estimation of clay mineral contents: IOP Conference Series, Earth and Environmental Science, v. 17, 6 p.

Johnson, D.P., Maillet, P.C., and Rice, R.C., 1992, The seabed morphology of the Hazel Holme fracture zone and the New Hebrides arc, northern Vanuatu-Solomon Islands region: South Pacific Applied Geoscience Commission, Technical Report 138, 28 p.

Kawada, Y., and Yoshida, S., 2010, Formation of a hydrothermal reservoir due to anhydrite precipitation in an arc volcano hydrothermal system: Journal of Geophysical Research, v. 115, B11106.

Kerr, D.J., and Gibson, H.L., 1993, A comparison of the Horne volcanogenic massive sulfide deposit and intracauldron deposits of the Mine sequence, Noranda, Quebec: Economic Geology, v. 88, p. 1419–1442.

King, E.M., Valley, J.W., and Davis, D.W., 2000, Oxygen isotope evolution of volcanic rocks at the Sturgeon Lake volcanic complex, Ontario: Canadian Journal of Earth Science, v. 37, p. 39–50.

Koski, R.A., Jonasson, I.R., Kadko, D.C., Smith, V.K., and Wong, F.L., 1994, Compositions, growth mechanisms, and temporal relations of hydrothermal sulfide-sulfate-silica chimneys at the northern Cleft segment, Juan de Fuca Ridge: Journal of Geophysical Research, v. 99, p. 4813–4832.

Kroenke, L.W., 1995, A morphotectonic interpretation of SPOACMAPS 1:500,000 charts: Central Solomon Islands-Southern Tuvalu: South Pacific Applied Geoscience Commission, Technical Report 220, 42 p.

Kusakabe, M., Komoda, Y., Takano, B., and Abiko, T., 2000, Sulfur isotopic effects in the disproportionation reaction of sulfur dioxide in hydrothermal fluids: Implications for the $\delta^{34}S$ variations of dissolved bisulfate and elemental sulfur from active crater lakes: Journal of Volcanology and Geothermal Research, v. 97, p. 287–307.

Labidi, J., Cartigny, P., Birck, J., Assayag, N., and Bourrand, J., 2012, Determination of multiple sulfur isotopes in glasses: A reappraisal of the MORB $\delta^{34}S$: Chemical Geology, v. 334, p. 189–198.

Labidi, J., Cartigny, P., Hamelin, C., Moreira, M., and Dosso, L., 2014, Sulfur isotope budget (^{32}S, ^{33}S, ^{34}S and ^{36}S) in Pacific-Antarctic ridge basalts: A record of mantle heterogeneity and hydrothermal sulfide assimilation: Geochimica et Cosmochimica Acta, v. 133, p. 47–67.

Large, R.R., Allen, R.L., Blake, M.D., and Herrmann, W., 2001, Hydrothermal alteration and volatile element halos for the Rosebery K Lens volcanic-hosted massive sulfide deposit, western Tasmania: Economic Geology, v. 96, p. 1055–1072.

MacDonald, R., Barrett, W.J., and Sherlock, R.L., 1996, Geology and lithogeochemistry at the Hidden Creek massive sulfide deposit, Anyonx, west-central British Columbia: Exploration and Mining Geology, v. 5, p. 369 – 398.

Maclean, W.H., 1990, Mass change calculation in altered rock series: Mineralium Deposita, v. 25, p. 44–49.

Maclean, W.H., and Barrett, T.J., 1993, Lithogeochemical techniques using immobile elements: Journal of Geochemical Exploration, v. 48, p. 109–133.

Maillet, P., Ruellan, E., Gérard, M., Person, A., Bellon, H., Cotton, J., Joron, J.-L., Nakada, S., and Price, R.C., 1995, Tectonics, magmatism, and evolution of the New Hebrides back-arc troughs (southwest Pacific), *in* Taylor, B., ed., Backarc basins: Tectonics and magmatism: New York, Plenum, p. 177–235.

Marumo, K., Nagasawa, K., and Kuroda, Y., 1980, Mineralogy and hydrogen isotope geochemistry of clay minerals in the Ohnuma geothermal area, northeastern Japan: Earth and Planetary Science Letters, v. 47, p. 255–262.

McConachy, T.F., Yeats, C.J., and Shipboard Scientific Party, 2002, Final cruise FR03-2002, SOLAVENTS-2002, Solomons Australia vents expedition aboard the RV Franklin, 26 March–21 April 2002: Commonwealth Scientific and Industrial Research Organisation (CSIRO), Exploration and Mining Report 1026F, 440 p.

Monecke, T., Giorgetti, G., Scholtysek, O., Kleeberg, R., Götze, J., Hannington, M.D., and Petersen, S., 2007, Textural and mineralogical changes associated with the incipient hydrothermal alteration of glassy dacite at the submarine PACMANUS hydrothermal system, eastern Manus basin: Journal of Volcanology and Geothermal Research, v. 160, p. 23–41.

Monecke, T., Petersen, S., Hannington, M.D., Grant, H., and Samson, I., 2016, The minor element endowment of modern sea-floor massive sulfides and comparison with deposits hosted in ancient volcanic successions: Reviews in Economic Geology, v. 18, p. 245–306.

Monjaret, M.C., Bellon, H., and Maillet, P., 1991, Magmatism of the troughs behind the New Hebrides island arc (RV Jean Charcot SEAPSO 2 cruise): K-Ar geochronology and petrology: Journal of Volcanology and Geothermal Research, v. 46, p. 265–280.

Moore, D.M., and Reynolds, C.R. Jr., 1997, X-ray diffraction and the identification and analysis of clay minerals, 2nd ed: New York, Oxford University Press, 400 p.

Morton, R.L., and Franklin, J.M., 1987, Two-fold classification of Archean volcanic-associated massive sulfide deposits: Economic Geology, v. 82, p. 1057–1063.

Morton, R.L., Walker, J.S., Hudak, G.J., and Franklin, J.M., 1991, The early development of an Archean submarine caldera complex with emphasis on the Mattabi ash-flow tuff and its relationship to the Mattabi massive sulfide deposit: Economic Geology, v. 86, p. 1002–1011.

Mottl, M., Seewald, J., Wheat, C., Tivey, M., Michael, P., Proskurowski, G., McCollom, T.M., Reeves, E., Sharkey, J., and You, C.F., 2011, Chemistry of hot springs along the eastern Lau spreading center: Geochimica et Cosmochimica Acta, v. 75, p. 1013–1038.

Mueller, W., and White, J.D.L., 1992, Felsic fire-fountaining beneath Archean seas: Pyroclastic deposits of the 2730 Ma Hunter mine group, Quebec, Canada: Journal of Volcanology and Geothermal Research, v. 54, p. 117–134.
Mueller, W., White, J.D.L., Stix, J., and Hudak, G.J., 2004, Archean calderas, *in* Ericksson, P., Altermann, W., Nelson, D., Mueller, W., Catuneanu, O., and Strand, K., eds., The Precambrian Earth: Developments in Precambrian geology, v. 12: Elsevier, p. 345–356.
Ohmoto, H., 1983, Geologic setting of the Kuroko deposits, Japan: Part I. Geologic history of the Green Tuff region: Economic Geology Monograph 5, p. 9–24.
——1996, Formation of volcanogenic massive sulfide deposits: The Kuroko perspective: Ore Geology Reviews, v. 10, p. 135–177.
Ono, S., Wing, B.A., Johnston, D., Farquhar, J., and Rumble, D., 2006, Mass-dependent fractionation of quadruple sulfur isotope system as a new tracer of sulfur biogeochemical cycles: Geochimica et Cosmochimica Acta, v. 70, p. 2238–2252.
Paulick, H., and Bach, W., 2006, Phyllosilicate alteration mineral assemblages in the active subsea-floor Pacmanus hydrothermal system, Papua New Guinea, ODP Leg 193: Economic Geology, v. 101, p. 633–650.
Pelletier, B., Lafoy, Y., and Missegue, F., 1993, Morphostructure and magnetic fabric of the northwestern North Fiji basin: Geophysical Research Letters, v. 20, p. 1151–1154.
Pelletier, B., Calmant, S., and Pillet, R., 1998, Current tectonics of the Tonga-New Hebrides region: Earth and Planetary Science Letters, v. 164, p. 263–276.
Piercey, S.J., Squires, G.C., and Brace, T.D., 2014, Lithostratigraphic, hydrothermal, and tectonic setting of the Boundary volcanogenic massive sulfide deposit, Newfoundland Appalachians, Canada: Formation by subsea-floor replacement in a Cambrian rifted arc: Economic Geology, v. 109, p. 661–687.
Récy, J., Charvis, P, Ruellan, E., Monjaret, M.-C., Gérard, M., Auclair, G., Baldassari, C., Boirat, J.-M., Brown, G.R., Butscher, J., Collot, J.Y., Daniel, J., Louat, R., Monzier, M., and Pontoise, B., 1986, Tectonique et volcanisme sous-marin à l'arrière de l'arc des Nouvelles-Hébrides (Vanuatu): Résultats préliminaires de la campagne SEAPSO (leg 2) du N.O. Jean Charcot: Comptes Rendus de d'Académie des Sciences, v. 303, p. 685–690.
Reeves, E.P., Seewald, J.S., Saccocia, P., Bach, W., Craddock, P.R., Shanks, W.C., Sylva, S.P., Walsh, E., Pichler, T., and Rosner, M., 2011, Geochemistry of hydrothermal fluids from the PACMANUS, northeast Pual and Vienna Woods hydrothermal fields, Manus basin, Papua New Guinea: Geochimica et Cosmochimica Acta, v. 75, p. 1088–1123.
Reyes, A.G., 1990, Petrology of Philippine geothermal systems and the application of alteration mineralogy to their assessment: Journal of Volcanology and Geothermal Research, v. 42, p. 279–309.
Rice, C.A., Tuttle, M.L., and Reynolds, R.L., 1993, The analysis of forms of sulfur in ancient sediments and sedimentary rocks: Comments and cautions: Science, v. 107, p. 83–95.
Sandwell, D.T., Müller, R.D., Smith, W.H.F., Garcia, E., and Francis, R., 2014, New global marine gravity model from CryoSat-2 and Jason-1 reveals buried tectonic structure: Science, v. 346, p. 65–67.
Savin, S.M., and Lee, M., 1988, Isotopic studies of phyllosilicates: Reviews in Mineralogy, v. 19, p. 189–223.
Scott, S.D., and Barnes, H.L., 1971, Sphalerite geothermometry and geobarometry: Economic Geology, v. 66, p. 653–669.
Shanks, W.C. III, Böhlke, J.K., and Seal, R.R. II, 1995, Stable isotopes in mid-ocean ridge hydrothermal systems: Interactions between fluids, minerals, and organisms: American Geophysical Union Monograph 91, p. 194–221.
Shau, Y.H., Peacor, D.R., and Essene, E.J., 1990, Corrensite and mixed-layer chlorite-corrensite in metabasalt from northern Taiwan: TEM-AEM, EMPA, XRD, and optical studies: Contributions to Mineralogy and Petrology, v. 105, p. 123–142.
Sheppard, S.M.F., 1986, Characterization and isotopic variations in natural waters: Reviews in Mineralogy, v. 16, p. 165–183.
Sheppard, S.M.F., and Gilg, H.A., 1996, Stable isotope geochemistry of clay minerals: Clay Minerals, v. 31, p. 1–24.
Shikazono, N., Holland, H.D., and Quirk, R.F., 1983, Anhydrite in Kuroko deposits: Mode of occurrence and depositional mechanisms: Economic Geology Monograph 5, p. 329–344.
Shikazono, N., Utada, M., and Shimizu, M., 1995, Mineralogical and geochemical characteristics of hydrothermal alteration of basalt in the Kuroko mine area, Japan: Implications for the evolution of a back arc basin hydrothermal system: Applied Geochemistry, v. 10, p. 621–642.
Shirozu, H., 1974, Clay minerals in altered wall rocks of the Kuroko-type deposits: Society of Mining Geology Special Issue, v. 6, p. 303–311.
Sigurdsson, H., 2000, Volcanic episodes and rates of volcanism, *in* Sigurdsson, H., Houghton, B., Rymer, H., Stix, J., and McNutt, S., eds., Encyclopedia of volcanoes: San Diego, California, Academic Press, p. 271–279.
Skirrow, R.G., and Franklin, J.M., 1994, Silicification and metal leaching in semiconformable alteration beneath the Chisel Lake massive sulfide deposit, Snow Lake, Manitoba: Economic Geology, v. 89, p. 31–50.
Stoffers, P., Worthington, T.J., Schwarz-Schampera, U., Hannington, M.D., Massoth, G.J., Hekinian, R., Schmidt, M., Lundsten, L.J., Evans, L.J., Vaiomo'unga, R., and Kerby, T., 2006, Submarine volcanoes and high-temperature hydrothermal venting on the Tonga arc, southwest Pacific: Geology, v. 34, p. 453–456.
Taylor, B.E., 1992, Degassing of H_2O from rhyolite magma during eruption and shallow intrusion, and the isotopic composition of magmatic water in hydrothermal systems, *in* Hedenquist, J.W., ed., Magmatic contributions to hydrothermal systems: Geological Survey of Japan Reports, v. 279, p. 190–194.
Thode, H.G., and Monster, J., 1961, Sulphur isotope geochemistry: Geochimica et Cosmochimica Acta, v. 25, p. 159–174.
Thompson, A.J.B., Hauff, P.L., and Robitaille, J.A., 1999, Alteration mapping in exploration: Application of short-wave infrared (SWIR) spectroscopy: Society of Economic Geologists Newsletter, no. 39, p. 1–27.
Tostevin, R., Turchyn, A.V., Farquhar, J., Johnston, D.T., Eldridge, D.L., Bishop, J.K.B., and McIlvin, M., 2014, Multiple sulfur isotope constraints on the modern sulfur cycle: Earth and Planetary Science Letters, v. 396, p. 14–21.
Ulrich, M.R., and Bodnar, R.J., 1988, Systematics of stretching of fluid inclusions; II, Barite at 1 atm confining pressure: Economic Geology, v. 83, p. 1037–1046.
Urabe, T., Auzende, J.-M., Deplus, C., Eissen, J.-P., Grimaud, D., Huchon, P., Ishibashi, J., Joshima, M., LaGabrielle, Y., Mevel, C., Naka, J., Tanaka, T., and Tanahashi, M., 1990, Hydrothermal deposits at the central spreading axis of the North Fiji basin (SW Pacific): Preliminary report of the Nautile dives of the STARMER cruise: Mining Geology, v. 40, p. 117–124 (in Japanese with English abs.).
Velde, B., 1980, Cell dimensions, polymorph type, and infrared spectra of synthetic white micas: The importance of ordering: American Mineralogist, v. 65, p. 1277–1282.
Vergnoille, S., and Mangan, M.T., 2000, Hawaiian and Strombolian eruptions, *in* Sigurdsson, H., ed., Encyclopedia of volcanoes: San Diego, Academic Press, p. 447–461.
Wienkenjohann, H., 2015, A sulfur isotope study of the Tinakula deposit, New Hebrides island arc, Solomon Islands: Unpublished B.Sc. thesis, Münster, Germany, Westfälische Wilhelms-Universität Münster, 67 p.
Wood, C.A., 1980, Morphometric evolution of cinder cones: Journal of Volcanology and Geothermal Research, v. 7, p. 387–413.
Zhang, Y., and Frantz, J.D., 1987, Determination of the homogenization temperatures and densities of supercritical fluids in the system NaCl-KCl-$CaCl_2$-H_2O using synthetic fluid inclusions: Chemical Geology, v. 64, p. 335–350.
Zhu, W., Tivey, M.K., Gittings, H., and Craddock, P.R., 2007, Permeability-porosity relationships in seafloor vent deposits: Dependence on pore evolution processes: Journal of Geophysical Research, v. 112, B05208.

Melissa O. Anderson is a newly appointed assistant professor of economic geology at the University of Toronto, Canada. She obtained her B.Sc. (Hon.) degree at Brandon University, Canada, and an M.Sc. degree at the University of New Brunswick, Canada, under the supervision of Drs. Dave Lentz and Chris McFarlane. She completed her Ph.D. degree in 2018 at the University of Ottawa, Canada, under the supervision of Dr. Mark Hannington and spent time as a visiting researcher at GEOMAR Helmholtz Centre for Ocean Research in Kiel, Germany. Her research focuses on understanding the relationships between geodynamics and ore formation in modern seafloor environments.